ABSTRACT

ZHANG, ZHENG. Growth and Characterization of $Cs_2AgBiBr_6$ Double Perovskite Single Crystals for Radiation Detection (Under the direction of Dr. Ge Yang).

In this thesis, the all-inorganic $Cs_2AgBiBr_6$ double perovskite single crystals were grown and fabricated as radiation detection devices for ionizing radiation detection. $Cs_2AgBiBr_6$ single crystals were grown from saturated aqueous solutions using slow temperature lowering (STL) method. To compare the effect of synthesizing stoichiometric ratio on as-grown single crystal qualities, $Cs_2AgBiBr_6$ single crystals were grown from Bi-normal (CsBr:AgBr:$BiBr_3$=2:1:1) and Bi-poor solutions (CsBr:AgBr:$BiBr_3$=2:1:0.8) respectively.

To evaluate the potential of using $Cs_2AgBiBr_6$ single crystals for ionizing radiation detection, various techniques and methods were employed to characterize the material properties. X-ray diffraction (XRD) and cathodoluminescence (CL) measurements of $Cs_2AgBiBr_6$ single crystals were carried out at analytical instrumentation facility (AIF) of NCSU. The obtained XRD pattern of $Cs_2AgBiBr_6$ single crystals matches well with the $Cs_2AgBiBr_6$ reference pattern in the database (ICSD collection #252164). Measured photoluminescence spectrum at 78.5 K gave the bandgap energies of $Cs_2AgBiBr_6$ to be 2.00 eV and 2.26 eV, which are close to that was observed in the temperature-dependent CL spectra. Current-voltage (I-V) measurement gave the room-temperature resistivity of $Cs_2AgBiBr_6$ to be at 2.6×10^{10} Ω·cm, which is comparable to that of today's leading room-temperature semiconductor detector material cadmium zinc telluride (CdZnTe or CZT). Further, mobility-lifetime (μ-τ) product is a key factor which ultimately determines the drift distance of charge carriers (electrons and holes). We evaluated the μ-τ product of $Cs_2AgBiBr_6$ using the laser-induced photocurrent approach and estimated the μ-τ product of $Cs_2AgBiBr_6$ to be 2.48×10^{-3} cm^2/V, which is slightly lower than that of the highest quality CdZnTe single crystals (~10^{-2} cm^2/V) but may be further improved by adjusting the

crystal growth methods. The surface recombination velocity determined using Many's equation is 2367.6 cm/s. Even though the crystal surface has been rinsed with ethanol, ethanol should not be the best option due to the remaining high surface recombination velocity. Methanol, isopropanol, or ultraviolet-ozone (UV-O_3) may be adopted to further treat the perovskite crystal surfaces to lower the probabilities of surface recombination.

The material defects are playing an important role when extracting charges from radiation detection devices. To understand the defect trap level in $Cs_2AgBiBr_6$ single crystals, we fabricated a planar Au/$Cs_2AgBiBr_6$/Au device (50 nm Au was deposited on the two parallel polished crystal surfaces). Space charge limited current (SCLC) was performed at room temperature to determine the density of trap states, which is estimated to be 1.44×10^{10} cm^{-3}. Charge carrier mobility 7.02 cm^2/V-s was determined at the same time from the Child regime of SCLC curve. The deep level defects are undesirable and can be better interpreted using the temperature-dependent resistivity measurement, from which we estimated the Fermi level of $Cs_2AgBiBr_6$ lies at 0.788 eV above the valence band. This indicates that the Fermi level pinning phenomenon is possible in $Cs_2AgBiBr_6$ if the CL spectra are analyzed correspondingly.

Finally, the $Cs_2AgBiBr_6$-based detector showed excellent linear response to 8 keV X-rays, produced from high voltage X-ray tube. This linearity enables $Cs_2AgBiBr_6$ for rapid dose determination in medical imaging applications. Gamma-ray energy spectrum recorded using Bi-poor $Cs_2AgBiBr_6$ single crystals gave an energy resolution of 15.53% at 59.5 keV (0.1 μCi Am-241 gamma source). This finding for the first time demonstrated that $Cs_2AgBiBr_6$ single crystals grown from Bi-poor precursor solutions hold great potentials for the use as next generation low-cost semiconductor gamma-ray detector materials.

Growth and Characterization of $Cs_2AgBiBr_6$ Double Perovskite Single Crystals for Radiation Detection

by
Zheng Zhang

A dissertation submitted to the Graduate Faculty of
North Carolina State University
in partial fulfillment of the
requirements for the degree of
Doctor of Philosophy

Nuclear Engineering

Raleigh, North Carolina
2020

APPROVED BY:

_____	_____
Dr. Ge Yang Committee Chair	Dr. Mohamed Bourham
_____	_____
Dr. John Mattingly	Dr. Dali Sun

DEDICATION

This dissertation is dedicated to my parents for their support and encouragement during my Ph.D. study.

BIOGRAPHY

Zheng Zhang obtained his Bachelor of Engineering (B.E.) degree in Nuclear Technology from Lanzhou University, China. He completed his Master of Science (M.S.) study in Nuclear Engineering at the University of Missouri - Rolla. Zheng Zhang is currently a Ph.D. candidate at North Carolina State University (NCSU) and will graduate in November 2020. His Ph.D. research is developing perovskite (traditional methylammonium(MA) and formamidinium(FA)-based perovskites and double perovskites) single crystals for ionizing radiation detection, specifically X-ray, gamma-ray, and alpha particle detection.

ACKNOWLEDGMENTS

Foremost, I would like to express my sincere thanks to my advisor Dr. Ge Yang, who provided guidance and great support for my Ph.D. study.

I also would like to thank my Ph.D. defense committee members, Dr. Mohamed Bourham, Dr. John Mattingly, and Dr. Dali Sun. Thanks to all of you for taking your time to attend my defense presentations.

Finally, I want to acknowledge the help of our collaborators (Dr. Dali Sun's research group at the physics department, Eric Vetter and Zhengjie Huang; Dr. Kenan Gundogdu's research group, Dovletgeldi Seyitliyev; Dr. Felix N. Castellano and Dr. Evgeny O. Danilov from the chemistry department at NCSU) and also my colleague Ibrahim Hany. The staff at analytical instrumentation facility (AIF) of NCSU (Dr. Chuanzhen Zhou, Dr. Ching-Chang Chung) also provided great help and guidance for the X-ray diffraction (XRD) and cathodoluminescence (CL) experiments. Without them, this dissertation would never be possible.

TABLE OF CONTENTS

LIST OF TABLES vi
LIST OF FIGURES vii

Chapter 1: Introduction & Motivation 1
1.1 Introduction 1
1.2 Motivation 5
1.3 Perovskite Materials 7
1.4 Requirements of Materials for Radiation Detection 9
1.5 Materials Selection 18
Chapter 2: Single Crystal Growth 20
2.1 Perovskite Single Crystal Growth Methods 20
2.2 Growth of $Cs_2AgBiBr_6$ Single Crystals 23
Chapter 3: Device Fabrication 26
3.1 Crystal Surface Processing Techniques 26
3.2 Fabrication of $Cs_2AgBiBr_6$-Based Detectors 28
Chapter 4: Materials Characterization 31
4.1 Photon Attenuation 31
4.2 X-Ray Diffraction Pattern 32
4.3 Current-Voltage (I-V) Characteristic 33
4.4 Temperature-Dependent Resistivity 34
4.5 Bandgap Energy of $Cs_2AgBiBr_6$ 37
4.6 Space Charge Limited Current (SCLC) Characterization 41
4.7 Mu-Tau Product 43
4.8 Response to LED Light 44
4.9 Comparison Study Between Bi-normal and Bi-poor $Cs_2AgBiBr_6$ 45
4.9.1 XRD Measurements and Rocking Curve 45
4.9.2 Comparison Between SCLC Curves 46
4.9.3 Mu-Tau Product 47
4.9.4 Response to Gamma Radiation 48
Chapter 5: Response to X-Ray 50
Chapter 6: Issues for Further Development 52
6.1 Ionic Migration 52
6.2 Aging Effect 53
6.3 Poor Electron Transport 56
6.4 Reducing the bandgap energy 58
6.5 Limited crystal size by conventional STL method 59
Chapter 7: Summary and Conclusions 60
REFERENCES 64
APPENDICES 79
Appendix A 80
Appendix B 86
Appendix C 90

LIST OF TABLES

Table 1.1 Room-temperature properties of common semiconductor materials for X-ray and gamma-ray detectors. [101-103] 17

Table 4.1 Peak energies in the CL spectrum 41

Table 7.1 Summary of the evaluated properties of Bi-normal $Cs_2AgBiBr_6$ single crystals 61

Table 7.2 Comparison between the Bi-normal and Bi-poor $Cs_2AgBiBr_6$ single crystals 62

Table A1 Luminescence origins of CL emission peaks 83

LIST OF FIGURES

Figure 1.1 Cadmium zinc telluride single crystals with as-shown dimensions up to $31\times33\times18$ mm^3. (Reproduced with permission from [86], IEEE Publishing, Copyright 2004.) ….. 3

Figure 1.2 Energy spectrum for 662 keV gamma-ray recorded by (a) CZT (b) NaI:Tl scintillator detectors. (Reproduced with permission from [2], Nature Publishing Group, Copyright 2019.) (Reproduced from [83], Copyright 2005.) …..... 4

Figure 1.3 A schematic which shows the working principle of semiconductor-based detectors…..... 5

Figure 1.4 Perovskite crystal structure ranging from (a) cubic (b) tetragonal (c) orthorhombic. In one unit cell, the A atom is in the corner position, B atom sits at body center, X atom sits at face center. (Reproduced with permission from [84], Wiley-VCH, Copyright 2018.) …..... 7

Figure 1.5 Energy spectrum of 59.5 keV gamma-ray, recorded using $FAPbI_3$ single crystal-based detectors. (Reproduced with permission from [24], Nature Publishing Group, Copyright 2016.)….. 9

Figure 1.6 A schematic that shows the direct band to band transition and indirect band to band transition in semiconductor solids. 1 – below bandgap and thus no absorption; 2 – absorption onset (due to the assist of phonons in indirect bandgap semiconductors or defects in direct bandgap semiconductors); 3 – high absorption edge. (Reproduced with permission from [96], Nature Publishing Group, Copyright 2019.) ….. 11

Figure 1.7 A ToF pulse trace for electrons using $TlSn_2I_5$ detector, measurement was performed using ^{241}Am alpha source at 100 V bias. (Reproduced with permission from [100], American Chemical Society, Copyright 2017.)….. 14

Figure 1.8 Time-resolved photoluminescence (PL) measurement of $MAPbCl_3$ single crystals. (Reproduced with permission from [89], Royal Society of Chemistry, Copyright 2019.)….. 16

Figure 2.1 Illustration of the (a) STL (b) ITC and (c) anti-solvent methods for growing perovskite single crystals…..... 20

Figure 2.2 (a) and (b) $MAPbBr_3$ single crystal (orange), placed near a millimeter ruler. $MAPbI_3$ single crystal (black), grown by ITC technique. (Reproduced with permission from [40], Nature Publishing Group, Copyright 2015.) 21

Figure 2.3 $CsPbBr_3$ single crystals, grown using anti-solvent approach. (Reproduced

with permission from [33], American Chemical Society, Copyright 2017.) (b) $CsPbBr_3$ single crystals, grown from Bridgman technique. (Reproduced with permission from [21], Nature Publishing Group, Copyright 2018.) 22

Figure 2.4 (a) and (b) Pristine $Cs_2AgBiBr_6$ single crystals grown using Bi-normal solution growth method..... 24

Figure 2.5 (a) Schematic illustration of the Bi-normal and (b) Bi-poor $Cs_2AgBiBr_6$ crystal growth processes. As-grown (c) Bi-normal and (d) Bi-poor $Cs_2AgBiBr_6$ single crystals. (e) Photographs of Bi-normal and (f) Bi-poor $Cs_2AgBiBr_6$ single crystals under Nikon optical microscope... 25

Figure 3.1 Illustration of the CH_3NH_2 gas treatment for $MAPbI_3$ single crystals, right shows the scanning electron microscopy (SEM) images without and with CH_3NH_2 gas treatment. (Reproduced with permission from [51], American Chemical Society, Copyright 2018.) 27

Figure 3.2 Photoluminescence (PL) spectra of $MAPbBr_3$ single crystals before and after UV-O_3 surface passivation. (Reproduced with permission from [52], Nature Publishing Group, Copyright 2016.) 28

Figure 3.3 Schematic illustration of the $Cs_2AgBiBr_6$ single crystals-based devices for electrical measurements and radiation response testing..... 29

Figure 4.1 Attenuation coefficient of CdZnTe, $Cs_2AgBiBr_6$, and CdTe crystals as a function of photon energy, from soft X-ray to high energy gamma rays. Inset plot shows the attenuation coefficient as a function of photon energy, from 0.1 MeV to 3 MeV 32

Figure 4.2 X-ray diffraction (XRD) pattern of $Cs_2AgBiBr_6$ single crystal grown with our solution process. The inset is a picture of a typical as-grown single crystal 33

Figure 4.3 Current-voltage (I-V) curve of $Cs_2AgBiBr_6$. Measurement was conducted at room temperature (19 ℃). Note the curve does not pass origin, probably indicating the existence of weak Schottky barrier..... 33

Figure 4.4 (a) and (b) I-V curves and the resistivity of $Cs_2AgBiBr_6$ single crystal at different temperatures..... 35

Figure 4.5 (a) and (b) Temperature dependence of the resistivity for Fermi level determination and the relative Fermi level position in the forbidden band..... 37

Figure 4.6 Estimation of the bandgap of $Cs_2AgBiBr_6$ using the variation of current with temperature. (Applied bias voltage: 1.0 V) 38

Figure 4.7 (a) $Cs_2AgBiBr_6$ single crystal was placed in position for PL excitation. (b) Low temperature photoluminescence (PL) spectrum of $Cs_2AgBiBr_6$ under 488 nm excitation 38

Figure 4.8 CL spectrum of $Cs_2AgBiBr_6$ single crystal at T=83 K..... 40

Figure 4.9 Space charge limited current (SCLC) measurement of Bi-normal $Cs_2AgBiBr_6$ single crystals, performed at 23 ℃ and Au was selected for electrodes deposition 42

Figure 4.10 Recorded photocurrent using Bi-normal $Cs_2AgBiBr_6$ single crystals under laser excitation at the wavelength of 450 nm. Orange curve is the fitting line using Many's equation 44

Figure 4.11 Strong luminescence of $Cs_2AgBiBr_6$ under illumination of visible light (400 nm wavelength)..... 45

Figure 4.12 Response of $Cs_2AgBiBr_6$ single crystals to LED light (wavelength: 472 nm), bias voltage: −5 V 45

Figure 4.13 XRD patterns of as-grown (a) Bi-normal and (b) Bi-poor $Cs_2AgBiBr_6$ single crystals. (c) Rocking curve for Bragg peak (111) of Bi-poor $Cs_2AgBiBr_6$ single crystals, red line is the Pearson VII fitting curve. 46

Figure 4.14 SCLC curves of (a) Bi-normal and (b) Bi-poor as-grown $Cs_2AgBiBr_6$ single crystals. The measurements were conducted at room temperature. (c) Photocurrent recorded for Bi-poor and Bi-normal $Cs_2AgBiBr_6$ single crystals using 450 nm laser excitation. The data is fitted by Many's equation. (d) Response of Bi-poor $Cs_2AgBiBr_6$-based detector to 0.1 μCi Am-241 radioactive source. The detector is biased at 200 V. Blue line is the Gaussian fitting curve 48

Figure 4.15 The energy spectrum recorded by Bi-poor $Cs_2AgBiBr_6$ detectors with and without Am-241 radioactive source. The data were collected with shaping time of 2 μs and bias at 200 V. The blue line is the Gaussian fitting curve for 59.5 keV gamma-ray energy peak. 49

Figure 5.1 Response of Au/$Cs_2AgBiBr_6$/Au device to X-ray radiation. The tested $Cs_2AgBiBr_6$ single crystals were grown from Bi-normal conditions 50

Figure 5.2 Recorded photocurrent of Au/$Cs_2AgBiBr_6$/Au device versus the variation of X-ray tube current, measured at bias voltage 5 V 51

Figure 5.3 Variation of photocurrent versus applied bias voltage (The X-ray tube current is fixed at 30 mA) 51

Figure 6.1 Recorded current vs. time to show the ionic migration issues in $Cs_2AgBiBr_6$ double perovskites, measurement was conducted when the crystal was exposed to relatively weak room light and bias at 5 V. 52

Figure 6.2 Response of Bi-poor $Cs_2AgBiBr_6$ single crystals to 472 nm LED light at bias voltage of +10 V and -10 V..... 52

Figure 6.3 Phase transition of FAPbI3 from black phase to yellow phase within hours. (Reproduced with permission from [31], John Wiley and Sons, Copyright 2016.)...54

Figure 6.4 PXRD patterns for Bi-normal and Bi-poor $Cs_2AgBiBr_6$ samples that have been exposed under ambient air conditions for months..... 55

Figure 6.5 Rocking curve (RC) measurements for Bi-normal and Bi-poor $Cs_2AgBiBr_6$ single crystals, samples have been stored under ambient air conditions for months..... 56

Figure 6.6 Recorded laser-induced current in Bi-poor $Cs_2AgBiBr_6$ single crystals at positive and negative bias of 10 V and 20 V, wavelength of the laser used is 450 nm. ..... ……57

Figure 6.7 Illustration of the $Cs_2AgBiBr_6$ single crystal using slow evaporation method at 60 ℃ and 150 ℃ respectively. Double perovskite (DP) single crystals grown at 60 ℃ presents a red color, a black color is observed for DP single crystals grown at 150 ℃. (Reproduced with permission from [97], Wiley-VCH, Copyright 2020.)……..……...59

Figure A1 Cathodoluminescence spectrum of $Cs_2AgBiBr_6$ single crystals at (a) 123 K (b) 163 K (c) 203 K (d) 243 K (e) 293 K 82

Figure A2 Grouped CL spectra for comparison, measured from 83 K to room temperature 293 K. The spectrum is shifted for clarity. 82

Figure A3 CL transition energy levels in $Cs_2AgBiBr_6$ single crystals. To clarify, the dashed line on the 2.054 eV emission refers to the possible Cs_i (+1/0) or Ag_i (+1/0) defect energy level. Note the energy depicted in the plot corresponds to T=83 K. V represents vacancy defects (e.g., V_{Br}: Br vacancy), Ag_{Bi} and Bi_{Ag} are antisite substitution defects. 83

Figure A4 Energy of CL features vs. temperature. Solid lines are the linear fitting curve with slope displayed. 84

Figure A5 Zoom-in CL plot of (a) C feature and (b) D feature and (c) E feature. 84

Figure A6 Linewidth of CL emission peaks at measured temperatures. The curve is shifted for clarity. 85

Figure B1 Time-of-Flight (ToF) pulse traces using Bi-poor $Cs_2AgBiBr_6$-based detector and ^{241}Am radioactive source, the detector is biased at (a) 100 V and (b) 50 V respectively. 87

Figure B2 Response of Bi-poor $Cs_2AgBiBr_6$ single crystals to Am-241, Na-22, and Cs-137 radioactive sources, measurement was conducted at room temperature with bias of +70V. 87

Figure B3 Comparison between the gamma energy spectrum recorded by CZT and Bi-poor $Cs_2AgBiBr_6$-based detectors, measurement was conducted at room temperature with 100 seconds recording time. 89

Figure C1 Current-voltage measurement of Bi-poor $Cs_2AgBiBr_6$ single crystals, measurement was conducted at room temperature. 90

Chapter 1: Introduction & Motivation

Part of this chapter is published in *Journal of Materials Science: Materials in Electronics* [1].

1.1 Introduction

Ionizing radiation has two types, electromagnetic and particulate. X-ray (100 eV to 200 keV) and gamma ray (> 100 keV) belong to electromagnetic radiation and they are consisted of photons. In particulate radiation, beta particles are high-energy electrons or positrons, and alpha particles are heavy charged helium-4 nucleus. Detection of ionizing radiation has played an important role in many fields, such as homeland security, nuclear nonproliferation, medical imaging, industrial monitoring, nuclear site inspection, astrophysical study, and basic scientific research [2, 3, 4]. Due to the broad applications and great importance of ionizing radiation detection, high-performance radiation detectors have been continuously sought after.

In the past years, many materials have been employed as radiation detector materials and three types of detectors (gas-filled detectors, scintillator-based detectors, and semiconductor detectors) have been typically used. Gas-filled detectors, as its name suggests, are using gas as the detection medium. Because of the low density and low average atomic number Z of gases, gas-filled detectors do not have high stopping power for heavy charged alpha particles and suitable mass attenuation coefficients for X-ray and gamma photons. The stopping power for heavy charged particles can be described using the Bethe formula,

$$-\frac{dE}{dx} = \frac{4\pi}{m_e c^2} \cdot \frac{nz^2}{\beta^2} \cdot \left(\frac{e^2}{4\pi\varepsilon_0}\right)^2 \cdot \left[\ln\left(\frac{2m_e c^2 \beta^2}{I \cdot (1-\beta^2)}\right) - \beta^2\right] \qquad (1)$$

where $n = \frac{N_A \cdot Z \cdot \rho}{A \cdot M_u}$ (M_u: molar mass constant, Z: atomic number of the target, A: relative atomic mass) and n is the electron number density, $\beta = v/c$, ε_0 is the vacuum permittivity, z is the

charge of projectile, I is mean excitation potential. In general, if the detection medium has higher atomic number Z, the stopping power for heavy charged alpha particles would be correspondingly larger. For gases, they usually have low average atomic number Z and thus do not have sufficient stopping power for heavy charged alpha particles. Gas-filled detectors typically are only used to count the interaction events. For X-ray and gamma photon attenuation, the mass attenuation coefficients are given in below,

$$\frac{\mu}{\rho} = \frac{б}{M} N_A \qquad (2)$$

where μ/ρ is the mass attenuation coefficient (cm^2/g), ρ is the material density (g/cm^3), μ is called linear attenuation coefficient (cm^{-1}, $\mu = \ln(I_0/I)/x$, x is the distance photon travels, I_0 is the photon intensity before interacting with the detector, and I is the intensity after photon travels distance x), б is the total interaction cross section, N_A is Avogadro number, M is the molecular weight of the detection medium. Depending on the interaction process, the total interaction cross section б can be written as below,

$$\sigma = \sigma_{pe} + \sigma_{coh} + \sigma_{compton} + \sigma_{pair} + \sigma_{trip} \qquad (3)$$

where σ_{pe} is for photoelectric process and varies with Z^4/E^3 (Z is the average atomic number and E is the photon energy), σ_{coh} ($\sim Z/E^2$) is for coherent scattering, $\sigma_{compton}$ ($\sim Z$) is for Compton scattering, σ_{pair} ($\sim Z^2$) is for pair production interaction, and σ_{trip} is for triplet interaction ($\sigma_{trip}/б_{pair} = 1/Z$). In general, only the photoelectric, Compton scattering, and pair production happen frequently. The coherent scattering and triplet interaction have low probabilities to occur.

In the photoelectric process, the entire energy carried by one photon is transferred to electrons and the interaction usually only occurs in low energy range (10 keV to 500 keV). During the Compton scattering process, part of the photon energy is lost and gained by electrons.

This type of interaction can happen in a broad photon energy range (50 keV to 3 MeV). The pair production creates one positron and one electron and it requires a minimum of photon energy of 1.022 MeV. Therefore, pair production only occurs at photon energy greater than 1.022 MeV. Photons could also interact with the nucleus and induce nuclear fission, but this only happens in very high-energy range (~ tens of MeV).

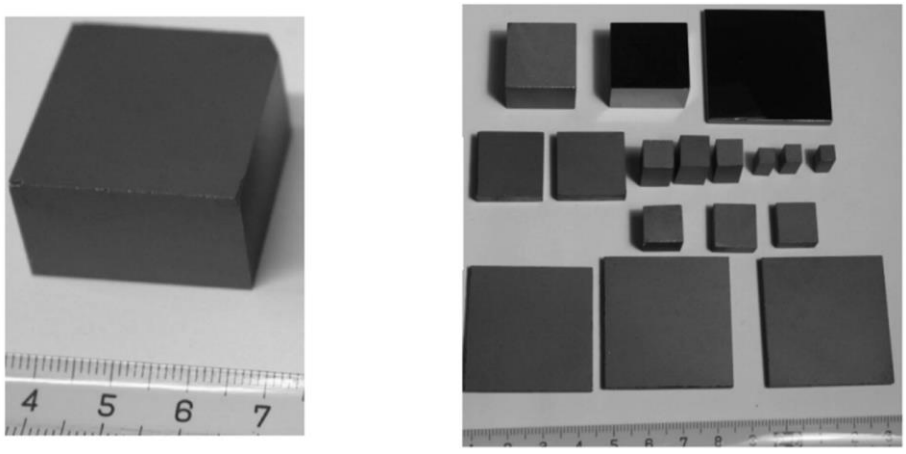

Figure 1.1 Cadmium zinc telluride single crystals with as-shown dimensions up to 31×33×18 mm^3. (Reproduced with permission from [86], IEEE Publishing, Copyright 2004.)

Scintillators-based and semiconductors-based detectors have been widely used for nuclear spectroscopic applications. One important aspect of nuclear spectroscopy is that it could help identify the radioactive nuclides, which thus leads to an important concept named as detector energy resolution (taken as the full width at half maximum (FWHM) over the peak centroid). Figure 2.1 (a) and (b) show the energy spectrum recorded by cadmium zinc telluride (CZT, shown in Figure 1.1, one of today's leading room-temperature semiconductor detector materials) and Tl doped sodium iodide (NaI) scintillator detectors. The CZT detector gives an excellent energy resolution of 0.9% at 662 keV, while the NaI:Tl scintillator gives a relatively broader photo-peak with energy resolution of 6.14% [83].

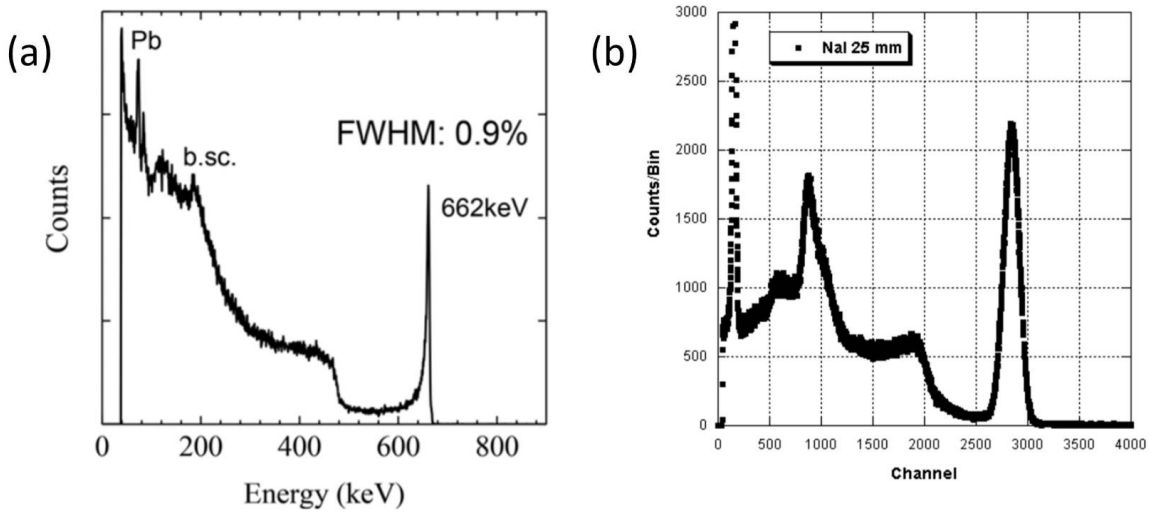

Figure 1.2 Energy spectrum for 662 keV gamma-ray recorded by (a) CZT (b) NaI:Tl scintillator detectors. (Reproduced with permission from [2], Nature Publishing Group, Copyright 2019.) (Reproduced from [83], Copyright 2005.)

Scintillators-based detectors are working based on the production of scintillation light photons and usually require further photomultiplier tube (PMT) to convert the scintillation photons into electrical current. In comparison with scintillator detectors, electron-hole pairs are created in semiconductor-based detectors and photon-to-current conversion is direct (i.e., no PMT is needed) (see Figure 1.3, which shows the working principle of semiconductor-based detectors). Scintillator detectors are typically cheaper compared with the cost of semiconductor-based detectors. For example, the cost of high-purity germanium (Ge) semiconductor detector is roughly $100K compared with $5K for thallium-doped sodium iodide (NaI(Tl)) scintillation detectors. Besides, the number of visible photons created in scintillators is much lower than the number of electron-hole pairs produced per one incident X-ray or gamma photon in semiconductor solids.

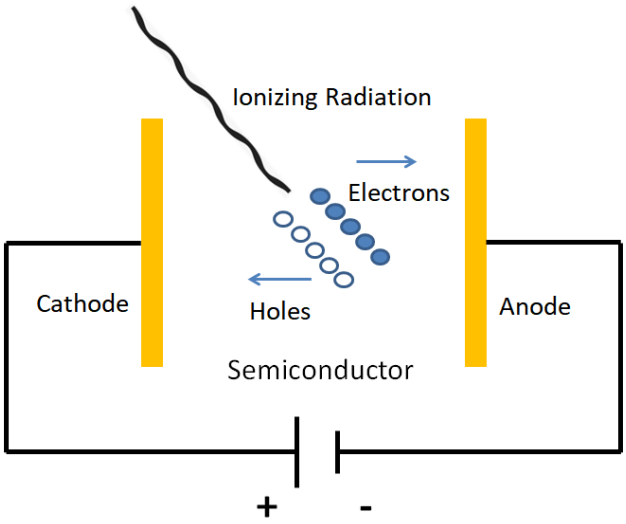

Figure 1.3 A schematic which shows the working principle of semiconductor-based detectors

Chapter 1 of this dissertation discusses the basic concepts, motivation, and history of this research. Chapter 2 explains the solution-based and melt-based single crystal growth methods for perovskites. The surface polishing and processing methods for as-grown $Cs_2AgBiBr_6$ single crystals are discussed in chapter 3. Chapter 4 and 5 summarized the characterized $Cs_2AgBiBr_6$ single crystal properties (physical, optical, and electrical) and the relation between the characterized material properties and the detector performance. Chapter 6 discusses some of the existing issues for further development of $Cs_2AgBiBr_6$ for ionizing radiation detection. Finally, conclusions and summary are made in chapter 7.

1.2 Motivation

Perovskite single crystals have recently attracted great attention as scintillation materials and semiconductor solids for radiation detection. Research focus of this dissertation is to investigate the possibilities of using $Cs_2AgBiBr_6$ double perovskite single crystals as semiconductor materials for alpha particle, X-ray, and gamma-ray detection.

In the past decades, many semiconductor solids, either in single element (e.g., silicon (Si), germanium (Ge)) or compound form (e.g., cadmium telluride (CdTe), gallium arsenide (GaAs)), have been extensively studied for radiation detection [5-8]. Even though great successes have been achieved, certain limitations remain untackled. For example, high purity germanium (HPGe) detector can offer excellent energy resolution at room temperature [6]. However, HPGe needs to be cooled down to cryogenic temperature for routine operations due to its small band gap energy (0.66 eV) and low resistivity (50 Ω·cm) at room temperature [9]. This is because the small band gap energy and low resistivity of Ge single crystals at room temperature can cause a very large leakage current (which serves as source of detector noise) in HPGe detectors due to thermal excitations. Requirement of cryogenic cooling makes HPGe detectors very expensive owing to the additional bulky cooling system and complicated maintenance requirements. Cadmium zinc telluride (CdZnTe) compound semiconductors have been explored as a leading room-temperature gamma-ray detector material due to its unique advantages [3, 10-13]. However, the development of CdZnTe single crystals still suffers from undesirable issues, such as compositional non-uniformity, high concentrations of Te inclusions and sub-grain boundaries [14], which originate from the high temperature melt growth and subsequent cooling processes. Moreover, the fabrication cost of CdZnTe gamma-ray detectors remains relatively high although many efforts have been made to reduce the cost. Another compound semiconductor material, Thallium bromide (TlBr), could exhibit room-temperature gamma-ray detection capabilities initially. Nevertheless, the associated polarization phenomenon, where the detection performance degrades over time, presents a realistic challenge towards the use of TlBr for gamma-ray detection. Owing to such, there is continuously a need for new semiconductor radiation detector materials to lower the production cost, and at the same

time maintain comparable device performance. Perovskite family is one group of such candidates with great potentials.

1.3 Perovskite Materials

Perovskite structure (cubic, tetragonal, or orthorhombic, Figure 1.4) was firstly discovered in 1926 by Victor Goldschmidt [29]. Nevertheless, not much attention was paid to their unique crystal structure and properties at that time. It was until recently that perovskites have been re-discovered. Due to their unique properties, perovskites in the form of single crystals or polycrystalline thin films (which have many grain boundaries compared with single crystals) with general molecular form ABX_3 (where $A=Cs^+$, methylammonium (MA or $CH_3NH_3^+$), formamidinium (FA or $HC(NH_2)_2^+$), Rb(MAFA), $B=Pb^{2+}$, Sn^{2+}, $X=Cl^-$, Br^-, I^-) have received broad attention for applications in optoelectronic devices, light-emitting diodes, and radiation detectors over the recent few years [15-24].

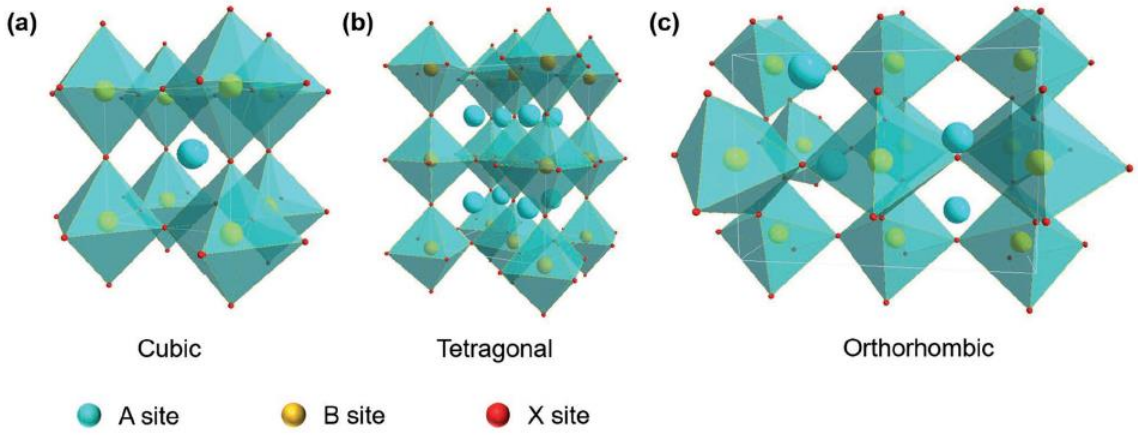

Figure 1.4 Perovskite crystal structure ranging from (a) cubic (b) tetragonal (c) orthorhombic. In one unit cell, the A atom is in the corner position, B atom sits at body center, X atom sits at face center. (Reproduced with permission from [84], Wiley-VCH, Copyright 2018.)

Use of perovskite single crystals for radiation detection was pioneered by Stoumpos et al. in 2013 [30]. Synthesis and structural, optoelectronic characterizations of $CsPbBr_3$ perovskite single crystals were carried out. Even though $CsPbBr_3$ possesses great potentials for ionizing radiation detection, no response to radiation was reported in this work. It was until 2016, Wei et al. studied the use of $MAPbBr_3$ single crystals for X-ray detection [52]. The X-ray detector made of $MAPbBr_3$ single crystals showed a high sensitivity of 80 μC $Gy_{air}^{-1}cm^{-2}$ and low detection dose rate of 0.5 $\mu Gy_{air}s^{-1}$ to continuum X-ray energy (up to 50 keV with peak centered at 22 keV). Soon later, Yakunin et al. systematically studied the gamma photon response using $MAPbI_3$, $MAPbBr_3$, $MAPbCl_3$, $FAPbI_3$, $FAPbBr_3$, and I-treated $MAPbBr_3$ single crystals [24]. In this work, $FAPbI_3$ single crystals-based detectors for the first time exhibited 35% energy resolution to 59.5 keV gamma photopeak (Figure 1.5, 59.5 keV gamma-ray is emitted as byproduct from the alpha decay of Am-241 radioactive source). This for the first time demonstrated that perovskite single crystals could potentially be used for room-temperature gamma-ray detection. Recently, He et al. fabricated the all-inorganic $CsPbBr_3$-based Ohmic and Schottky single crystal devices. $CsPbBr_3$-based Schottky detector showed high spectral resolution for Co-57 122 keV and Cs-137 662 keV gamma-rays (3.9% and 3.8% respectively) [21]. The rapid progress within a relatively short period clearly indicates that perovskites materials hold great potentials towards future room-temperature gamma-ray detection.

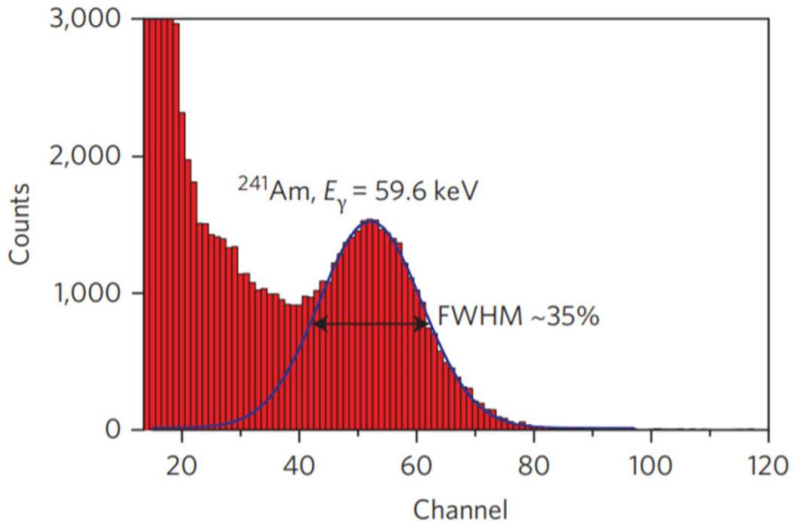

Figure 1.5 Energy spectrum of 59.5 keV gamma-ray, recorded using $FAPbI_3$ single crystal-based detectors. (Reproduced with permission from [24], Nature Publishing Group, Copyright 2016.)

Practicality of using perovskite single crystals for radiation detection arises from the low fabrication cost using solution-processing methods, the high average atomic number Z, high resistivity for leakage current reduction, high defect tolerance ability, large mobility-lifetime (μ-τ) product of charge carriers, tunable optical band gap, and excellent thermal stability [17, 21, 24-28]. In next section, the aforementioned characteristics of perovskites will be discussed in details.

1.4 Requirements of Materials for Radiation Detection

Perovskite single crystals meet most requirements for the use as semiconductor radiation detector materials. For example, the atomic number of Cs, Pb, and Br in $CsPbBr_3$ perovskite single crystals are 55, 82, and 35 respectively. This gives $CsPbBr_3$ a very high average atomic number of 48.4. Perovskites also have suitable resistivity for leakage current reduction. The leakage current serves as detector noise and therefore could degrade the detector energy

resolution, which is undesirable. The bulk crystal resistivity usually can be determined by measuring the current-voltage (I-V) curve, from which the resistivity ρ can be expressed in the following way,

$$\rho = \frac{R \times A}{L} = \frac{\frac{V}{I} \times A}{L} \qquad (4)$$

where V is the voltage (V), I is current (A), R is resistance (Ω), L is the single crystal thickness (cm), A is the surface area (cm^2). Hybrid (i.e., organic-inorganic, such as MA and FA-based single crystals $MAPbI_3$ and $FAPbI_3$) and all-inorganic $CsPbBr_3$ perovskite single crystals have resistivity of 10^7 to 10^9 Ω·cm [17, 28, 31-34], which is suitable for performing X-ray and gamma photon detection. In comparison with the resistivity of CdZnTe (~10^{10} Ω·cm) single crystals, the resistivity of hybrid and all-inorganic $CsPbBr_3$ single crystals is slightly lower. Therefore, the resistivity of hybrid and $CsPbBr_3$ perovskite single crystals should be further improved to lower the detector noise for room temperature radiation detection applications.

To be used as semiconductor detector materials, a good candidate should have suitable optical band gap energy and large mobility-lifetime (μ-τ) product. The band gap energy of semiconductors is defined from the valence band maximum (VBM) to the conduction band minimum (CBM). If the semiconductor has direct bandgap, then electrons can move from VBM to CBM without the assist of phonons. In indirect bandgap semiconductor solids, photons will need to participate in the optical transition process so that momentum of electrons can be conserved (Figure 1.6). Electrons can only be free to move (i.e., conduct the flow of current) when they enter the conduction band of semiconductor solids. Band gap energy which is larger than 1.5 eV in semiconductors is required for performing X-ray and gamma ray detection [35]. This is because if the band gap energy is too small, electrons can easily move from valence band

to conduction band due to thermal excitations so that many noisy signals could be registered as detector noise. If the band gap energy is too large, it will work towards insulators. Suitable band

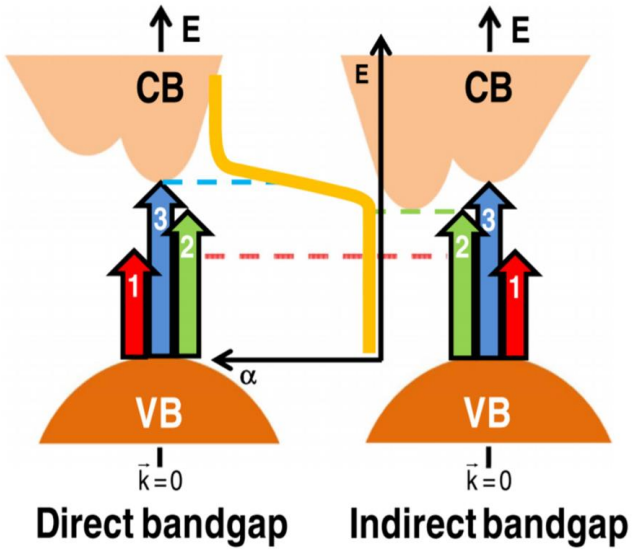

Figure 1.6 A schematic that shows the direct band to band transition and indirect band to band transition in semiconductor solids. 1 – below bandgap and thus no absorption; 2 – absorption onset (due to the assist of phonons in indirect bandgap semiconductors or defects in direct bandgap semiconductors); 3 – high absorption edge. (Reproduced with permission from [96], Nature Publishing Group, Copyright 2019.)

gap energy can ensure that large number of electron-hole pairs can be produced to achieve a better detector energy resolution (which is again defined as the full-width-at-half-maximum (FWHM) of the photo-peak over the peak centroid). The electron-hole pair creation energy W (eV) is related with the band gap energy in the below empirical formula [36],

$$W=2E_g + 1.43 \qquad (5)$$

where E_g is the band gap energy.

Another important figure-of-merit for evaluating the materials potential as semiconductor detector materials is the mobility-lifetime (μ-τ) product. Mobility is defined as the

drift velocity per unit of electric field and possesses the unit of cm^2/V-s. Under the applied electric field E (V/cm), the drift distance λ (cm) of charge carriers is given by,

$$\lambda = \mu\tau E \qquad (6)$$

where λ has the unit of centimeter and τ is the lifetime (the time from charge carrier creation to the recombination of charge carriers) of charge carriers (electrons or holes). In general, to achieve a better charge collection efficiency (CCE), higher mobility and mobility-lifetime product are desired. Mobility-lifetime (μ-τ) product can be evaluated using the Hecht model [37],

$$\mathrm{CCE} = \eta(x) = \frac{(\mu\tau)_e E}{d}\left(1 - \exp\left(-\frac{d-x}{(\mu\tau)_e E}\right)\right) + \frac{(\mu\tau)_h E}{d}\left(1 - \exp\left(-\frac{x}{(\mu\tau)_h E}\right)\right) \qquad (7)$$

where CCE represents charge collection efficiency and d is the detector thickness, E is the applied electric field. Eqn. 7 can be applied for the situation that gamma photons are incident on the cathode and charge carriers are produced at position x (which is the distance from negative electrodes). $(\mu\tau)_e$ and $(\mu\tau)_h$ in eqn. 7 could be exchanged if gamma rays are incident on the positive electrode [37]. If radiation with weak penetrating capability (e.g., low-energy X-rays, alpha particles) rather than gamma rays is incident on the electrodes, charge carriers will mostly be produced near the surface of the detector. Therefore, single charge carriers will travel the entire detector length from electrode to electrode. This allows us to determine the $(\mu\tau)_e$ and $(\mu\tau)_h$ separately. In this scenario, the mobility-lifetime product for single charge carriers can be determined using [38],

$$\frac{Q}{Q_0} = \frac{\mu\tau E}{d}\left[1 - \exp\left(-\frac{d}{\mu\tau E}\right)\right] \qquad (8)$$

where Q/Q_0 is the charge collection efficiency. There is another way to determine the μ-τ product, which can be extracted from Many's equation [39] or modified Hecht model. In this dissertation, Many's equation was used to determine the μ-τ product of charge carriers in $Cs_2AgBiBr_6$ single crystals.

The mobility and lifetime also can be evaluated separately using several techniques. To characterize the charge carrier mobility, space charge limited current (SCLC) method could be used (eqn. (20) in Chapter 4). Hall effect measurement is another technique to determine the free carrier mobility. In the Hall effect experiment, both electrical and magnetic fields are applied to measure the behaviors of charge carriers inside the semiconductors. The principle of Hall effect is that the Lorentz force induced by the magnetic field on moving charge carriers could deflect the moving paths of charge carriers and eventually is counter balanced by the produced Hall voltage V_H (due to the accumulation of charge carriers on one side). Therefore, a steady state could be reached. Equations are then set for solving to find the charge carrier mobility. Free carrier mobility in Hall measurement could be described using,

$$\mu_H = \frac{|V_H d|}{BI\rho} \qquad (9)$$

in which V_H is the Hall voltage, d is the sample thickness, B is the applied magnetic field, I is current, and ρ is the semiconductor resistivity. Hall effect is also very useful for finding the conduction type of semiconductors as the majority charge carrier holes for p-type semiconductor and electrons for n-type semiconductors will deflect along opposite directions, thus the sign of Hall voltage will be different. Charge carrier concentration and resistivity of semiconductor solids could be determined using Hall effect measurement as well.

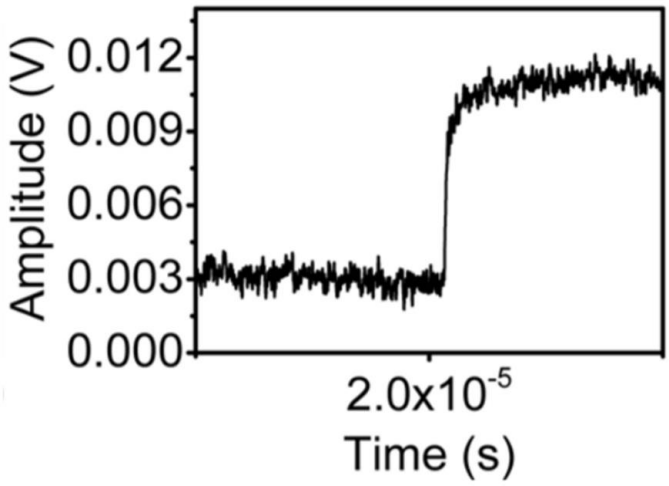

Figure 1.7 A ToF pulse trace for electrons using $TlSn_2I_5$ detector, measurement was performed using ^{241}Am alpha source at 100 V bias. (Reproduced with permission from [100], American Chemical Society, Copyright 2017.)

The third method to characterize carrier mobility is time-of-flight (ToF) technique. Free carrier mobility in ToF method could be determined by,

$$\mu = \frac{v}{E} \qquad (10)$$

E is the applied electric field (V/cm), and v is the velocity of charge carriers, which can be calculated by using d/t (d: detector thickness, t: transient time, transient time t can be read from the ToF pulse traces). Figure 1.7 shows the ToF electron pulse trace for $TlSn_2I_5$ detector. The pulse trace was induced by ^{241}Am alpha source at 100 V bias. To determine the electron rise time (or transient time in eqn. (10)) from Figure 1.7, one can use the time interval between 10% and 90% of the maximum charge collected. Another method to estimate the electron rise time is to determine the time needed from no charge collected to 50% of the maximum charge collected. The electron rise time then is two times the time needed from no charge collected to 50% of the maximum charge collected. For Figure 1.7, the electron rise time is ~1.06 μs. Because the

detector is ~0.1 cm thick, the velocity of electrons then can be obtained. This gives the mobility of electrons of $TlSn_2I_5$ to be ~94 cm^2/V-s [100].

In ToF method, the drift mobility remains as a function of intrinsic charge carrier concentrations, the determined mobility thus is not as accurate as the one which is determined from SCLC technique. Besides, the drift mobility determined using ToF method is device-oriented and thus is very useful for device characterizations [87]. The SCLC technique and Hall measurement are more commonly used for evaluating the quality of new materials. It also should be noted that the drift mobility determined using eqn. (20) or eqn. (10) usually differs from the one that is determined from eqn. (9) Hall mobility. This difference originates from the different scattering mechanisms (e.g., ionized-impurity scattering, lattice scattering). At low electrical fields, charge carriers are almost in equilibrium with lattice vibrations and mainly undergo phonon and Coulomb scattering [88]. However, at high electrical fields, the mobility becomes a field-dependent parameter. Further, in Hall effect measurement, the scattering of charge carriers could be affected by the applied magnetic field.

The lifetime of charge carriers for single crystals could be determined using the time-resolved photoluminescence (TRPL), shown in Figure 1.8. In time-resolved PL, there are two lifetime contributions from the fitting curve, short-lived PL lifetime and long-lived PL lifetime. The short-lived PL lifetime corresponds to the lifetime for surface recombination, while the long-lived PL lifetime reflects the charge carrier lifetime inside the bulk single crystals. Figure 1.6 shows the TRPL measurement for $MAPbCl_3$ single crystals. The TRPL trace can be fitted using the below multi-exponential equation [89],

$$R(t) = B_1 e^{(-t/\tau_1)} + B_2 e^{(-t/\tau_2)} + B_3 e^{(-t/\tau_3)} + B_4 e^{(-t/\tau_4)} \qquad (11)$$

The fitting yields the short-lived PL lifetime (τ_1) of charge carriers due to surface recombination to be 1.4137 ns, while the long-lived PL lifetime (τ_2) of charge carriers inside the bulk single crystals is 6.8684 ns. Here, only the first two parts (τ_1 and τ_2) of equation (11) was used for fitting.

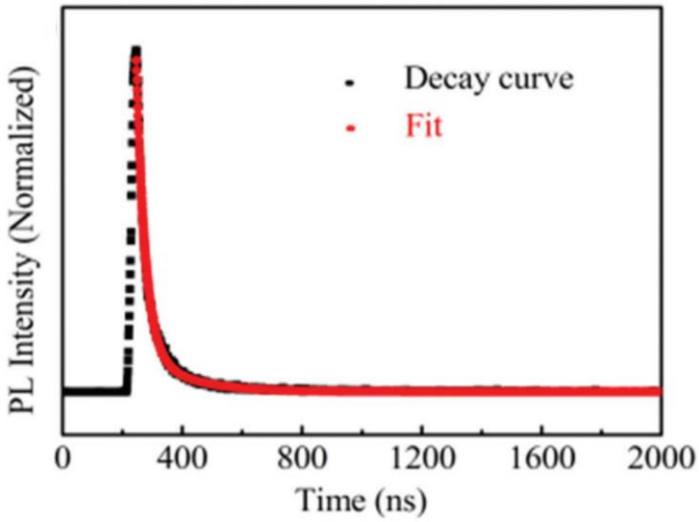

Figure 1.8 Time-resolved photoluminescence (PL) measurement of $MAPbCl_3$ single crystals. (Reproduced with permission from [89], Royal Society of Chemistry, Copyright 2019.)

Finally, low fabrication cost is desirable when searching for ideal radiation detector materials. For market competition, perovskite single crystals have a great advantage which is that they can be grown from aqueous solutions. The single crystal solution growth methods will be explained and discussed in chapter 2. One benefit of the solution growth techniques is the fabrication cost is very low. Raw chemicals for synthesizing using solution growth methods can be purchased from vendors such as Sigma Aldrich and Fisher Scientific. We estimate the materials cost to grow $Cs_2AgBiBr_6$ double perovskite single crystals is ~ \$6/cm^3, which could be cheaper if lower purity raw chemicals are used. In comparison with solution-growth, melt growth methods are another class of single crystal fabrication methods for today's leading room-temperature semiconductor detector materials cadmium zinc telluride (CdZnTe) and its low-cost

Table 1.1 Room-temperature properties of common semiconductor materials for X-ray and gamma-ray detectors. [101-103]

Material	Atomic Number	Density (g/cm^3)	Band Gap (eV)	E_{pair} (eV)	Resistivity ($\Omega \cdot cm$)	$\mu\tau$ (e) product (cm^2V^{-1})	$\mu\tau$ (h) product (cm^2V^{-1})
Si	14	2.33	1.12	3.6	10^4	4×10^{-1}	2×10^{-1}
Ge	32	5.33	0.66	2.96	50	1	1
GaAs	31, 33	5.32	1.43	4.2	10^{11}	10^{-2}	5×10^{-4}
InP	15, 49	4.78	1.34	4.2	10^6	5×10^{-6}	$<2\times10^{-5}$
CdTe	48, 52	6.2	1.44	4.4	10^9	3×10^{-3}	2.6×10^{-4}
$Cd_{0.9}Zn_{0.1}Te$	48, 30, 52	5.78	1.57	4.6	10^{11}	10^{-2}	10^{-4}
PbI_2	82, 53	6.2	2.3-2.6	4.9	10^{12}	8×10^{-6}	9×10^{-7}
HgI_2	80, 53	6.4	2.13	4.2	10^{13}	10^{-4}	4×10^{-5}
TlBr	81, 35	7.56	2.68	6.5	10^{12}	3×10^{-5}	1.5×10^{-6}

alternative cadmium zinc telluride selenium (CdZnTeSe) single crystals. Melt growth methods usually costs more (e.g., optical furnaces are required in floating zone method) and requires higher temperatures above the melting point of raw chemicals (e.g., as synthesizing raw chemicals of $CsPbBr_3$ single crystal, T_{melt} of CsBr and $PbBr_2$ are 636 ^{0}C and 373 ^{0}C respectively).

Table 1.1 summarized the properties of some of the compound and single element semiconductor solids for X-ray and gamma-ray detection use. As mentioned, the germanium detectors offer the best-in-class energy resolution due to their superior mu-tau products for both electrons and holes. The CZT single crystals are today's leading compound semiconductor materials for room-temperature gamma-ray detection, while the CZT still suffers from the poor hole transport due to the low mu-tau product for holes.

1.5 Materials Selection

Even though many single element and compound solids have potentials to serve as next-generation room-temperature semiconductor detector materials, very few of them have been systematically studied to date. Perovskites are a big family and were only recently re-discovered. Thus, revealing of the unique properties of perovskite single crystals still requires many efforts and input.

In this work, the all-inorganic $Cs_2AgBiBr_6$ double perovskite single crystals were selected for detailed investigations. This material was chosen for the following reasons: Firstly, $Cs_2AgBiBr_6$ has large average atomic number (Cs = 55, Ag = 47, Bi = 83) and high density (4.65 g cm^{-3}). Large average atomic number implies high mass attenuation coefficients, which is especially important for the development of X-ray and gamma-ray radiation detectors. High density leads to a much larger intrinsic efficiency, which is defined as the ratio of counts under the photo-peak to the photons interacting with the detector. Secondly, previously reported humidity and thermal stability tests confirmed the high moisture and heat resistance capabilities of $Cs_2AgBiBr_6$ [68], which offer potentials for long-term and stable device operation. More importantly, this crystal does not contain lead, which eliminates the use of toxic heavy metal in the case of hybrid lead halide perovskites. We note the solubility constant of AgBr is approximately four orders of magnitude lower than that of PbI_2 [69]. Finally, previous work by Hoye et al. indicated fundamental carrier lifetime in $Cs_2AgBiBr_6$ thin films can exceed 1 μs, which is even longer than the carrier lifetime in $FAPbI_3$ and CdTe bulk single crystals (484 ns and ~150 ns respectively) [31, 70, 71]. In combination with a suitable charge carrier mobility, the possible large mobility-lifetime product could enable a more efficient charge collection at lower bias voltages using $Cs_2AgBiBr_6$ single crystals.

It should also be noted that the optical band gap energy is another important criterion for the selection of materials. $Cs_2AgBiBr_6$ has indirect band gap energy of 1.95 eV and direct band gap energy of 2.21 eV [47]. This would give electron hole pair creation energy of ~ 5.33 eV according to the empirical equation (5) (E_g=1.95 eV is used for calculation), which makes $Cs_2AgBiBr_6$ suitable for further studies as radiation detector materials.

Chapter 2: Single Crystal Growth

2.1 Perovskite Single Crystal Growth Methods

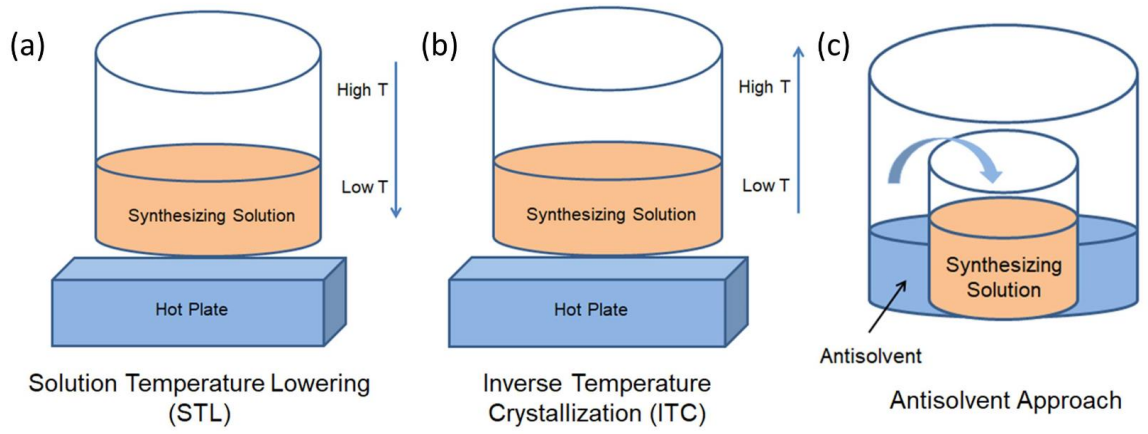

Figure 2.1 Illustration of the (a) STL (b) ITC and (c) anti-solvent methods for growing perovskite single crystals.

Both solution growth and melt growth methods have been employed for producing large-sized perovskite single crystals. Perovskite single crystals can be grown from aqueous solutions, which generally can be classified into four types of solution-growth methods: 1) inverse-temperature crystallization, known as ITC technique (Figure 2.1 (b)). In the ITC method, the principle is raw synthesizing chemicals have high solubility in organic solvents (e.g., γ-butyrolactone (GBL) and N,N-dimethylformamide (DMF)) at low temperatures. Therefore, raw chemicals could be dissolved in solvents at room temperature and then the solution temperature can be gradually increased to reach saturated state for single crystals to form. 2) slow cooling method (Figure 2.1 (a)), in which solution temperature is lowered down from high temperatures so that saturated state could be reached and therefore single crystals start to form. 3) anti-solvent approach (Figure 2.1 (c)), in which an organic solvent (e.g., methanol, ethanol, toluene) is usually used to slowly diffuse into the synthesizing solution to precipitate single crystals. 4) solvent evaporation method. In this technique, some organic solvents (e.g., GBL, dimethyl

sulfoxide (DMSO)) can be used for dissolving the raw synthesizing chemicals. The mixed solution is then exposed at room temperature for slow evaporations. Perovskite single crystals usually can be obtained after weeks. Using ITC technique, solution growth of millimeter-sized $MAPbI_3$ and $MAPbBr_3$ single crystals (Figure 2.2 (a) and (b)) could be achieved within a few hours, as demonstrated in Saidaminov et al. work [40]. Compared with the ITC technique, the slow cooling method or solution temperature lowering (STL, [41]) method is a traditional technique and usually takes days compared with ITC method to produce high-quality single crystals. With this method, Dang et al. lowered the solution temperature down from 65 °C to 40 °C and produced 10mm×10 mm×8 mm $MAPbI_3$ single crystal after days [42].

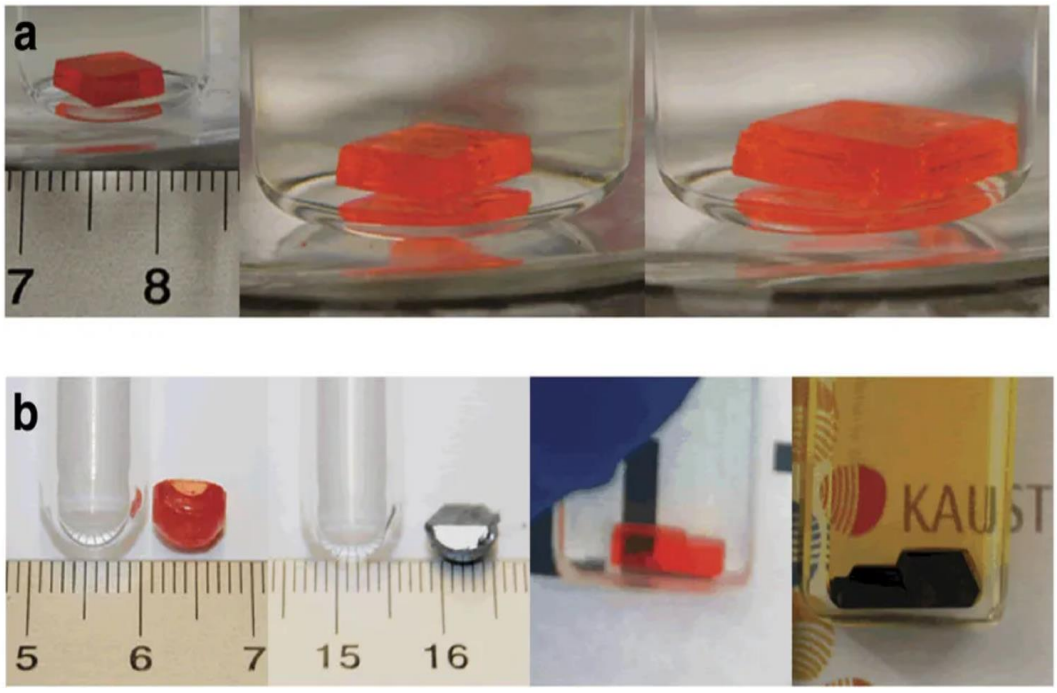

Figure 2.2 (a) and (b) $MAPbBr_3$ single crystal (orange), placed near a millimeter ruler. $MAPbI_3$ single crystal (black), grown by ITC technique. (Reproduced with permission from [40], Nature Publishing Group, Copyright 2015.)

Melt growth methods (e.g., Bridgman, optical floating zone) also have been used to grow perovskite single crystals with suitable size for characterizations [21, 43, 44]. In the Bridgman

technique, the seed crystal sits in a container, which is either a graphite crucible with tight lid or a sealed quartz ampoule [45]. The container is filled with inert gas (e.g., Ar) at high pressure to suppress the loss of volatile components. It moves along the region which has a temperature gradient (above and below the melting point). The seed crystal grows in a colder region along with the movement of the container. High pressure Bridgman (HPB) could be implemented in both vertical and horizontal orientations and large CdZnTe ingots (up to 10 kg in weight) can be acquired using this technique, though crystals from HPB are polycrystalline with large grains and they tend to suffer from macroscopic cracking and pipe defects [45, 46]. Using this method, He et al. mixed the polycrystalline CsBr and $PbBr_2$ (1:1 stoichiometric ratio) at 580 ℃ in a sealed

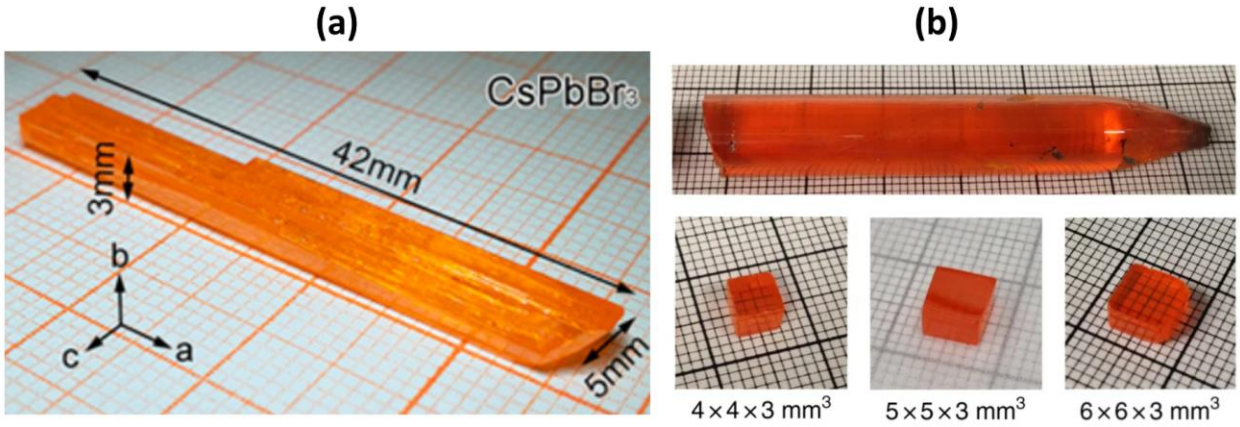

Figure 2.3 (a) $CsPbBr_3$ single crystals, grown using anti-solvent approach. (Reproduced with permission from [33], American Chemical Society, Copyright 2017.) (b) $CsPbBr_3$ single crystals, grown from Bridgman technique. (Reproduced with permission from [21], Nature Publishing Group, Copyright 2018.)

fused silica tube. The silica tube was placed in a vertical furnace and heated to 580 ℃. Then, it was moved downwards to pass the temperature gradient region for the single crystals to precipitate. The produced $CsPbBr_3$ ingot is 11 mm in diameter, 3mm in thickness, and 65 mm in

length (Figure 2.3 (b)). Figure 2.3 (a) shows the $CsPbBr_3$ single crystals, grown by anti-solvent approach.

2.2 Growth of $Cs_2AgBiBr_6$ Single Crystals

In this dissertation, the $Cs_2AgBiBr_6$ single crystal was grown using solution-processing technique. We adopted and then modified the STL method which was reported previously by Slavney et al. [47, 48]. The crystal growth was started by first dissolving 2.0 mmol CsBr (99.999%, Sigma Aldrich) and 1.0 mmol $BiBr_3$ (99.999%, Sigma Aldrich) in 10 mL HBr acid (99.9999%, 48% w/w, Alfa Aesar) at room temperature. 1.0 mmol AgBr (99.998%, Alfa Aesar) was then added and the solution was briefly stirred. Then the vial containing this solution was placed on top of a hotplate, which has been pre-heated to 120 °C. The solution temperature was maintained at this temperature until the solution was clear and transparent. The temperature was then decreased at a controlled rate of 2 °C h^{-1}. Temperature was unchanged overnights to promote the crystal growth. This process generally takes 4 days to complete. Once the crystal growth ends, the solution was filtered using polytetrafluoroethylene (PTFE) filters. The as-grown crystals were carefully handled and washed using ethanol to remove chemical residues on the surface. In this work, a crystal in one centimeter size was able to be synthesized, however its shape was irregular (i.e., octahedral shape). The above described process will be referred as bismuth-normal (Bi-normal) solution growth for $Cs_2AgBiBr_6$ single crystals in this dissertation. Figure 2.4 shows the as-grown fresh $Cs_2AgBiBr_6$ single crystals using Bi-normal solution growth method. The shown crystals are approximately 5mm×5mm×4mm (x, y, z) large.

It was previously theoretically reported that the bismuth ratio in synthesizing solutions could affect the $Cs_2AgBiBr_6$ single crystal qualities [49]. In theory, the undesirable deep electron

(a) (b)

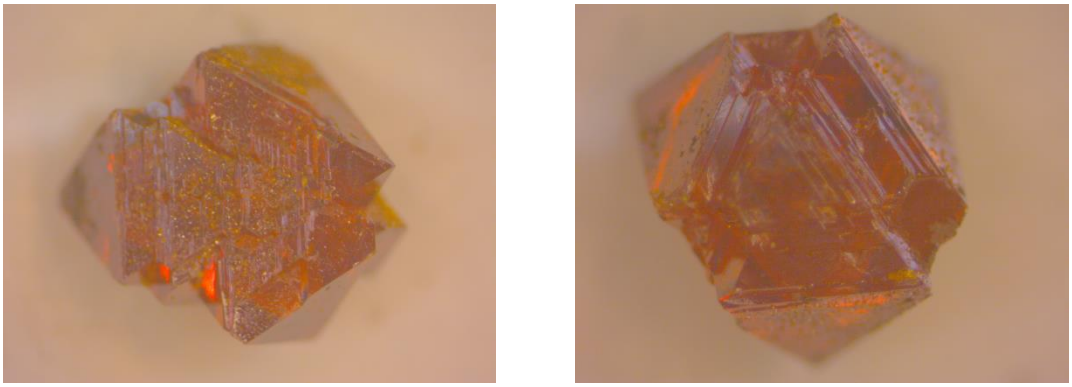

Figure 2.4 (a) and (b) Pristine $Cs_2AgBiBr_6$ single crystals grown using Bi-normal solution growth method.

trapping sites bromide (Br) vacancy defects and Bi_{Ag} (bismuth cations on silver cations) antisite substitutions could be dramatically suppressed if single crystals are synthesized from bismuth-poor (Bi-poor) and bromide-rich (Br-rich) solutions. To verify the theoretical study, we synthesized the $Cs_2AgBiBr_6$ single crystals from Bi-poor solutions. Essentially, same temperature control and lowering was used as the Bi-normal solution growth process. However, the synthesizing ratio of CsBr, AgBr, and $BiBr_3$ is 2:1:0.8. In Bi-normal experiment, the synthesizing ratio of raw chemicals is 2:1:1 ($CsBr:AgBr:BiBr_3$). Figure 2.5 (a) and (b) schematically illustrates the single crystal growth processes for Bi-normal and Bi-poor $Cs_2AgBiBr_6$ solution growth. The grown single crystals are in octahedral shape with four crystal surfaces surrounding one peak point, shown in Figure 2.5 (c)-(f). Comparing the Bi-normal and Bi-poor $Cs_2AgBiBr_6$ single crystals, it is observed that Bi-normal single crystals are darker with a dark brown color. The Bi-poor single crystals show a more clear red brown color. Single crystals grown from Bi-poor solutions seem to be more transparent compared with the ones synthesized from Bi-normal solutions.

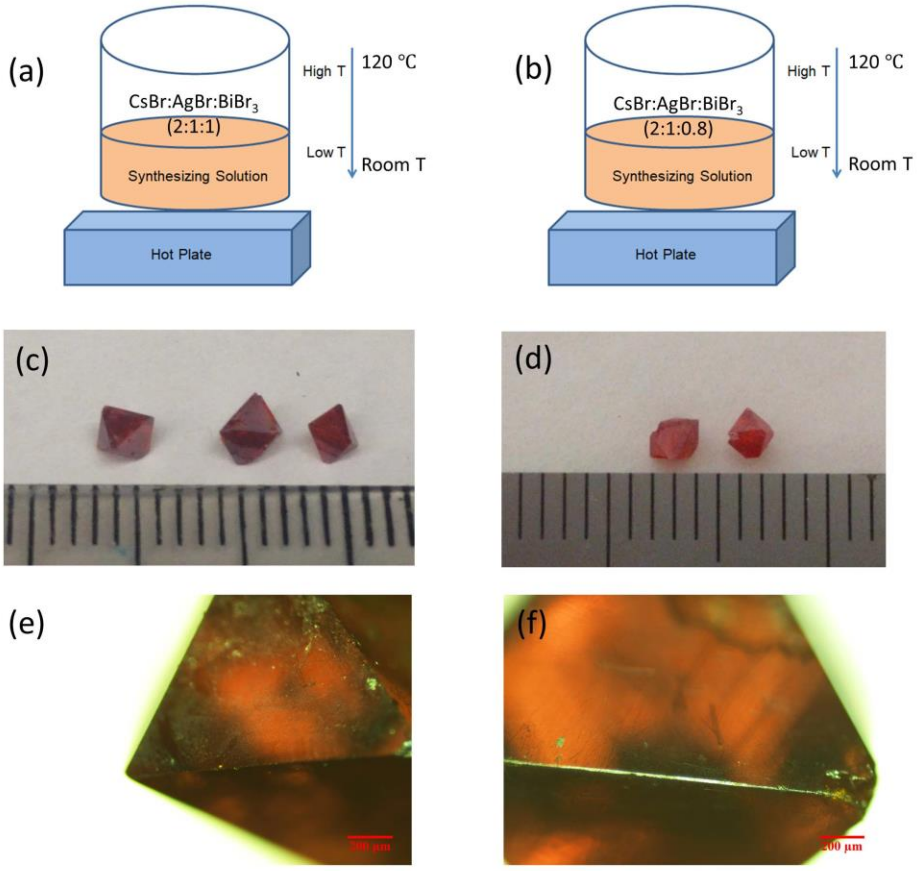

Figure 2.5 (a) Schematic illustration of the Bi-normal and (b) Bi-poor $Cs_2AgBiBr_6$ crystal growth processes. As-grown (c) Bi-normal and (d) Bi-poor $Cs_2AgBiBr_6$ single crystals. (e) Photographs of Bi-normal and (f) Bi-poor $Cs_2AgBiBr_6$ single crystals under Nikon optical microscope.

Chapter 3: Device Fabrication

Part of this chapter is published in *Journal of Materials Science: Materials in Electronics* [1].

3.1 Crystal Surface Processing Techniques

Hybrid MA and FA-based perovskites usually have two natural planar parallel crystal surfaces which allow direct device fabrication. Either low work function metals (e.g., Ag, Al, In) or high work function metals (e.g., Au) could be selected for electrodes deposition on the two parallel crystal surfaces. Nevertheless, before depositing certain metal electrodes, the crystal surface usually requires further processing. The as-grown single crystals typically carry many impurities from synthesizing solutions. Besides, pristine crystals usually have a certain level of surface defects which could serve as trapping sites for charge carriers, thus consequently affecting the charge extraction. To reduce the number of undesirable surface trapping sites, organic solvents (e.g., ethanol, methanol, acetone, DMF) could be applied to soak the as-grown single crystals for a short period. Ethanol and acetone can evaporate quickly and therefore would not affect the surface conditions. In addition to using organic solvents to wash single crystals, vapor surface treatment could also be used. Zhou et al. placed $MAPbI_3$ single crystals on top of a vial which contains 40% CH_3NH_2 aqueous solutions [51]. It was noted that the broadband photo-response in pristine $MAPbI_3$ single crystals was found to be narrower after vapor treatment. This indicated the vapor-treated single crystal has a better quality compared with pristine crystals and surface traps were effectively passivated.

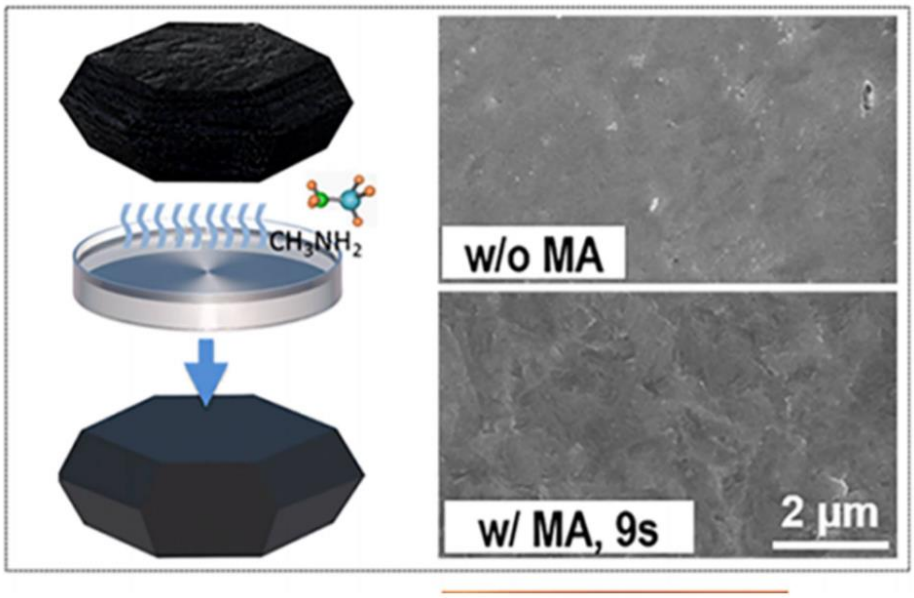

Figure 3.1 Illustration of the CH_3NH_2 gas treatment for $MAPbI_3$ single crystals, right shows the scanning electron microscopy (SEM) images without and with CH_3NH_2 gas treatment. (Reproduced with permission from [51], American Chemical Society, Copyright 2018.)

In the development of X-ray detectors using $MAPbBr_3$ single crystals, Wei et al. employed the ultraviolet-ozone (UV-O_3) technique to treat as-grown $MAPbBr_3$ single crystals [52]. The UV-O_3 method is very effective in removing organic contaminants, but not inorganic impurities. This technique applies the principle that the organic contaminants could be decomposed by ultraviolet rays and the excited contaminants then can react with atomic oxygen to form H_2O, CO_2, and etc. These volatile substances thus can be easily removed from crystal surfaces. By treating $MAPbBr_3$ single crystals for 20 mins, Wei et al. noticed the photoluminescence (PL) intensity was dramatically enhanced. In addition, the surface recombination velocity of passivated single crystals revealed by the recorded photocurrent data is 64 cm/s, which is 18 times slower than the pristine $MAPbBr_3$ single crystals. The photocurrent data was fitted by Many's equation (eqn. 20 in chapter 4) and thus the surface recombination velocity could be extracted. The dramatic lower surface recombination velocity in passivated

$MAPbBr_3$ single crystals compared with that in pristine ones demonstrated surface passivation methodology is a workable technique and could be similarly applied to treat other hybrid perovskite single crystals to enhance the response to gamma ray.

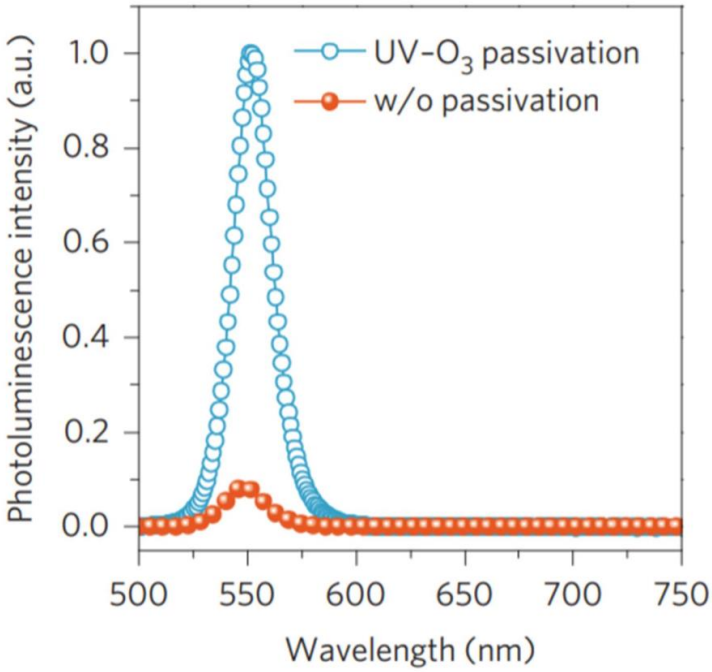

Figure 3.2 Photoluminescence (PL) spectra of $MAPbBr_3$ single crystals before and after UV-O_3 surface passivation. (Reproduced with permission from [52], Nature Publishing Group, Copyright 2016.)

3.2 Fabrication of $Cs_2AgBiBr_6$-Based Detectors

In this dissertation, we first polished the as-grown Bi-normal $Cs_2AgBiBr_6$ single crystals to achieve two parallel surfaces for electrodes deposition. To fulfill this purpose, rinsed Bi-normal $Cs_2AgBiBr_6$ were taken to analytical instrumentation facility (AIF) at NCSU. Crystals were carefully polished using silicon carbide (SiC) grinding paper using the Allied Multiprep polishing station. To ensure two parallel surfaces were created, polished crystal surfaces were examined under optical microscope. It has to note that evidences have been found that halide

ions in some hybrid perovskites could diffuse and react with certain metal electrodes (e.g., Ag, Al) [53, 54]. In this work, we selected Au (with the assumption that it will not react with $Cs_2AgBiBr_6$ double perovskites) for electrodes deposition on the two polished surfaces of one Bi-normal $Cs_2AgBiBr_6$ single crystal. Two 50 nm thick Au electrodes were deposited onto the two parallel surfaces of one single crystal (referred to as Au/$Cs_2AgBiBr_6$/Au device) for electrical measurements using electron beam evaporation with a base chamber pressure of 1×10^{-7} Torr and deposition rate of 1 Å/s. Figure 3.3 is a schematic illustration of the $Cs_2AgBiBr_6$ single crystals-based devices with electrodes deposited for follow-on measurements. Silver is added in Figure 3.3 as we have also tried brushing silver paste directly on the two sides of one single crystal for electrical measurements.

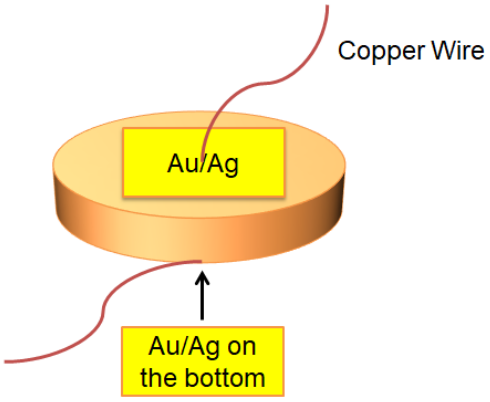

Figure 3.3 Schematic illustration of the $Cs_2AgBiBr_6$ single crystals-based devices for electrical measurements and radiation response testing

For the comparison study between Bi-normal and Bi-poor $Cs_2AgBiBr_6$ single crystals, we did not perform surface polishing owing to the possible induced surface damage by SiC grinding paper. The induced surface damage from the polishing process could slightly affect the electrical measurements. On the other hand, as-grown two crystal surfaces were selected for direct Ag electrodes deposition. The silver paste (Fast Drying Silver Paint, purchased from Ted Pella, INC.)

was manually brushed on the crystal surfaces. It has to note that selected two crystal surfaces are near parallel but are not perfectly parallel (due to the natural octahedral shape of $Cs_2AgBiBr_6$) as that in the polished single crystals. The non-parallel crystal surfaces could have slightly affected the uniformity of electrical field during the measurements, though here it is assumed that it has no influence.

Chapter 4: Materials Characterization

Part of this chapter is published in *RSC Advances* and *Materials Letters* [48, 50]. Part of this chapter is under revision at *Advanced Optical Materials* [76].

In this chapter, sections 4.1 - 4.8 reported the characterized physical, optical, and electrical properties of Bi-normal $Cs_2AgBiBr_6$ single crystals using the device structure of either Au/$Cs_2AgBiBr_6$/Au or Ag/$Cs_2AgBiBr_6$/Ag. Comparison study in material properties between Bi-normal and Bi-poor $Cs_2AgBiBr_6$ single crystals was made from section 4.9.

4.1 Photon Attenuation

Characterization of $Cs_2AgBiBr_6$ compound single crystals for radiation detection was started by first showing its photon attenuation capabilities for X-ray and gamma ray. $Cs_2AgBiBr_6$ has large average atomic number (Cs = 55, Ag = 47, Bi = 83) and high density (4.65 g/cm^3). The attenuation capability of $Cs_2AgBiBr_6$ is comparable to the leading room-temperature semiconductor detector materials CdZnTe and CdTe, as can be seen in Figure 4.1 (data is available online in XCOM photon cross section database). This lays foundation for the further investigation of using $Cs_2AgBiBr_6$ single crystals for X-ray and gamma photon detection. In addition, as mentioned in the Introduction section, high average atomic number Z of 45 for ensuring large stopping power for alpha particle detection.

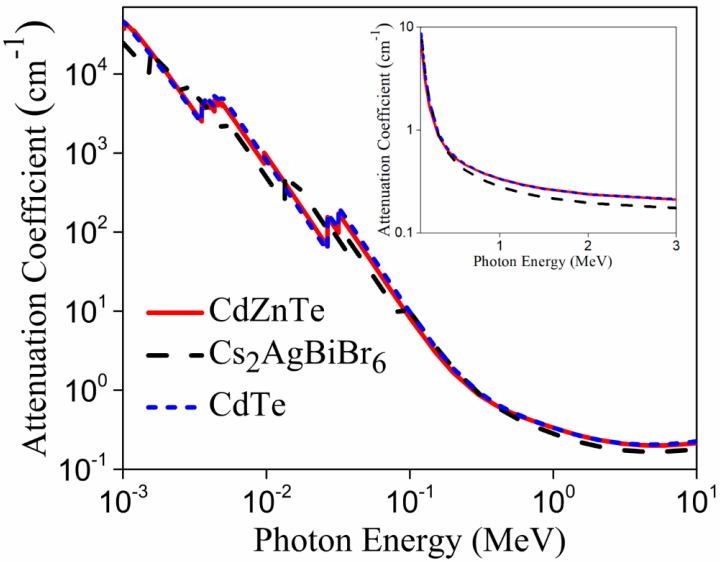

Figure 4.1 Attenuation coefficient of CdZnTe, $Cs_2AgBiBr_6$, and CdTe crystals as a function of photon energy, from soft X-ray to high energy gamma-rays. Inset plot shows the attenuation coefficient as a function of photon energy, from 0.1 MeV to 3 MeV.

4.2 X-Ray Diffraction Pattern

X-ray diffraction (XRD) experiment was carried out using a Rigaku SmartLab X-ray diffractometer with CuKα1 X-ray (wavelength=1.5406 Å) source at AIF of NCSU. We observed the peaks from one set of parallel lattice planes from the typical as-grown bulk Bi-normal $Cs_2AgBiBr_6$ single crystal. The obtained XRD pattern shown in Figure 4.2 matches well with the $Cs_2AgBiBr_6$ reference pattern in the database (ICSD collection #252164). This confirms that the as-grown single crystals in our solution growth process is indeed $Cs_2AgBiBr_6$ phase.

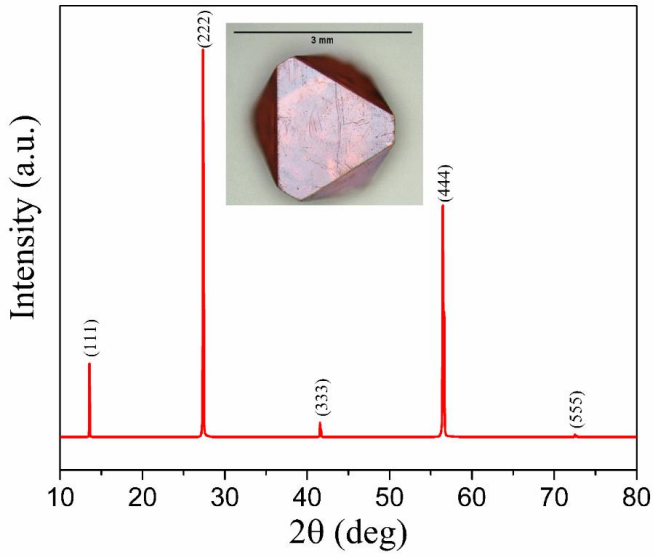

Figure 4.2 X-ray diffraction (XRD) pattern of $Cs_2AgBiBr_6$ single crystal grown with our solution process. The inset is a picture of a typical as-grown single crystal.

4.3 Current-Voltage (I-V) Characteristic

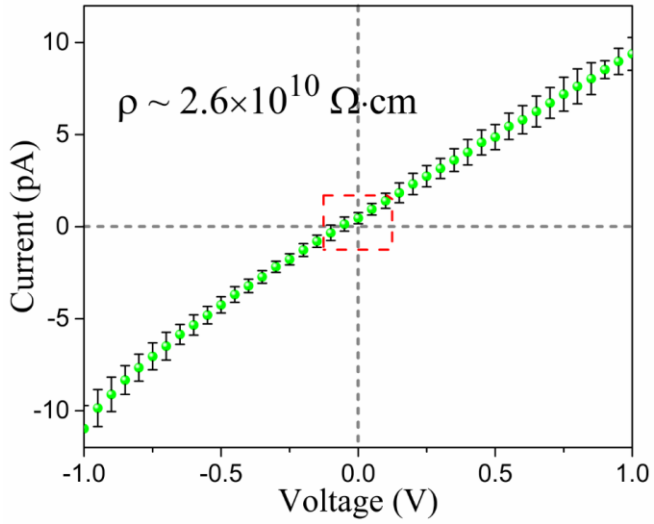

Figure 4.3 Current-voltage (I-V) curve of $Cs_2AgBiBr_6$. Measurement was conducted at room temperature (19 ℃). Note the curve does not pass origin, probably indicating the existence of weak Schottky barrier.

Figure 4.3 shows the current-voltage (I-V) curve of $Cs_2AgBiBr_6$ single crystals, measured using Keithley 6487 picoammeter/voltage source. Voltage was set from −1 V to 1 V with step 0.05 V and one second for each step. The pre-installed software in excel was used for initial picoammeter parameter settings and recording the current at different bias voltages. Silver paste was brushed on the two opposite single crystal surfaces for I-V measurement. The determined resistivity of $Cs_2AgBiBr_6$ is 2.6×10^{10} Ω·cm. Such a high resistivity will ensure low leakage current for the fabrication of high performance semiconductor-based radiation devices. It was noted that the I-V curve in Figure 4.3 did not pass the origin. Though crystal surfaces have been rinsed with ethanol, certain level of surface defects should remain presenting on the $Cs_2AgBiBr_6$ single crystal surfaces. This therefore creates a very weak Schottky barrier, which caused that the I-V curve did not pass the origin. It is also reasonable to doubt that the I-V hysteresis shown here is partially contributed by the halide bromide ion migrations. It is possible that the surface defects are playing a much important role than the ionic migrations. This is judged by the high surface recombination velocity of 2367.6 cm/s, determined by the Many's equation fitting for laser-induced current at different bias voltages (shown in section 4.7).

4.4 Temperature-Dependent Resistivity

Temperature-dependent resistivity measurement was performed from 266 K to 292 K (-7 ℃ to room temperature 19 ℃). Same experimental setup that was used for I-V measurement above was used here, but with temperature-control capabilities. Figure 4.4 (a) showed the I-V curves acquired at the above mentioned temperature range. Figure 4.4 (b) is a plot which showed the resistivity versus temperatures for $Cs_2AgBiBr_6$. The resistivity plot in Figure 4.4 (b) follows

the classical semiconductor behaviors. In other words, the resistivity will decrease with the increase of temperature owing to the presence of more thermally excited charge carriers.

(a) (b)

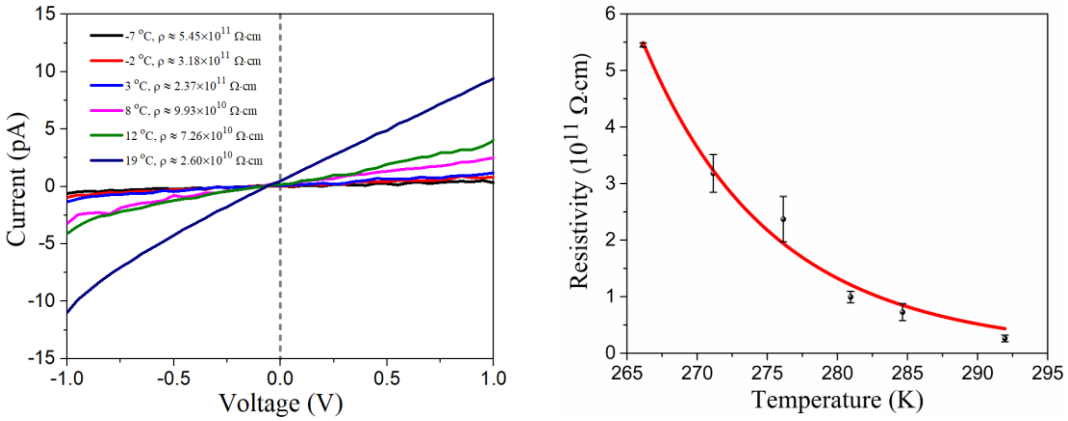

Figure 4.4 (a) and (b) I-V curves and the resistivity of $Cs_2AgBiBr_6$ single crystal at different temperatures.

Temperature-dependent resistivity can also help determine the Fermi level. The Fermi level is a hypothetical energy level where electrons have 50% probability to occupy under thermodynamic equilibrium. For semiconductors, the resistivity ρ can be expressed in the following way [55, 56],

$$\rho = \frac{1}{q(\mu_e n + \mu_h p)} \qquad (11)$$

where q is the electron charge (1.602×10^{-19} C), n and p are electron and hole concentrations, μ_e and μ_h are electron and hole mobilities respectively. In Boltzmann relations, the electron and hole concentrations are given by,

$$n = N_c \exp(-\frac{E_c - E_F}{kT}) \qquad (12)$$

$$p = N_v \exp(-\frac{E_F - E_v}{kT}) \qquad (13)$$

where N_c and N_v are effective density of states in conduction band and valence band respectively, E_c and E_v are edges of the conduction band and valence band, E_F is the Fermi level, k is the Boltzmann constant. Therefore, we can substitute equations (12) and (13) into equation (11),

$$\rho = \frac{1}{q(\mu_e N_c \exp(-\frac{E_c - E_F}{kT}) + \mu_h N_v \exp(-\frac{E_F - E_v}{kT}))} \qquad (14)$$

In p or n type semiconductors, there is large difference between carrier densities. Thus,

$$\rho \approx \frac{1}{q\mu_e N_c \exp(-\frac{E_c - E_F}{kT})} \text{ (n-type)} \quad \text{or} \quad \rho \approx \frac{1}{q\mu_h N_v \exp(-\frac{E_F - E_v}{kT})} \text{ (p-type)} \qquad (15)$$

Additionally, since the temperature range is narrow (265 K to 292 K), N_c, N_v, μ_e, μ_h can be treated as constants with no variations. Therefore, by taking logarithmic transformation, the Fermi level position can be determined using,

$$\ln(\rho) = \frac{\Delta E}{kT} + constants \qquad (16)$$

For p-type semiconductor, ΔE refers to the position of Fermi level above the valence band. For n-type semiconductor, ΔE refers to the position of Fermi level below the conduction band.

Using the obtained temperature-dependent resistivity data, we determined the Fermi level position to be either 0.788 eV below the conduction band (n-type) or above the valence band (p-type), as shown in Figure 4.5 (a). Since the as-grown Bi-normal $Cs_2AgBiBr_6$ single crystals are p-type (judged by the positive Seebeck coefficient), Fermi level therefore lies in the position of 0.788 eV above the valence band, as shown in Figure 4.5 (b). This determination of Fermi level position could serve as a guidance for the further study of the possible Fermi level pinning phenomenon in $Cs_2AgBiBr_6$ single crystals, which could help the interpretation of deep level defects.

(a) (b)

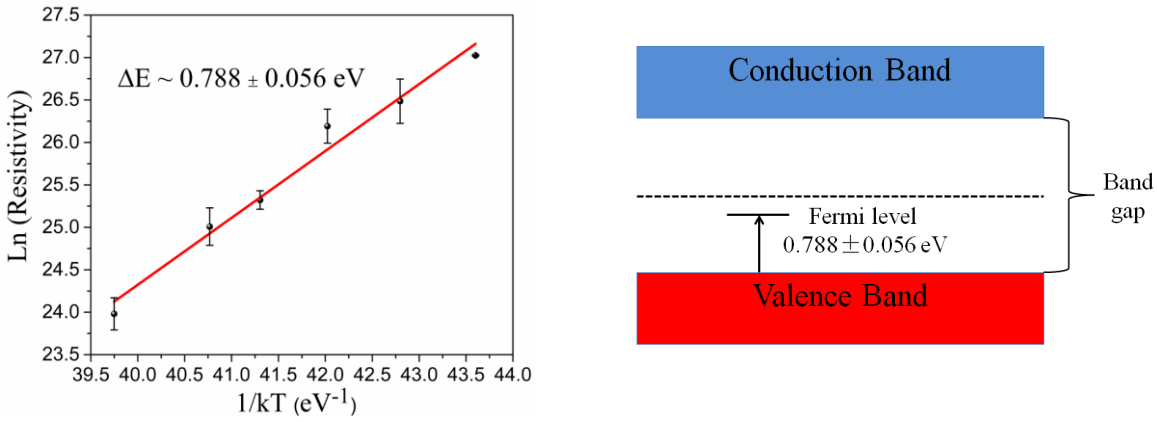

Figure 4.5 (a) and (b) Temperature dependence of the resistivity for Fermi level determination and the relative Fermi level position in the forbidden band.

4.5 Band Gap Energy of $Cs_2AgBiBr_6$

The band gap of $Cs_2AgBiBr_6$ could be estimated using,

$$I = I_0 e^{-\frac{E_g}{2kT}} \qquad (17)$$

where I is the current at temperature T (in Kelvin), I_0 is the reference current, k is the Boltzmann constant (8.617×10^{-5} eV/K) and E_g is the bandgap energy. Taking the logarithmic transformation, eqn. 17 becomes,

$$ln(I) = -\frac{E_g}{2k}\frac{1}{T} + ln(I_0) \qquad (18)$$

As displayed in Figure 4.6, the bandgap energy 2.07 eV of the double perovskite can be estimated using the slope of the fitting line. The small bandgap variation with temperature is neglected here since the measured temperature range is narrow (from 271 K to 305 K). In addition, the activation energy of charge carriers is assumed to be the same from 271 K to 305 K as the measurement were all conducted at low temperature range.

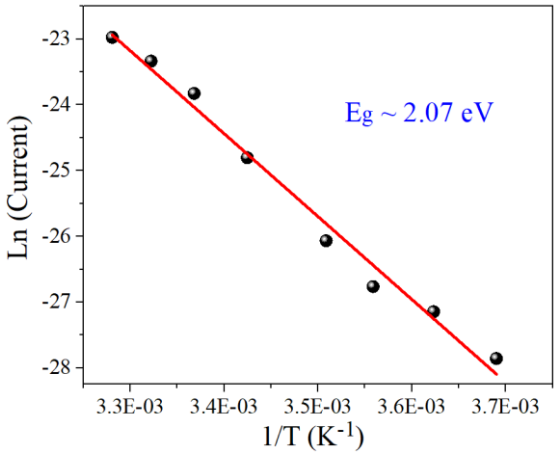

Figure 4.6 Estimation of the bandgap of $Cs_2AgBiBr_6$ using the variation of current with temperature. (Applied bias voltage: 1.0 V).

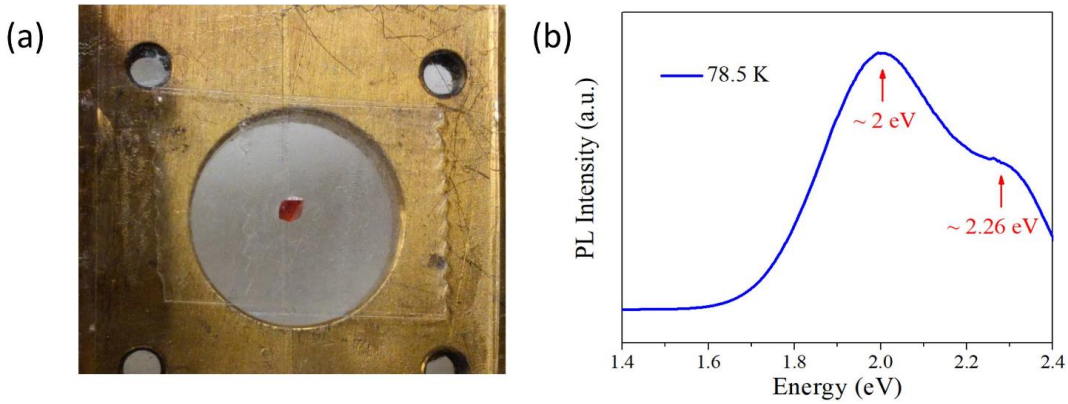

Figure 4.7 (a) $Cs_2AgBiBr_6$ single crystal was placed in position for PL excitation. (b) Low temperature photoluminescence (PL) spectrum of $Cs_2AgBiBr_6$ under 488 nm excitation.

Photoluminescence (PL) is a technique which uses the principle of photoexcitation. Light is emitted from semiconductor solids after the absorption of photons. PL measurement of $Cs_2AgBiBr_6$ was carried out using the fluorescence spectrometer FLS980 (Edinburgh Instruments). Figure 4.7 (a) shows the $Cs_2AgBiBr_6$ sample was placed in position for PL measurement. PL spectrum of the $Cs_2AgBiBr_6$ single crystal is shown in Figure 4.7 (b). Two PL peaks, located at approximately 2.00 eV and 2.26 eV respectively, were observed. We think the

emission of these two peaks are corresponding to previous reported band gap energies of $Cs_2AgBiBr_6$, 2.095 eV (indirect) and 2.254 eV (direct) [57].

In comparison with PL, cathodoluminescence (CL) is another method which uses higher-energy electrons (100 eV-30 keV for the JEOL JSM-7600F system used in this work) rather than light photons to excite the luminescent materials. The CL measurement was performed at analytical instrumentation facility (AIF) of NCSU. JEOL JSM-7600F Scanning Electron Microscope (SEM) coupled with a Horiba Synapse CCD lateral detector (200-1200 nm UV-Vis wavelengths) was used for receiving CL signals. Figure 4.8 showed the acquired CL spectrum using $Cs_2AgBiBr_6$ single crystals, measured at low-temperature T=83 K. Table 4.1 summarized the peak energies shown in Figure 4.8. The two peaks at 1.917 eV and 2.054 eV are ascribed to near band gap emissions with low intensities. They are likely from free exciton or bound exciton emissions, which can be induced when the created electrons and holes from band-gap radiation recombine and form free excitons, or the free excitons collide with donors or acceptors and bound to them to form (D^+, X) or (A^-, X) complexes [64]. The two near band gap energies given in the CL spectrum are lower than the band gap of hybrid perovskite $MAPbBr_3$ (2.21 eV) and $MAPbCl_3$ (2.97 eV) [62, 65]. Rest of the CL peaks likely come from the intrinsic material defects in the forbidden band. Some defects are CL emission activators and serve as recombination sites, which consequently produce photons in radioactive recombination processes. One example of such defects is the dislocations, which can induce localized electronic shallow levels due to the elastic strain fields and deep levels near middle of the gap because of the dangling bonds [66]. Another possible defect, vacancies (e.g., V_{Br}, V_{Ag}, V_{Bi}), can serve as donors (cation vacancy) or acceptors (anion vacancy) [49, 67]. Recombination may occur at donor or acceptor energy levels (donor-to-valence or band-to-acceptor) and therefore

luminescence are likely to occur. In other cases, a donor-acceptor (D-A) pair emission is possible when electrons bound to donors and holes bound to acceptors. Much work could be further conducted to date back to the origins of these CL emission peaks and thermal annealing is a method which could be applied experimentally to $Cs_2AgBiBr_6$. Basically, thermal annealing could alter the location of defects and causes defects (e.g., vacancies) being filled so that the corresponding CL peak induced by vacancy defects will be having lower intensity compared with the observed CL peak using pristine crystals.

Three band gap energies are known to exist in $Cs_2AgBiBr_6$, two of them are indirect (1.946 eV and 2.095 eV) and one is direct (2.254 eV) [57]. The near 2 eV band gap energy of $Cs_2AgBiBr_6$ is suitable for the use in X-ray and gamma photon detection, though it may be further reduced to 1.5 eV by cation engineering and anion alloying methods. Part of the halide bromide ions may be substituted with iodide to form $Cs_2AgBiBr_{6-x}I_x$ compositions. Such a new compound may have a lower band gap energy, and at the same time offer better charge transport properties.

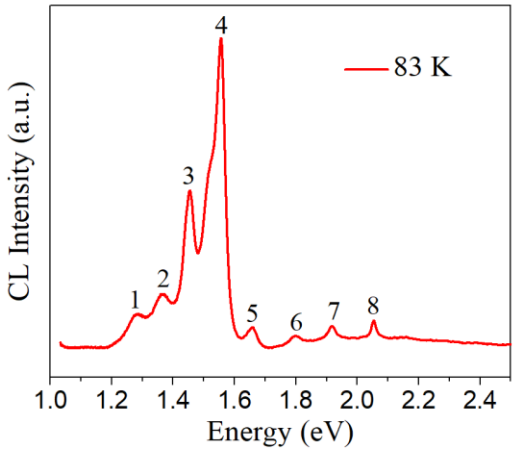

Figure 4.8 CL spectrum of $Cs_2AgBiBr_6$ single crystal at T=83 K.

Table 4.1 Peak energies in the CL spectrum

Peak	Energy (eV)
1	1.288
2	1.367
3	1.454
4	1.556
5	1.659
6	1.798
7	1.917
8	2.054

4.6 Space Charge Limited Current (SCLC) Characterization

Material defects in semiconductors could have a significant effect on the transport properties of charge carriers, which ultimately determine the device performance for detection applications. To evaluate the material defect density, we performed space charge limited current (SCLC) measurements on both Bi-normal and Bi-poor $Cs_2AgBiBr_6$ perovskite single crystals. As shown in Figure 4.9, SCLC measurement identified three transition regimes: ohmic, trap-filled limit (TFL), and child. In the ohmic regime, the current is linearly proportional to the applied voltage. Therefore, we can determine the crystal resistivity from the ohmic regime, which is estimated at 5.4×10^9 Ω·cm. Following the increased bias voltage, the transition regime starts to enter TFL and all defect traps in $Cs_2AgBiBr_6$ are filled. Onset voltage of the TFL regime can therefore be used to extract the density of trap states in $Cs_2AgBiBr_6$ according to the following formula [58],

$$n_t = \frac{2\varepsilon\varepsilon_0}{eL^2}V_{TFL} \qquad (19)$$

where n_t is the density of trap states, ε (=16.73) [59] is the static dielectric constant, ε_0 is the vacuum permittivity, L is the crystal thickness, and V_{TFL} is the onset voltage of TFL regime.

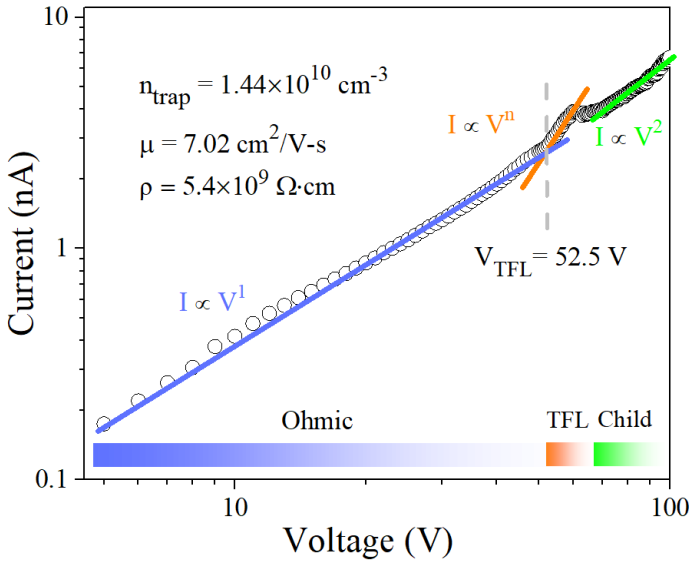

Figure 4.9 Space charge limited current (SCLC) measurement of Bi-normal $Cs_2AgBiBr_6$ single crystals, performed at 23 ℃ and Au was selected for electrodes deposition.

The density of trap states was calculated to be 1.44×10^{10} cm^{-3}, which is orders of magnitude lower than that in the polycrystalline perovskite thin film counterparts (~ 10^{16} cm^{-3}) [60]. The corresponding carrier mobility was determined to be 7.02 cm^2/V-s according to the Mott-Gurney law [61],

$$\mu = \frac{8J_D L^3}{9\varepsilon\varepsilon_0 V^2} \qquad (20)$$

where J_D is the current density at applied voltage V and μ is the carrier mobility.

The carrier concentration is then related with the mobility using equation (19) [65] and was estimated to be 1.65×10^{8} cm^{-3}. This value is slightly lower than that of hybrid single-crystalline perovskites ($MAPbI_3$ ~ 9×10^{9} cm^{-3}, $MAPbCl_3$ ~ 5.1×10^{9} cm^{-3}, $FAPbI_3$ ~ 2.8×10^{9} cm^{-3}) [32, 61, 62].

$$n_c = \frac{\sigma}{e\mu} \qquad (21)$$

where e is the electronic charge and σ is the conductivity.

4.7 Mu-Tau (μ-τ) Product

The mobility-lifetime (μ-τ) product is a key figure of merit in evaluating candidate materials' potential as radiation detection media. To estimate the μ-τ product of charge carriers in $Cs_2AgBiBr_6$ single crystals, a laser-induced photocurrent approach was used. Under the laser excitation at the wavelength of 450 nm, we recorded the produced photocurrent in the Au/$Cs_2AgBiBr_6$/Au device (Figure 4.10). Many's equation (or modified Hecht model) [30, 39] was employed to extract the μ-τ, as described by equation (22),

$$I = \frac{I_0 \mu \tau V}{L^2} \frac{1-exp(-\frac{L^2}{\mu \tau V})}{1+\frac{Ls}{V\mu}} \qquad (22)$$

where I is the measured photocurrent, I_0 is the saturated photocurrent, and s is the surface recombination velocity. Lower bound value of the μ-τ product of charge carriers in $Cs_2AgBiBr_6$ single crystals was estimated to be 2.48×10^{-3} cm^2/V and the surface recombination velocity is 2367.6 cm/s. The high μ-τ product of $Cs_2AgBiBr_6$ estimated here is comparable with some of the hybrid and all-inorganic perovskites ($MAPbI_3$ ~0.8×10^{-3} cm^2/V; $CsPbBr_3$ ~10^{-4} cm^2/V) [17, 73], though this value is lower than that of the highest quality CdZnTe single crystals (~ 10^{-2} cm^2/V) [74]. Calculated high surface recombination velocity indicates that ethanol is not very effective in removing undesirable surface trapping sites. To further the development of $Cs_2AgBiBr_6$, methanol and isopropanol could be used and tested for surface passivation.

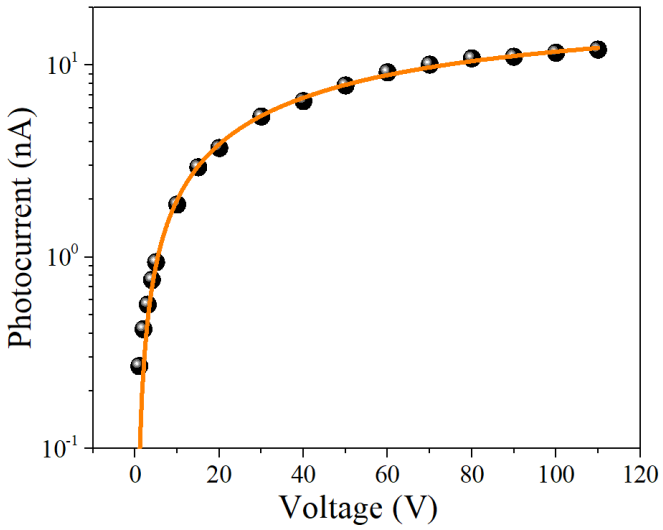

Figure 4.10 Recorded photocurrent using Bi-normal $Cs_2AgBiBr_6$ single crystals under laser excitation at the wavelength of 450 nm. Orange curve is the fitting line using Many's equation.

4.8 Response to LED Light

Along with the investigation of using $Cs_2AgBiBr_6$ single crystals for radiation detection, we studied its response to low-energy light photons. Figure 4.11 showed the strong luminescence of $Cs_2AgBiBr_6$ once illuminated by 400 nm wavelength visible light. Further, we tested the response of $Cs_2AgBiBr_6$ to light-emitting diode (LED) light. Figure 4.12 showed the 'on' and 'off' measurements using $Cs_2AgBiBr_6$ single crystals (exposed to 472 nm LED light). When the LED light is turned on, the flow of current in Au/$Cs_2AgBiBr_6$/Au device is significantly increased. This observation is expected. $Cs_2AgBiBr_6$ is currently very popular as new lead-free perovskites in solar cell research for converting sunlight photons into electrical current.

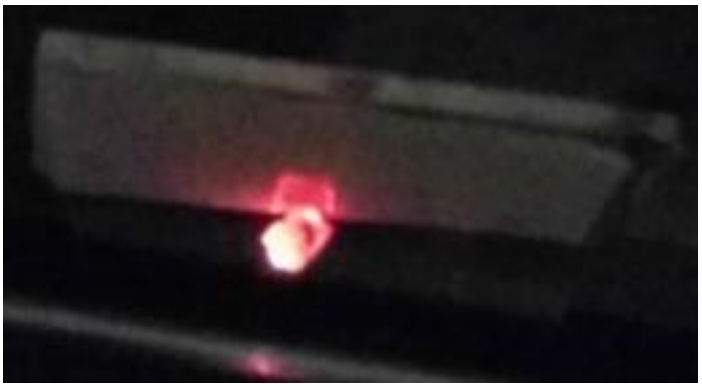

Figure 4.11 Strong luminescence of $Cs_2AgBiBr_6$ under illumination of visible light (400 nm wavelength).

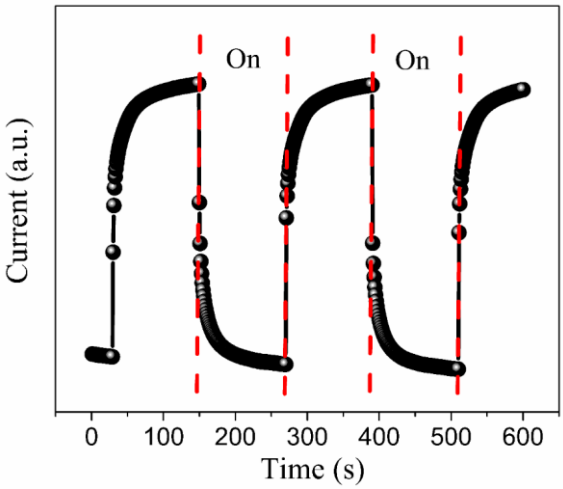

Figure 4.12 Response of $Cs_2AgBiBr_6$ single crystals to LED light (wavelength: 472 nm), bias voltage: −5 V.

4.9 Comparison Study between Bi-normal and Bi-poor $Cs_2AgBiBr_6$

4.9.1 XRD Measurements and Rocking Curve

Both XRD patterns for Bi-normal and Bi-poor $Cs_2AgBiBr_6$ single crystals (Figure 4.13 (a) and (b)) showed that pure $Cs_2AgBiBr_6$ phase was obtained with no presence of secondary phases. This indicates that both Bi-normal and Bi-poor solution growth processes should be able to produce high-quality $Cs_2AgBiBr_6$ single crystals. Figure 4.13 (c) shows the XRD omega scan

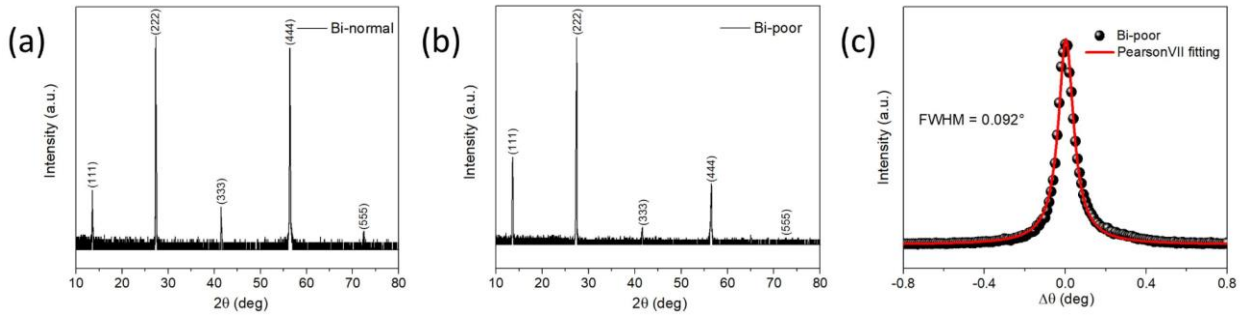

Figure 4.13 XRD patterns of as-grown (a) Bi-normal and (b) Bi-poor $Cs_2AgBiBr_6$ single crystals. (c) Rocking curve for Bragg peak (111) of Bi-poor $Cs_2AgBiBr_6$ single crystals, red line is the Pearson VII fitting curve.

for Bragg peak (111) using Bi-poor $Cs_2AgBiBr_6$ single crystals. Fitted by Pearson VII, the given full width at half maximum (FWHM) of the diffraction peak is 0.092°, which is better than single crystal $CsPbBr_3$ 0.16° [77] and $MAPbI_3$ 0.3718° [78]. The sharp peak indicates Bi-poor $Cs_2AgBiBr_6$ single crystal has excellent crystalline quality, which is suitable for radiation detection use.

4.9.2 Comparison between SCLC Curves

Figure 4.14 (a) and (b) showed the SCLC curves measured using Bi-poor and Bi-normal as-grown $Cs_2AgBiBr_6$ single crystals. Here, to make an accurate comparison as much as possible, carbon conductive glue was brushed onto both as-grown Bi-normal and Bi-poor single crystals. It should be noted that we previously selected Ag and Au as metal electrodes for Bi-normal $Cs_2AgBiBr_6$ single crystals. However, it has been reported that Ag could react with some perovskites and thus cause the degradation of device performance over time. Au has been almost the standard metal electrode for perovskite single crystals. Nevertheless, Au is not the best metal electrode in comparison with the Ag for $Cs_2AgBiBr_6$ [90].

Both Bi-normal and Bi-poor single crystals were rinsed with isopropanol and no further surface processing was performed. Resistivity determined for the Bi-poor single crystals is 1.56×10^{11} Ω·cm and carrier mobility (1.35 cm^2/V-s) is at the same magnitude compared with that was determined for Bi-normal single crystals (1.62×10^{11} Ω·cm and 3.59 cm^2/V-s). The density of trap states reached a desirable lower value of 2.65×10^{9} cm^{-3} for Bi-poor $Cs_2AgBiBr_6$ compared with 3.85×10^{10} cm^{-3} for Bi-normal $Cs_2AgBiBr_6$. This is consistent with the theoretical prediction for $Cs_2AgBiBr_6$ by Li et al. [49]. $Cs_2AgBiBr_6$ single crystals, grown from Bi-poor precursor solutions, have lower density of trap states.

4.9.3 Mu-Tau Product

The determined μ-τ product for Bi-poor $Cs_2AgBiBr_6$ single crystals is 1.47×10^{-3} cm^2/V (Figure 4.14 (c)). Especially, we observed that the μ-τ product has been raised from 5.19×10^{-4} cm^2/V for Bi-normal $Cs_2AgBiBr_6$ single crystals to 1.47×10^{-3} cm^2/V for crystals grown from Bi-poor solutions. Such an improvement indicated $Cs_2AgBiBr_6$ single crystals grown from Bi-poor solutions should have a preferable radiation detection performance compared with the Bi-normal ones. Moreover, the surface recombination velocity has been reduced to 85.69 cm/s for Bi-normal $Cs_2AgBiBr_6$ and 15.35 cm/s for Bi-poor $Cs_2AgBiBr_6$. It should be noted that we used isopropanol instead of the previously used ethanol to rinse the Bi-normal and Bi-poor $Cs_2AgBiBr_6$ single crystals. The results indicated that isopropanol is indeed more effective than ethanol for reducing the number of surface defect trapping sites.

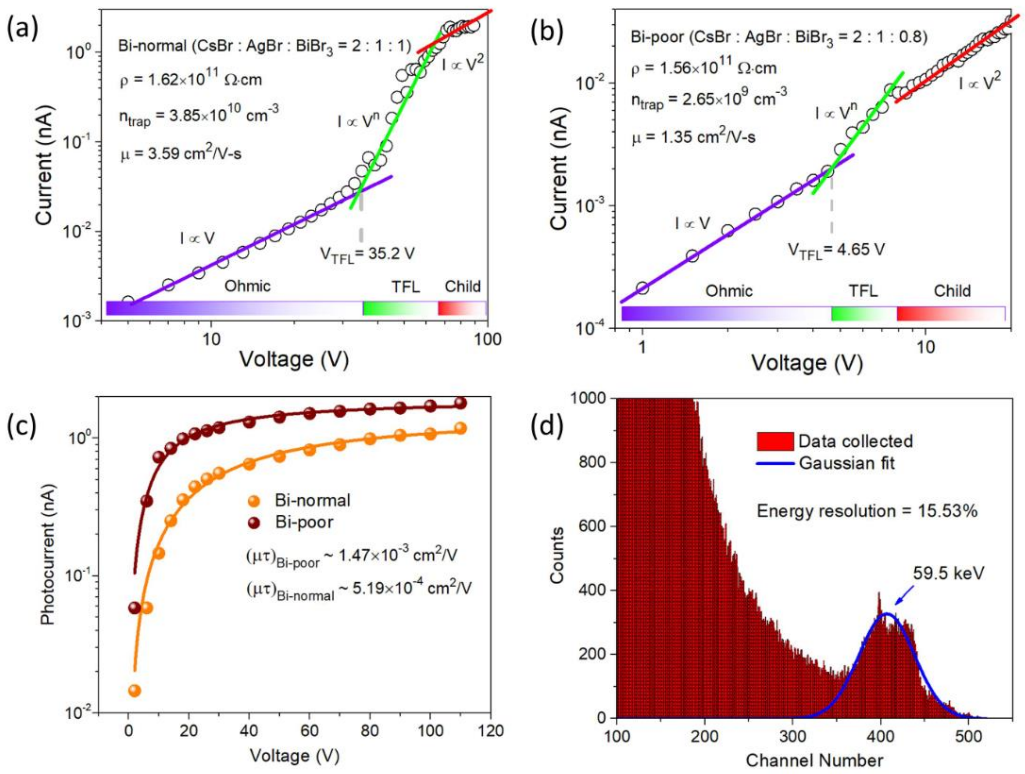

Figure 4.14 SCLC curves of (a) Bi-normal and (b) Bi-poor as-grown $Cs_2AgBiBr_6$ single crystals. The measurements were conducted at room temperature. (c) Photocurrent recorded for Bi-poor and Bi-normal $Cs_2AgBiBr_6$ single crystals using 450 nm laser excitation. The data is fitted by Many's equation. (d) Response of Bi-poor $Cs_2AgBiBr_6$-based detector to 0.1 μCi Am-241 radioactive source. The detector is biased at 200 V. Blue line is the Gaussian fitting curve.

4.9.4 Response to Gamma Radiation

Figure 4.14 (d) shows the energy spectrum recorded by a prototype gamma-ray detector based on Bi-poor $Cs_2AgBiBr_6$ single crystal, which has silver paste brushed on its two opposite pristine crystal surfaces. The 59.5 keV gamma-ray emitted as byproduct from 0.1 μCi Am-241 radioactive source was resolved with an energy resolution of 15.53% (taken as the FWHM over peak centroid). Figure 4.15 further compares the energy spectrum recorded by Bi-poor

$Cs_2AgBiBr_6$-based detector with and without the presence of Am-241 radioactive source. The 59.5 keV energy peak becomes absent without Am-241 radioactive source. Moreover, it is interesting that $Cs_2AgBiBr_6$ single crystals grown from Bi-normal conditions did not show any response to 59.5 keV gamma-ray. In our opinion, the defects in $Cs_2AgBiBr_6$, especially the deep level electron traps (which should have been suppressed in Bi-poor solution growth conditions), are playing an important role in terms of gamma-ray detection performance. In Bi-normal $Cs_2AgBiBr_6$ single crystals, charge carriers excited by 59.5 keV gamma photons could have been trapped by high level defect sites and thus could not effectively move across the crystal to form a signal. Our results indicate that $Cs_2AgBiBr_6$ single crystals grown from Bi-poor precursor solutions hold great potentials for the use as semiconductor gamma-ray detector materials and should be further explored.

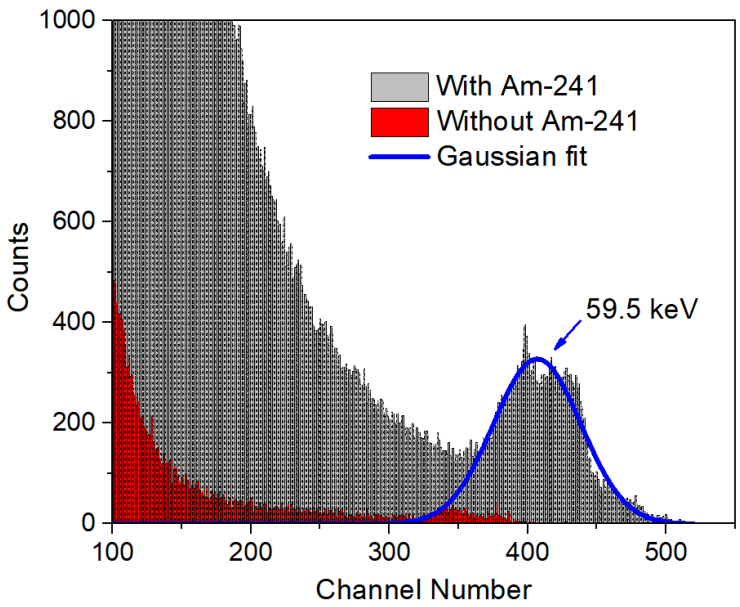

Figure 4.15 The energy spectrum recorded by Bi-poor $Cs_2AgBiBr_6$ detectors with and without Am-241 radioactive source. The data were collected with shaping time of 2 μs and bias at 200 V. The blue line is the Gaussian fitting curve for 59.5 keV gamma-ray energy peak.

Chapter 5: Response to X-ray

To evaluate the potential of using $Cs_2AgBiBr_6$ single crystals for X-ray detection, we fabricated a planar Au/$Cs_2AgBiBr_6$/Au detector using Bi-normal $Cs_2AgBiBr_6$ single crystals. Figure 5.1 presents the direct response of this device to X-ray radiation at 8 keV (produced from Cu X-ray tube). The corresponding bias voltage is -5 V, and a significant increase of photocurrent was observed when the X-ray beam was turned on. Such a change indicates $Cs_2AgBiBr_6$ single crystals are highly responsive to X-ray photons.

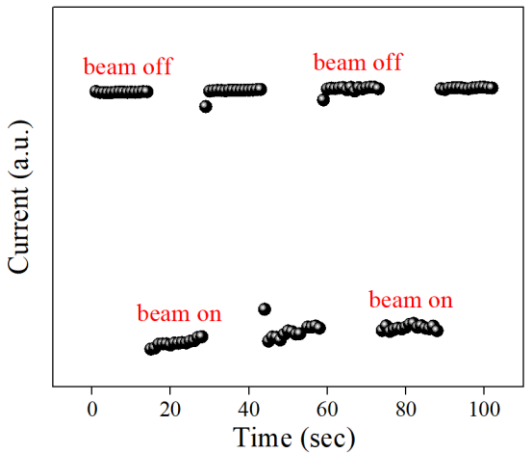

Figure 5.1 Response of Au/$Cs_2AgBiBr_6$/Au device to X-ray radiation. The tested $Cs_2AgBiBr_6$ single crystals were grown from Bi-normal conditions.

Figure 5.2 shows the device's response versus the variation of X-ray tube current, which represents a relative dose rate. As one can see, the Au/$Cs_2AgBiBr_6$/Au device showed a highly linear response to the variation of dose rate. Such linearity is especially important for radiation dosimetry applications, in which rapid determination of X-ray dose is required [63]. This finding demonstrated the potential of employing $Cs_2AgBiBr_6$ single crystals as solid state X-ray detectors in radiation dosimetry and medical imaging applications. Furthermore, Figure 5.3 shows the relationship between photocurrent and applied bias voltage, measured at the X-ray

tube current of 30 mA. From 5 V to 60 V, the linear increase of photocurrent was observed and the detector sensitivity (i.e., current density/dose rate) is improved by more than 15 times.

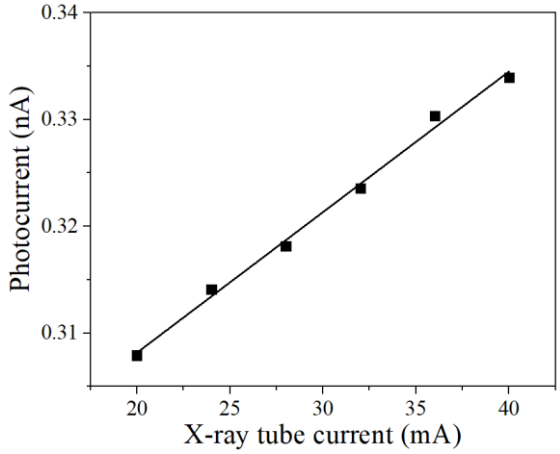

Figure 5.2 Recorded photocurrent of Au/$Cs_2AgBiBr_6$/Au device versus the variation of X-ray tube current, measured at bias voltage 5 V.

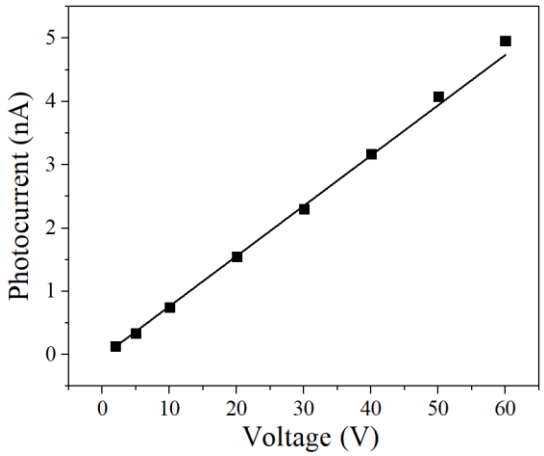

Figure 5.3 Variation of photocurrent versus applied bias voltage (The X-ray tube current is fixed at 30 mA).

Chapter 6: Issues for Further Development

6.1 Ionic Migration

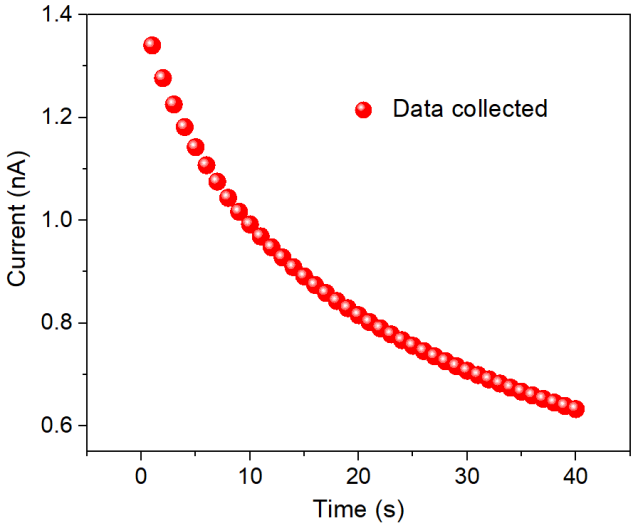

Figure 6.1 Recorded current vs. time to show the ionic migration issues in $Cs_2AgBiBr_6$ double perovskites, measurement was conducted completely under dark environment and with bias voltage of 5 V.

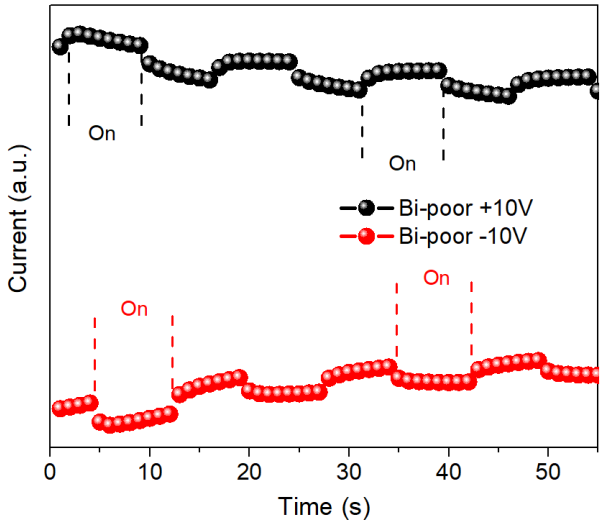

Figure 6.2 Response of Bi-poor $Cs_2AgBiBr_6$ single crystals to 472 nm LED light at bias voltage of +10 V and -10 V.

The halide ion migration issues have been known in many perovskites materials, such as $MAPbI_3$ and mixed-halide perovskite $MAPbBr_xI_{3-x}$ [24, 79-82]. Basically, the halide ions (I^-, Cl^-, Br^-) could migrate inside the device over time and thus cause the formation of electrical counter-field. The electrical counter-field induced by the migration of halide ions could retard the movement of charge carriers and thus affect the charge collection. Figure 6.1 shows the current recorded at bias of 5 V for $Cs_2AgBiBr_6$ single crystals. The measurement was conducted when the room light is turned on. As Figure 6.1 and Figure 6.2 exhibit, the ion migrations issues also exist in $Cs_2AgBiBr_6$ single crystals. To further the development of $Cs_2AgBiBr_6$ for gamma-ray detection, this issue should be addressed appropriately. One adoptable method is to select suitable metal electrodes to suppress the formation of counter electrical fields. For example, in thallium bromide (TlBr) detectors, the Br-ions can diffuse and react with nearly all types of metallic anodes and form non-conducting metal bromides, such as $AuBr_3$, $PtBr_2$ [91]. Several approaches have been proposed and one of them is using Tl as metal contacts to minimize the effects of polarization [92]. It showed that Tl can adhere strongly to TlBr. The TlBr detector fabricated using Tl as contacts did not show short-term (hundreds of hours) spectroscopic fluctuations during long-term lifetime tests [92]. It should be noted that this issue also exists in mercury iodide (HgI_2) compound semiconductors as the halide semiconductors are ionic in nature [93].

6.2 Phase Transition and Aging Effect

Some of the hybrid perovskites, such as $FAPbI_3$, can undergo facile phase transition from black phase to yellow phase (non-perovskite phase) within hours, shown in Figure 6.3. Such phase transition would be undesirable for radiation detection use as it usually leads to the crack

of materials. For all-inorganic $Cs_2AgBiBr_6$, since this material does not contain any organic components, it is expected that long-term stability should be possessed. Even though previous study shows that $Cs_2AgBiBr_6$ can undergo phase transition from cubic phase to tetragonal perovskite phase at 122 K [94], no phase transition at room temperature has been reported so far. Figure 6.4 shows the powder X-ray diffraction (PXRD) patterns for Bi-normal and Bi-poor $Cs_2AgBiBr_6$ samples that have been exposed under ambient air conditions for months. Figure 6.4 shows the RC measurements for Bi-normal and Bi-poor $Cs_2AgBiBr_6$ single crystals (samples have been stored under ambient air conditions for months). From Figure 6.3, no obvious signs of phase transition or decomposition of Bi-normal and Bi-poor $Cs_2AgBiBr_6$ have been observed even after 7 months and 11 months respectively. All PXRD peaks match well with the previously reported powder XRD pattern for as-produced $Cs_2AgBiBr_6$ [72]. The peaks are labelled correspondingly, according to the previous reported PXRD pattern [72].

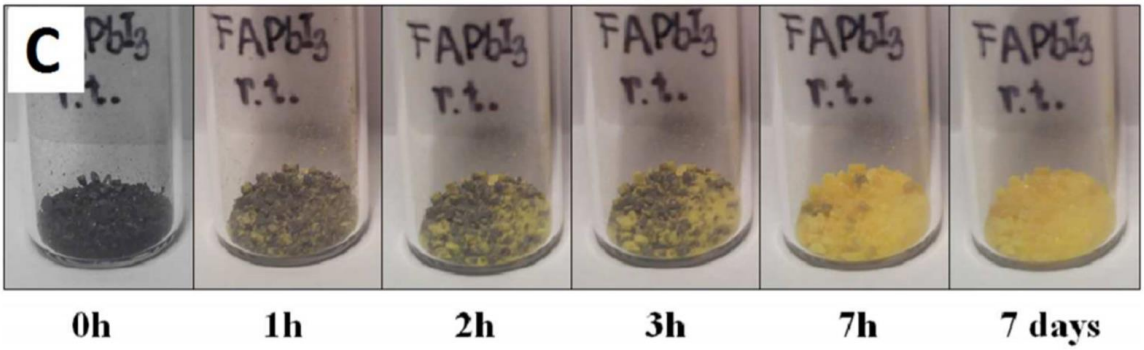

Figure 6.3 Phase transition of FAPbI3 from black phase to yellow phase within hours. (Reproduced with permission from [31], John Wiley and Sons, Copyright 2016.)

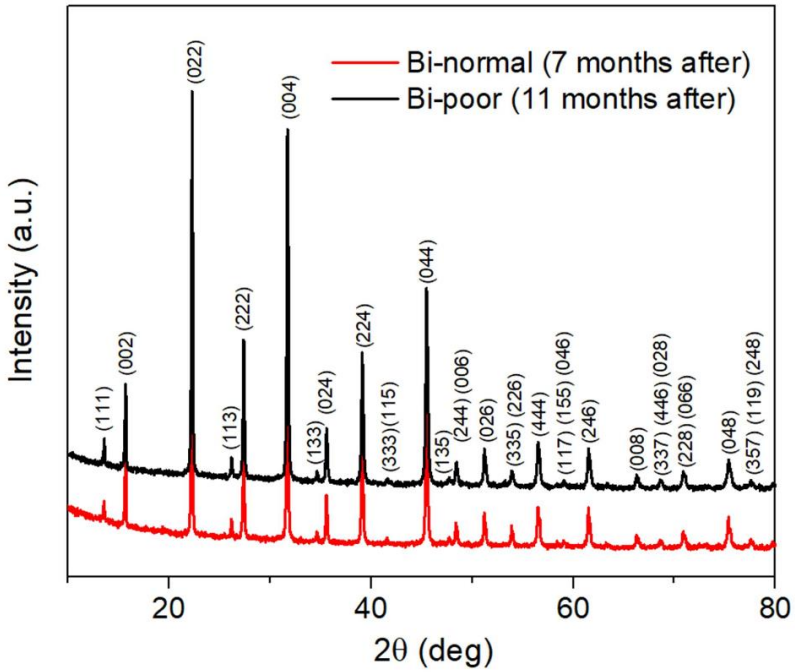

Figure 6.4 PXRD patterns for Bi-normal and Bi-poor $Cs_2AgBiBr_6$ samples that have been exposed under ambient air conditions for months.

According to Figure 6.5, FWHM for Bragg peak (222) of Bi-poor $Cs_2AgBiBr_6$ single crystal is 0.050°. Based on our SCLC and mu-tau results, Bi-poor $Cs_2AgBiBr_6$ single crystals should have better crystal qualities compared to Bi-normal ones. Therefore, RC measurements of Bi-poor $Cs_2AgBiBr_6$ samples should show a narrower peak with smaller FWHM. For the two samples that we have measured here, indeed the Bi-poor $Cs_2AgBiBr_6$ shows narrower peak with FWHM=0.050° compared with that for Bi-normal $Cs_2AgBiBr_6$ (FWHM=0.083°). Nevertheless, more measurements should be taken to confirm that $Cs_2AgBiBr_6$ single crystals grown from Bi-poor precursor solutions indeed have better crystalline quality compared to the ones grown from Bi-normal solutions. This is because the RC measurement could vary from crystal to crystal, though Bi-poor $Cs_2AgBiBr_6$ probably in general should have better crystalline quality compared to Bi-normal $Cs_2AgBiBr_6$.

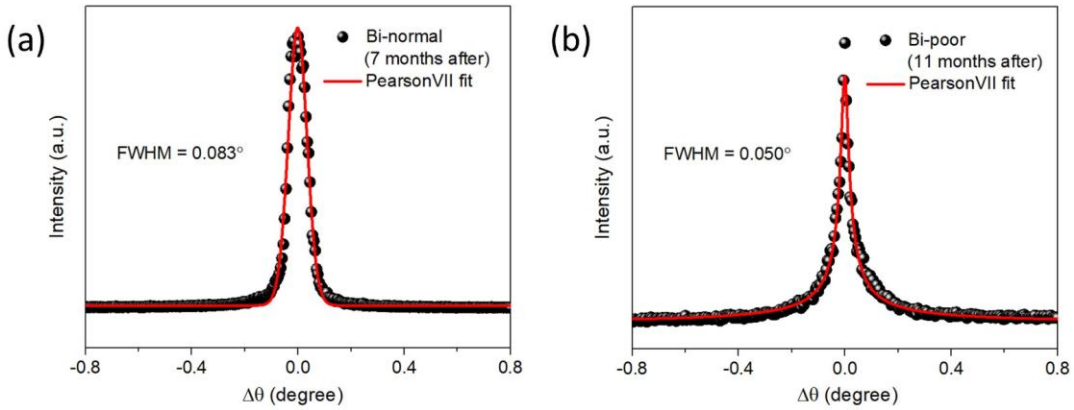

Figure 6.5 Rocking curve (RC) measurements for Bi-normal and Bi-poor $Cs_2AgBiBr_6$ single crystals, samples have been stored under ambient air conditions for months.

6.3 Poor electron transport

Though $Cs_2AgBiBr_6$ has showed excellent response to X-ray and 59.5 keV gamma-ray, there is a limiting factor that could hamper the further development of $Cs_2AgBiBr_6$. Figure 6.5 shows the laser-induced current in Bi-poor $Cs_2AgBiBr_6$ single crystals, recorded at room temperature by the lock-in amplifier with bias of -10 V, -20 V, 10 V, and 20 V. In this measurement, the 450 nm laser was focused and excited the single crystal at a fixed location from one electrode side only. Therefore, when positive or negative bias is applied, only the electron or hole will transport and contribute to the charge collection. Figure 6.6 clearly shows that the hole transport at positive bias is much better than electron transport at negative bias, which indicates that $(\mu\text{-}\tau)_h$ should be much larger $(\mu\text{-}\tau)_e$. This finding is consistent with the results reported by Longo et al. [85]. In $Cs_2AgBiBr_6$ thin films, the electron diffusion length is only ~30 nm, while the hole diffusion length is greater than 150 nm [85].

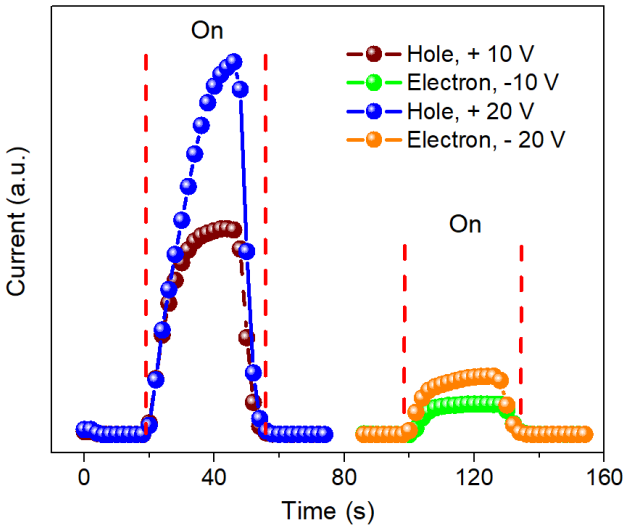

Figure 6.6 Recorded laser-induced current in Bi-poor $Cs_2AgBiBr_6$ single crystals at positive and negative bias of 10 V and 20 V, wavelength of the laser used is 450 nm.

Moreover, Bi-poor $Cs_2AgBiBr_6$ showed a relatively long rise-time (~ 18s, defined as the time interval between 10% and 90% of the reached maximum photocurrent) for hole-only transport. The rise-time for electron-only transport (~ 4s) is much shorter compared to that of hole-only transport. The long rise-time also could be observable for Bi-normal $Cs_2AgBiBr_6$ (Figure 4.12) when the single crystal was exposed to LED light. One hypothesis is that fall time is related with the charge carrier recombination after the light is turned off. The charge carrier gradually recombines and therefore the produced photocurrent is gradually reduced [95]. For the rise-time, it should be related the charge carrier mobility and the defect trapping sites. If large number of defect levels are presenting in the devices, it is expected that a certain amount of time will be required before maximum charge collection can be reached. For $Cs_2AgBiBr_6$, the relatively long rise-time for hole-only transport should originate from the possible low hole carrier mobility and the relatively large number of hole charge carrier trapping sites. Moreover, holes, as the majority charge carrier for p-type $Cs_2AgBiBr_6$, should be as expected governing the bulk crystal transport properties. This is because the rise-time, shown for Bi-normal $Cs_2AgBiBr_6$

(Figure 4.12) and Bi-poor $Cs_2AgBiBr_6$ (hole-only transport, Figure 6.6), remains relatively unchanged. It should be noted that for Figure 4.12 LED measurement, light was illuminated on the entire $Cs_2AgBiBr_6$-based detector and therefore both electrons and holes were equally contributing to the total charge collection.

6.4 Reducing the bandgap energy

It has been pointed out that $Cs_2AgBiBr_6$ has indirect band gap energy of 1.95 eV and direct band gap energy of 2.21 eV [47]. Though the bandgap value here is suitable for radiation detection use, more efforts could be made to reduce the bandgap energy to ~ 1.5 eV to improve the detector performance. Bandgap energy of 1.5 eV, which is also the value that CZT single crystal possesses, would be ideal for performing X-ray and gamma-ray detection. To shrink the bandgap energy of $Cs_2AgBiBr_6$, a possible way is to grow the single crystals using a different method, as demonstrated by Ji et al. [97]. Ji et al. used the slow evaporation method, rather than the slow temperature lowering (STL) technique, to grow $Cs_2AgBiBr_6$ single crystals at 60 ℃ and 150 ℃ respectively (Figure 6.7). It was observed that the bandgap energy of $Cs_2AgBiBr_6$ was reduced from 1.98 eV for DP-60 ($Cs_2AgBiBr_6$ grown at 60 ℃) to 1.72 eV for DP-150 ($Cs_2AgBiBr_6$ grown at 150 ℃). It also should be noted that though the crystal grown at 150 ℃ is black rather than red, the acquired solids remains to be $Cs_2AgBiBr_6$. The color change is likely due to the enhanced Ag-Bi disorder at 150 ℃ [97].

However, from another point of view, the semiconductor bandgap energy is an intrinsic property and thus should not change significantly just by adopting a different crystal growth method. More reliable bandgap engineering method for $Cs_2AgBiBr_6$ is to substitute part of the Cs elements with FA or MA cations, which may change the bandgap structure with a reduced bandgap energy.

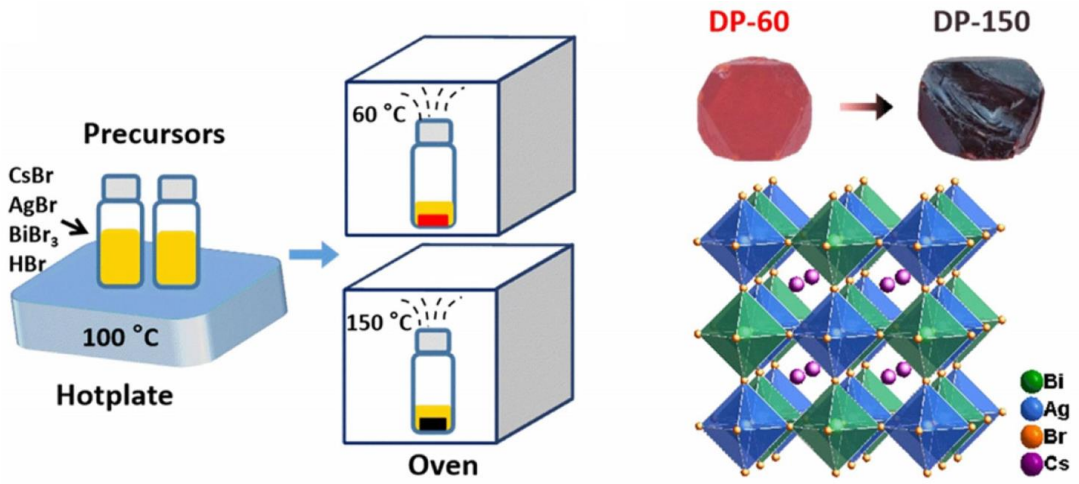

Figure 6.7 Illustration of the $Cs_2AgBiBr_6$ single crystal using slow evaporation method at 60 ℃ and 150 ℃ respectively. Double perovskite (DP) single crystals grown at 60 ℃ presents a red color, a black color is observed for DP single crystals grown at 150 ℃. (Reproduced with permission from [97], Wiley-VCH, Copyright 2020.)

6.5 Limited crystal size by conventional STL method

The $Cs_2AgBiBr_6$ single crystals grown by the conventional slow cooling method can only produce single crystals with size about 3 mm large or even smaller [72, 104], which is likely due to the formation of multiple nucleation sites during the crystal growth processes. In our lab, we were able to produce single crystals with size up to 10 mm in length. Nevertheless, the formation of multiple nucleation sites was not able to be well controlled. Recently, using MABr as the flux in HBr-H_3PO_2 mixed solution [90] and adding toluene additive [105] have been reported for growing $Cs_2AgBiBr_6$ that can yield single crystals with size above 10 mm in length. For the further research on $Cs_2AgBiBr_6$, a larger crystal with size around at least 5 mm thick would be desired for the use as gamma-ray detector fabrication.

Chapter 7: Summary and Conclusions

Table 7.1 summarized the evaluated properties of Bi-normal $Cs_2AgBiBr_6$ single crystals for radiation detection. In comparison, we compared this work with previous published research in using $Cs_2AgBiBr_6$ single crystals for X-ray detection. As shown in Table 7.1, $Cs_2AgBiBr_6$ single crystals have a very high desirable resistivity of 10^9-10^{11} Ω·cm. The density of trap states in Bi-normal single crystals is in the order of 10^9-10^{10} cm^{-3}. Low dark carrier concentration is expected as this material has very high resistivity at room temperature. Regarding the carrier mobility, the reported value is very low, no more than 10 cm^2/V-s. However, the estimated μ-τ product in the order of 10^{-4} to 10^{-3} cm^2/V is very encouraging due to the very long charge carrier lifetime in $Cs_2AgBiBr_6$. Further, the estimated high surface recombination velocity indicated that surface trapping sites should be further passivated using a more effective treatment method or solvent. We used isopropanol organic solvent to treat the as-grown Bi-normal and Bi-poor $Cs_2AgBiBr_6$ single crystal surfaces. It showed that the surface recombination velocity has been significantly reduced to 85.69 cm/s and 15.35 cm/s respectively (Table 7.2).

Main research focus of this work is to develop $Cs_2AgBiBr_6$ for high energy gamma photon and alpha particle detection. Up to date, to the best of our knowledge, no reports have been made in using $Cs_2AgBiBr_6$ to successfully fulfill this purpose. We tested Schottky-type Bi-normal $Cs_2AgBiBr_6$ detector (Au/$Cs_2AgBiBr_6$/Ga, 50 nm Au (work function ~ 5.1 eV), 50 nm Ga (work function ~ 4.3 eV)) for detecting Co-57 122 keV gamma ray and Am-241 5.5 MeV alpha particle. The Au/$Cs_2AgBiBr_6$/Ga detector showed no response. The same situation happened to Ohmic-type Au/$Cs_2AgBiBr_6$/Au detector using Bi-normal single crystals.

The Bi-poor single crystals in theory have a lower density of trap states compared with Bi-normal single crystals at room temperature and therefore charge carriers should be more

Table 7.1 Summary of the evaluated properties of Bi-normal $Cs_2AgBiBr_6$ single crystals

Property	*Bi-normal $Cs_2AgBiBr_6$	Bi-normal $Cs_2AgBiBr_6$	Bi-normal $Cs_2AgBiBr_6$
Atomic Number	Cs: 55, Ag: 47, Bi: 83, Br: 35	53.1	-
Density (g/cm^3)	4.65	-	-
**Resistivity ($\Omega \cdot cm$)	10^9-10^{10}	10^9-10^{11}	10^9-10^{10}
Bandgap Energy (eV)	2.00 (Indirect), 2.26 (Direct)	-	-
Density of Trap States (cm^{-3})	1.44×10^{10}	4.54×10^9	-
Dark Carrier Concentration (cm^{-3})	1.65×10^8	-	-
Mobility ($cm^2/V\text{-}s$)	7.02	3.17	1.70
μ-τ Product (cm^2/V)	2.48×10^{-3}	3.75×10^{-3}	1.36×10^{-4}
Surface Recombination Velocity (cm/s)	2367.6	1496	-
Response to X-ray	Yes, 8 keV (Cu X-ray tube)	Yes, 30 keV (Tungsten X-ray tube)	Yes, 30 keV (Tungsten X-ray tube)
Response to Alpha Particle	No response	N/A	N/A
Response to γ-ray	No response	N/A	N/A

Table 7.1 (continued)

Reference	This work	[72]	[75]

*The reported properties are based on Au/$Cs_2AgBiBr_6$/Au device

**Measured resistivity is at room temperature

easily transported towards cathodes and anodes under external applied bias without being trapped. Therefore, Bi-poor $Cs_2AgBiBr_6$ single crystals probably can give some response to charged alpha particles and high energy gamma-rays compared with Bi-normal $Cs_2AgBiBr_6$ single crystals. Indeed, it is interesting that the Ohmic-type Ag/$Cs_2AgBiBr_6$/Ag detector using Bi-poor single crystals for the first time showed response to 59.5 keV gamma-rays. In our opinion, the defects in $Cs_2AgBiBr_6$, especially the deep level electron traps (which should have been suppressed in Bi-poor solution growth conditions), are playing an important role in terms of gamma-ray detection performance. In Bi-normal $Cs_2AgBiBr_6$ single crystals, charge carriers excited by 59.5 keV gamma photons could have been trapped by high level defect sites and thus could not effectively move across the crystal to form a signal. Table 7.2 summarized the properties that were determined for Bi-normal and Bi-poor $Cs_2AgBiBr_6$ single crystals. Our results indicate that high-quality $Cs_2AgBiBr_6$ single crystals may be grown from Bi-poor precursor solutions. Bi-poor $Cs_2AgBiBr_6$ single crystals, for the first time showed response to gamma photons, hold great potentials for the use as semiconductor gamma-ray detector materials and should be further explored.

Table 7.2 Comparison between the Bi-normal and Bi-poor $Cs_2AgBiBr_6$ single crystals

Property	*Bi-normal $Cs_2AgBiBr_6$	*Bi-poor $Cs_2AgBiBr_6$
**Resistivity (Ω·cm)	1.62×10^{11}	1.56×10^{11}
Density of Trap States (cm^{-3})	3.85×10^{10}	2.65×10^{9}

Table 7.2 (continued)

Mobility (cm^2/V-s)	3.59	1.35
μ-τ Product (cm^2/V)	5.19×10^{-4}	1.47×10^{-3}
Surface Recombination Velocity (cm/s)	85.69	15.35
Response to Alpha Particle	-	-
Response to γ-ray	No	Yes (59.5 γ-ray)

*The reported properties are based on Ohmic-type $Cs_2AgBiBr_6$ detectors

**Measured resistivity is at room temperature

In summary, we successfully detected soft 8 keV X-ray and 59.5 keV gamma-ray using $Cs_2AgBiBr_6$ single crystals. $Cs_2AgBiBr_6$ single crystals, as lead-free green double perovskite, have great potentials (high μ-τ product (~10^{-3} cm^2/V), large resistivity (10^9-10^{11} Ω·cm), suitable band gap energy (~ 2 eV)) and with low materials cost (~ \$6/cm^3) for the use as next generation semiconductor-based X-ray and gamma-ray detectors. Future work should be to test the response of Bi-poor $Cs_2AgBiBr_6$ single crystals to higher energy gamma-rays (e.g., 662 keV gamma-ray emitted from the radioactive decay of Cs-137, and 1.33 MeV gamma-ray from Co-57) and also alpha particles.

REFERENCES

(1) Zhang, Z., Yang, G. Recent advancements in using perovskite single crystals for gamma-ray detection. *J Mater Sci: Mater Electron* (2020). https://doi.org/10.1007/s10854-020-03519-z

(2) Roy, U. N.; Camarda, G. S.; Cui, Y.; Gul, R.; Yang, G.; Zazvorka, J.; Dedic, V.; Franc, J.; James, R. B. Evaluation of CdZnTeSe as a High-Quality Gamma-Ray Spectroscopic Material with Better Compositional Homogeneity and Reduced Defects. Sci. Rep. 2019, 9 (1).

(3) del Sordo, S.; Abbene, L.; Caroli, E.; Mancini, A. M.; Zappettini, A.; Ubertini, P. Progress in the Development of CdTe and CdZnTe Semiconductor Radiation Detectors for Astrophysical and Medical Applications. Sensors 2009, 9 (5), 3491–3526.

(4) Schlesinger, T. E.; Toney, J. E.; Yoon, H.; Lee, E. Y.; Brunett, B. A.; Franks, L.; James, R. B. Cadmium Zinc Telluride and Its Use as a Nuclear Radiation Detector Material. Mater. Sci. Eng. R Reports 2001, 32 (4–5), 103–189.

(5) BAILY, N. A.; MAYER, J. W. A P-N Junction Semiconductor Radiation Detector for Use with Beta- and Gamma-Ray-Emitting Isotopes. Radiology 1961, 76, 116.

(6) Johnson, L. C.; Campbell, D. L.; Hull, E. L.; Peterson, T. E. Characterization of a High-Purity Germanium Detector for Small-Animal SPECT. Phys. Med. Biol. 2011, 56 (18), 5877–5888.

(7) Abbaspour, S.; Mahmoudian, B.; Islamian, J. Cadmium Telluride Semiconductor Detector for Improved Spatial and Energy Resolution Radioisotopic Imaging. World J. Nucl. Med. 2017, 16 (2), 101.

(8) Zaletin, V. M.; Varvaritsa, V. P. Wide-Bandgap Compound Semiconductors for X- or Gamma-Ray Detectors. Russ. Microelectron. 2011, 40 (8), 443–452.

(9) Owens, A. Compound Semiconductor Radiation Detectors; CRC Press, 2012.

(10) Eisen, Y.; Shor, A.; Mardor, I. CdTe and CdZnTe Gamma Ray Detectors for Medical and Industrial Imaging Systems. Nucl. Instruments Methods Phys. Res. Sect. A Accel. Spectrometers, Detect. Assoc. Equip. 1999, 428 (1), 158–170.

(11) Varnell, L. S.; Mahoney, W. A.; Hull, E. L.; Butler, J. F.; Wong, A. S. Radiation Effects in CdZnTe Gamma-Ray Detectors Produced by 199-MeV Protons. In Proceedings of SPIE - The International Society for Optical Engineering; 1996; Vol. 2806, pp 424–431.

(12) Li, Q.; Beilicke, M.; Lee, K.; Garson, A.; Guo, Q.; Martin, J.; Yin, Y.; Dowkontt, P.; De Geronimo, G.; Jung, I.; et al. Study of Thick CZT Detectors for X-Ray and Gamma-Ray Astronomy. Astropart. Phys. 2011, 34 (10), 769–777.

(13) Bolotnikov, A. E.; Ackley, K.; Camarda, G. S.; Cui, Y.; Eger, J. F.; De Geronimo, G.; Finfrock, C.; Fried, J.; Hossain, A.; Lee, W.; et al. High-Efficiency CdZnTe Gamma-Ray Detectors. In IEEE Transactions on Nuclear Science; Institute of Electrical and Electronics Engineers Inc., 2015; Vol. 62, pp 3193–3198.

(14) Roy, U. N.; Camarda, G. S.; Cui, Y.; Gul, R.; Hossain, A.; Yang, G.; Zazvorka, J.; Dedic, V.; Franc, J.; James, R. B. Role of Selenium Addition to CdZnTe Matrix for Room-Temperature Radiation Detector Applications. Sci. Rep. 2019, 9 (1).

(15) Chen, Z.; Turedi, B.; Alsalloum, A. Y.; Yang, C.; Zheng, X.; Gereige, I.; Alsaggaf, A.; Mohammed, O. F.; Bakr, O. M. Single-Crystal MAPbI3 Perovskite Solar Cells Exceeding 21% Power Conversion Efficiency. ACS Energy Lett. 2019, 4 (6), 1258–1259.

(16) Kim, H.; Byun, H. R.; Jeong, M. S. Synthesis and Characterization of Multiple-Cation Rb(MAFA)PbI3 Perovskite Single Crystals. Sci. Rep. 2019, 9 (1).

(17) He, Y.; Ke, W.; Alexander, G. C. B.; McCall, K. M.; Chica, D. G.; Liu, Z.; Hadar, I.; Stoumpos, C. C.; Wessels, B. W.; Kanatzidis, M. G. Resolving the Energy of γ-Ray Photons with MAPbI3 Single Crystals. ACS Photonics 2018, 5 (10), 4132–4138.

(18) Mirershadi, S.; Javad, A.; Ahmadi-Kandjani, S. Efficient Single-Layer Light-Emitting Diodes Based on Organic–Inorganic Lead Halide Perovskite and Tuning Luminescence Properties. J. Theor. Appl. Phys. 2019, 13 (2), 133–140.

(19) Tan, Z. K.; Moghaddam, R. S.; Lai, M. L.; Docampo, P.; Higler, R.; Deschler, F.; Price, M.; Sadhanala, A.; Pazos, L. M.; Credgington, D.; et al. Bright Light-Emitting Diodes Based on Organometal Halide Perovskite. Nat. Nanotechnol. 2014, 9 (9), 687–692.

(20) Li, L.; Liu, X.; Zhang, H.; Zhang, B.; Jie, W.; Sellin, P. J.; Hu, C.; Zeng, G.; Xu, Y. Enhanced X-Ray Sensitivity of MAPbBr3 Detector by Tailoring the Interface-States Density. ACS Appl. Mater. Interfaces 2019, 11 (7), 7522–7528.

(21) He, Y.; Matei, L.; Jung, H. J.; McCall, K. M.; Chen, M.; Stoumpos, C. C.; Liu, Z.; Peters, J. A.; Chung, D. Y.; Wessels, B. W.; et al. High Spectral Resolution of Gamma-Rays at Room Temperature by Perovskite CsPbBr3 Single Crystals. Nat. Commun. 2018, 9 (1).

(22) Kumari, N.; Patel, S. R.; Gohel, J. V. Superior Efficiency Achievement for FAPbI3 - Perovskite Thin Film Solar Cell by Optimization with Response Surface Methodology Technique and Partial Replacement of Pb by Sn. Optik (Stuttg). 2019, 176, 262–277.

(23) Li, Y.; Shao, W.; Ouyang, X.; Ouyang, X.; Zhu, Z.; Zhang, H.; Liu, B.; Xu, Q. Scintillation Properties of Perovskite Single Crystals. J. Phys. Chem. C 2019, 123 (28), 17449–17453.

(24) Yakunin, S.; Dirin, D. N.; Shynkarenko, Y.; Morad, V.; Cherniukh, I.; Nazarenko, O.; Kreil, D.; Nauser, T.; Kovalenko, M. V. Detection of Gamma Photons Using Solution-Grown Single Crystals of Hybrid Lead Halide Perovskites. Nat. Photonics 2016, 10 (9), 585–589.

(25) Liu, Z.; Peters, J. A.; Stoumpos, C. C.; Sebastian, M.; Wessels, B. W.; Im, J.; Freeman, A. J.; Kanatzidis, M. G. Heavy Metal Ternary Halides for Room-Temperature x-Ray and Gamma-Ray Detection. In Hard X-Ray, Gamma-Ray, and Neutron Detector Physics XV; Fiederle, M., Burger, A., Franks, L., James, R. B., Eds.; 2013; Vol. 8852, p 88520A.

(26) Steirer, K. X.; Schulz, P.; Teeter, G.; Stevanovic, V.; Yang, M.; Zhu, K.; Berry, J. J. Defect Tolerance in Methylammonium Lead Triiodide Perovskite. ACS Energy Lett. 2016, 1 (2), 360–366.

(27) Wang, L.; Yuan, G. D.; Duan, R. F.; Huang, F.; Wei, T. B.; Liu, Z. Q.; Wang, J. X.; Li, J. M. Tunable Bandgap in Hybrid Perovskite CH3NH3Pb(Br3-yXy) Single Crystals and Photodetector Applications. AIP Adv. 2016, 6 (4).

(28) Li, W. G.; Rao, H. S.; Chen, B. X.; Wang, X. D.; Kuang, D. Bin. A Formamidinium-Methylammonium Lead Iodide Perovskite Single Crystal Exhibiting Exceptional Optoelectronic Properties and Long-Term Stability. J. Mater. Chem. A 2017, 5 (36), 19431–19438.

(29) Goldschmidt, V. M. Die Gesetze Der Krystallochemie. Naturwissenschaften 1926, 14, 477–485.

(30) Stoumpos, C. C.; Malliakas, C. D.; Peters, J. A.; Liu, Z.; Sebastian, M.; Im, J.; Chasapis, T. C.; Wibowo, A. C.; Chung, D. Y.; Freeman, A. J.; et al. Crystal Growth of the Perovskite

Semiconductor CsPbBr3: A New Material for High-Energy Radiation Detection. Cryst. Growth Des. 2013, 13 (7), 2722–2727.

(31) Han, Q.; Bae, S. H.; Sun, P.; Hsieh, Y. T.; Yang, Y.; Rim, Y. S.; Zhao, H.; Chen, Q.; Shi, W.; Li, G.; et al. Single Crystal Formamidinium Lead Iodide (FAPbI3): Insight into the Structural, Optical, and Electrical Properties. Adv. Mater. 2016, 28 (11), 2253–2258.

(32) Liu, Y.; Sun, J.; Yang, Z.; Yang, D.; Ren, X.; Xu, H.; Yang, Z.; Liu, S. F. 20-mm-Large Single-Crystalline Formamidinium-Perovskite Wafer for Mass Production of Integrated Photodetectors. Adv. Opt. Mater. 2016, 4 (11), 1829–1837.

(33) Zhang, H.; Liu, X.; Dong, J.; Yu, H.; Zhou, C.; Zhang, B.; Xu, Y.; Jie, W. Centimeter-Sized Inorganic Lead Halide Perovskite CsPbBr3 Crystals Grown by an Improved Solution Method. Cryst. Growth Des. 2017, 17 (12), 6426–6431.

(34) Saidaminov, M. I.; Haque, M. A.; Almutlaq, J.; Sarmah, S.; Miao, X. H.; Begum, R.; Zhumekenov, A. A.; Dursun, I.; Cho, N.; Murali, B.; et al. Inorganic Lead Halide Perovskite Single Crystals: Phase-Selective Low-Temperature Growth, Carrier Transport Properties, and Self-Powered Photodetection. Adv. Opt. Mater. 2017, 5 (2), 1600704.

(35) Mirzaei, A.; Huh, J. S.; Kim, S. S.; Kim, H. W. Room Temperature Hard Radiation Detectors Based on Solid State Compound Semiconductors: An Overview. Electron. Mater. Lett. 2018, 14 (3), 261–287.

(36) Devanathan, R.; Corrales, L. R.; Gao, F.; Weber, W. J. Signal Variance in Gamma-Ray Detectors-A Review. Nucl. Instruments Methods Phys. Res. Sect. A Accel. Spectrometers, Detect. Assoc. Equip. 2006, 565 (2), 637–649.

(37) Kim, K. O.; Kwon, T. J.; Kim, J. K.; Ha, J. H. A New Approach for Evaluating the Mobility-Lifetime Products of Electron-Hole Pairs in Semiconductor Detectors. J. Korean Phys. Soc. 2011, 59 (1), 20–26.

(38) Street, R. A.; Ready, S. E.; Van Schuylenbergh, K.; Ho, J.; Boyce, J. B.; Nylen, P.; Shah, K.; Melekhov, L.; Hermon, H. Comparison of PbI2 and HgI2 for Direct Detection Active Matrix X-Ray Image Sensors. J. Appl. Phys. 2002, 91 (5), 3345–3355.

(39) Many, A. High-Field Effects in Photoconducting Cadmium Sulphide. J. Phys. Chem. Solids 1965, 26 (3), 575–578.

(40) Saidaminov, M. I.; Abdelhady, A. L.; Murali, B.; Alarousu, E.; Burlakov, V. M.; Peng, W.; Dursun, I.; Wang, L.; He, Y.; MacUlan, G.; et al. High-Quality Bulk Hybrid Perovskite Single Crystals within Minutes by Inverse Temperature Crystallization. Nat. Commun. 2015, 6, 23955.

(41) Li, S.; Zhang, C.; Song, J. J.; Xie, X.; Meng, J. Q.; Xu, S. Metal Halide Perovskite Single Crystals: From Growth Process to Application. Crystals 2018, 8 (5), 220.

(42) Dang, Y.; Liu, Y.; Sun, Y.; Yuan, D.; Liu, X.; Lu, W.; Liu, G.; Xia, H.; Tao, X. Bulk Crystal Growth of Hybrid Perovskite Material CH3NH3PbI3. CrystEngComm 2015, 17 (3), 665–670.

(43) Xin, C.; Veber, P.; Guennou, M.; Toulouse, C.; Valle, N.; Ciomaga Hatnean, M.; Balakrishnan, G.; Haumont, R.; Saint Martin, R.; Velazquez, M.; et al. Single Crystal Growth of BaZrO3 from the Melt at 2700 °C Using Optical Floating Zone Technique and Growth Prospects from BaB2O4 Flux at 1350 °C. CrystEngComm 2019, 21 (3), 502–512.

(44) Guguschev, C.; Klimm, D.; Brützam, M.; Gesing, T. M.; Gogolin, M.; Paik, H.; Dittmar, A.; Fratello, V. J.; Schlom, D. G. Single Crystal Growth and Characterization of Ba2ScNbO6 – A Novel Substrate for BaSnO3 Films. J. Cryst. Growth 2019, 528.

(45) Owens, A. Compound Semiconductor Radiation Detectors; CRC Press, 2012.

(46) Sudharsanan, R.; Parnham, K. B.; Karam, N. H. Cadmium Zinc Telluride Detects Gamma Rays, Laser Focus World, 1996.

(47) Slavney, A. H.; Hu, T.; Lindenberg, A. M.; Karunadasa, H. I. A Bismuth-Halide Double Perovskite with Long Carrier Recombination Lifetime for Photovoltaic Applications. J. Am. Chem. Soc. 2016, 138 (7), 2138–2141.

(48) Zhang, Z.; Yang, G.; Zhou, C.; Chung, C. C.; Hany, I. Optical and Electrical Properties of All-Inorganic Cs2AgBiBr6 Double Perovskite Single Crystals. RSC Adv. 2019, 9 (41), 23459–23464.

(49) Li, T.; Zhao, X.; Yang, D.; Du, M. H.; Zhang, L. Intrinsic Defect Properties in Halide Double Perovskites for Optoelectronic Applications. Phys. Rev. Appl. 2018, 10 (4), 41001.

(50) Zhang, Z.; Chung, C.-C.; Huang, Z.; Vetter, E.; Seyitliyev, D.; Sun, D.; Gundogdu, K.; Castellano, F. N.; Danilov, E. O.; Yang, G. Towards Radiation Detection Using Cs2AgBiBr6 Double Perovskite Single Crystals. Mater. Lett. 2020, 269, 127667.

(51) Zhou, J.; Fang, H. H.; Wang, H.; Meng, R.; Zhou, H.; Loi, M. A.; Zhang, Y. Understanding the Passivation Mechanisms and Opto-Electronic Spectral Response in Methylammonium Lead Halide Perovskite Single Crystals. ACS Appl. Mater. Interfaces 2018, 10 (41), 35580–35588.

(52) Wei, H.; Fang, Y.; Mulligan, P.; Chuirazzi, W.; Fang, H. H.; Wang, C.; Ecker, B. R.; Gao, Y.; Loi, M. A.; Cao, L.; et al. Sensitive X-Ray Detectors Made of Methylammonium Lead Tribromide Perovskite Single Crystals. Nat. Photonics 2016, 10 (5), 333–339.

(53) Li, J.; Dong, Q.; Li, N.; Wang, L. Direct Evidence of Ion Diffusion for the Silver-Electrode-Induced Thermal Degradation of Inverted Perovskite Solar Cells. Adv. Energy Mater. 2017, 7 (14), 1602922.

(54) Guerrero, A.; You, J.; Aranda, C.; Kang, Y. S.; Garcia-Belmonte, G.; Zhou, H.; Bisquert, J.; Yang, Y. Interfacial Degradation of Planar Lead Halide Perovskite Solar Cells. ACS Nano 2016, 10 (1), 218–224.

(55) Xu, Y.; Jie, W.; Sellin, P.; Wang, T.; Liu, W.; Zha, G.; Veeramani, P.; Mills, C. Study on Temperature Dependent Resistivity of Indium-Doped Cadmium Zinc Telluride. J. Phys. D. Appl. Phys. 2009, 42, 035105.

(56) S. M. Sze and K. K. Ng , *Physics of Semiconductor Devices* , John Wiley and Sons, Hoboken, 2006.

(57) O. A. Lozhkina , A. A. Murashkina , M. S. Elizarov , V. V. Shilovskikh , A. A. Zolotarev , Y. V. Kapitonov , R. Kevorkyants , A. V. Emeline and T. Miyasaka , Microstructural Analysis and Optical Properties of the Halide Double Perovskite Cs2BiAgBr6 Single Crystals, *Chem. Phys. Lett.*, 2018, **694** , 18–22.

(58) Bube, R. H. Trap Density Determination by Space-Charge-Limited Currents. J. Appl. Phys. 1962, 33 (5), 1733–1737.

(59) Steele, J. A.; Puech, P.; Keshavarz, M.; Yang, R.; Banerjee, S.; Debroye, E.; Kim, C. W.; Yuan, H.; Heo, N. H.; Vanacken, J.; et al. Giant Electron-Phonon Coupling and Deep

Conduction Band Resonance in Metal Halide Double Perovskite. ACS Nano 2018, 12 (8), 8081–8090.

(60) Gao, W.; Ran, C.; Xi, J.; Jiao, B.; Zhang, W.; Wu, M.; Hou, X.; Wu, Z. High-Quality Cs2AgBiBr6 Double Perovskite Film for Lead-Free Inverted Planar Heterojunction Solar Cells with 2.2 % Efficiency. ChemPhysChem 2018, 19 (14), 1696–1700.

(61) Dong, Q.; Fang, Y.; Shao, Y.; Mulligan, P.; Qiu, J.; Cao, L.; Huang, J. Electron-Hole Diffusion Lengths > 175 μm in Solution-Grown CH3NH3PbI3 Single Crystals. Science (80-.). 2015, 347 (6225), 967–970.

(62) Liu, Y.; Yang, Z.; Cui, D.; Ren, X.; Sun, J.; Liu, X.; Zhang, J.; Wei, Q.; Fan, H.; Yu, F.; et al. Two-Inch-Sized Perovskite CH3NH3PbX3 (X = Cl, Br, I) Crystals: Growth and Characterization. Adv. Mater. 2015, 27 (35), 5176–5183.

(63) Thirimanne, H. M.; Jayawardena, K. D. G. I.; Parnell, A. J.; Bandara, R. M. I.; Karalasingam, A.; Pani, S.; Huerdler, J. E.; Lidzey, D. G.; Tedde, S. F.; Nisbet, A.; et al. High Sensitivity Organic Inorganic Hybrid X-Ray Detectors with Direct Transduction and Broadband Response. Nat. Commun. 2018, 9 (1), 2926.

(64) Bogardus, E. H.; Bebb, H. B. Bound-Exciton, Free-Exciton, Band-Acceptor, Donor-Acceptor, and Auger Recombination in GaAs. Phys. Rev. 1968, 176, 993–1002.

(65) Shi, D.; Adinolfi, V.; Comin, R.; Yuan, M.; Alarousu, E.; Buin, A.; Chen, Y.; Hoogland, S.; Rothenberger, A.; Katsiev, K.; et al. Low Trap-State Density and Long Carrier Diffusion in Organolead Trihalide Perovskite Single Crystals. Science (80-.). 2015, 347, 519–522.

(66) Yacobi, B. G.; Holt, D. B. Cathodoluminescence Scanning Electron Microscopy of Semiconductors. J. Appl. Phys. 1986, 59, R1–R24.

(67) Xiao, Z.; Meng, W.; Wang, J.; Yan, Y. Thermodynamic Stability and Defect Chemistry of Bismuth-Based Lead-Free Double Perovskites. ChemSusChem 2016, 9, 2628–2633.

(68) A. H. Slavney , R. W. Smaha , I. C. Smith , A. Jaffe , D. Umeyama and H. I. Karunadasa , Chemical Approaches to Addressing the Instability and Toxicity of Lead–Halide Perovskite Absorbers, *Inorg. Chem.*, 2017, 56, 46-55.

(69) Karunadasa, H. I.; Slavney, A. H. Halide Double Perovskite Cs2AgBiBr6 Solar-Cell Absorber Having Long Carrier Lifetimes. U.S. Patent Application 20170194101, 2017.

(70) R. L. Z. Hoye , L. Eyre , F. Wei , F. Brivio , A. Sadhanala , S. Sun , W. Li , K. H. L. Zhang , J. L. MacManus-Driscoll and P. D. Bristowe , *et al.*, Fundamental Carrier Lifetime Exceeding 1 μs in Cs2AgBiBr6 Double Perovskite, *Adv. Mater. Interfaces*, 2018, 5, 1800464.

(71) S. Johnston , K. Zaunbrecher , R. Ahrenkiel , D. Kuciauskas , D. Albin and W. Metzger , Simultaneous Measurement of Minority-Carrier Lifetime in Single-Crystal CdTe Using Three Transient Decay Techniques, *IEEE J. Photovolt.*, 2014, 4, 1295-1300.

(72) Pan, W.; Wu, H.; Luo, J.; Deng, Z.; Ge, C.; Chen, C.; Jiang, X.; Yin, W. J.; Niu, G.; Zhu, L.; et al. Cs2AgBiBr6 Single-Crystal X-Ray Detectors with a Low Detection Limit. Nat. Photonics 2017, 11 (11), 726–732.

(73) He, Y.; Liu, Z.; McCall, K. M.; Lin, W.; Chung, D. Y.; Wessels, B. W.; Kanatzidis, M. G. Perovskite CsPbBr 3 Single Crystal Detector for Alpha-Particle Spectroscopy. Nucl. Instruments Methods Phys. Res. Sect. A Accel. Spectrometers, Detect. Assoc. Equip. 2019, 922, 217–221.

(74) Xia, J.; Streicher, M.; Zhu, Y.; He, Z. Measurement of Electron Mobility-Lifetime Product in 3-D Position-Sensitive CdZnTe Detectors Using the VAD UMv2.2 Digital Readout System. IEEE Trans. Nucl. Sci. 2018, 65 (11), 2834–2837.

(75) Yin, L.; Wu, H.; Pan, W.; Yang, B.; Li, P.; Luo, J.; Niu, G.; Tang, J. Controlled Cooling for Synthesis of Cs2AgBiBr6 Single Crystals and Its Application for X-Ray Detection. Adv. Opt. Mater. 2019, 7 (19), 1900491.

(76) Zhang, Z.; Huang, Z.; Chung, C.; Sun, D.; Yang, G. Gamma-Ray Detection Using Bi-poor Cs2AgBiBr6 Double Perovskite Single Crystals. (Under Revision)

(77) Zhang, M.; Zheng, Z.; Fu, Q.; Chen, Z.; He, J.; Zhang, S.; Yan, L.; Hu, Y.; Luo, W. Growth and Characterization of All-Inorganic Lead Halide Perovskite Semiconductor CsPbBr3 Single Crystals. CrystEngComm 2017, 19 (45), 6797–6803.

(78) Liu, Y.; Yang, Z.; Cui, D.; Ren, X.; Sun, J.; Liu, X.; Zhang, J.; Wei, Q.; Fan, H.; Yu, F.; et al. Two-Inch-Sized Perovskite CH3NH3PbX3 (X = Cl, Br, I) Crystals: Growth and Characterization. Adv. Mater. 2015, 27 (35), 5176–5183.

(79) Futscher, M. H.; Lee, J. M.; McGovern, L.; Muscarella, L. A.; Wang, T.; Haider, M. I.; Fakharuddin, A.; Schmidt-Mende, L.; Ehrler, B. Quantification of Ion Migration in CH3NH3PbI3 Perovskite Solar Cells by Transient Capacitance Measurements. Mater. Horizons 2019, 6 (7), 1497–1503.

(80) Phung, N.; Al-Ashouri, A.; Meloni, S.; Mattoni, A.; Albrecht, S.; Unger, E. L.; Merdasa, A.; Abate, A. The Role of Grain Boundaries on Ionic Defect Migration in Metal Halide Perovskites. Adv. Energy Mater. 2020, 10 (20), 1903735.

(81) Lan, D. The Physics of Ion Migration in Perovskite Solar Cells: Insights into Hysteresis, Device Performance, and Characterization. Prog. Photovoltaics Res. Appl. 2020, 28 (6), 533–537.

(82) Zhang, H.; Fu, X.; Tang, Y.; Wang, H.; Zhang, C.; Yu, W. W.; Wang, X.; Zhang, Y.; Xiao, M. Phase Segregation Due to Ion Migration in All-Inorganic Mixed-Halide Perovskite Nanocrystals. Nat. Commun. 2019, 10 (1), 1–8.

(83) Choong, W.; Derenzo, S. E.; Moses, W. W.; Ce, L.; Choong, W.; Derenzo, S. E.; Moses, W. W. Evaluation of Production Samples of the Scintillators LaBr3 : Ce and LaCl3 : Ce, International Conference on Inorganic Scintillators and their Industrial Applications; Crimea (Ukraine), 19-23 Sep 2005.

(84) Liu, Y.; Yang, Z.; Liu, S. F. Recent Progress in Single-Crystalline Perovskite Research Including Crystal Preparation, Property Evaluation, and Applications. Adv. Sci. 2018, 5 (1), 1700471.

(85) Longo, G.; Mahesh, S.; Buizza, L. R. V.; Wright, A. D.; Ramadan, A. J.; Abdi-Jalebi, M.; Nayak, P. K.; Herz, L. M.; Snaith, H. J. Understanding the Performance-Limiting Factors of Cs2AgBiBr6Double-Perovskite Solar Cells. ACS Energy Lett. 2020, 5 (7), 2200–2207.

(86) Li, L.; Lu, F.; Lee, C.; Black, M.; James, R.; Wright, G.; Bolotnikov, A.; Olsen, R.; Burger, A.; Gostilo, V.; et al. New Progress in Large-Size CZT (Zn=10%) Single Crystal Growth Using MVB Technique for Room Temperature Radiation Detectors. In IEEE Nuclear Science Symposium Conference Record; IEEE, 2004; Vol. 4, pp 2320–2323.

(87) Henini, M. Molecular Beam Epitaxy: From Research to Mass Production; 2nd ed.; Elsevier, 2018.

(88) Schroder, D. K. Advanced Mos Devices (Modular Series on Solid State Devices); Addison-Wesley, 1987.

(89) Yuan, Z.; Huang, W.; Ma, S.; Ouyang, G.; Hu, W.; Zhang, W. A High Performance Perovskite CH3NH3PbCl3 Single Crystal Photodetector: Benefiting from an Evolutionary Preparation Process. J. Mater. Chem. C 2019, 7 (18), 5442–5450.

(90) Dang, Y.; Tong, G.; Song, W.; Liu, Z.; Qiu, L.; Ono, L. K.; Qi, Y. Interface Engineering Strategies towards Cs2AgBiBr6 Single-Crystalline Photodetectors with Good Ohmic Contact Behaviours. J. Mater. Chem. C 2019, 8 (1), 276–284.

(91) Datta, A.; Becla, P.; Motakef, S. Novel Electrodes and Engineered Interfaces for Halide-Semiconductor Radiation Detectors. Sci. Rep. 2019, 9 (1), 1–10.

(92) Datta, A.; Becla, P.; Motakef, S. Thallium Bromide Semiconductor Radiation Detectors with Thallium Contacts. IEEE Trans. Nucl. Sci. 2018, 65 (8), 2329–2332.

(93) Du, H.; Antonuk, L. E.; El-Mohri, Y.; Zhao, Q.; Su, Z.; Yamamoto, J.; Wang, Y. Investigation of the Signal Behavior at Diagnostic Energies of Prototype, Direct Detection, Active Matrix, Flat-Panel Imagers Incorporating Polycrystalline HgI2. Phys. Med. Biol. 2008, 53 (5), 1325–1351.

(94) Schade, L.; Wright, A. D.; Johnson, R. D.; Dollmann, M.; Wenger, B.; Nayak, P. K.; Prabhakaran, D.; Herz, L. M.; Nicholas, R.; Snaith, H. J.; et al. Structural and Optical Properties of Cs2AgBiBr6 Double Perovskite. ACS Energy Lett. 2019, 4 (1), 299–305.

(95) Zhao, Y.; Li, C.; Shen, L. Recent Advances on Organic-inorganic Hybrid Perovskite Photodetectors with Fast Response. InfoMat 2019, 1 (2), 164-182.

(96) Zanatta, A. R. Revisiting the Optical Bandgap of Semiconductors and the Proposal of a Unified Methodology to Its Determination. Sci. Rep. 2019, 9 (1), 11225.

(97) Ji, F.; Klarbring, J.; Wang, F.; Ning, W.; Wang, L.; Yin, C.; Figueroa, J. S. M.; Christensen, C. K.; Etter, M.; Ederth, T.; et al. Lead-Free Halide Double Perovskite Cs2AgBiBr6 with Decreased Band Gap. Angew. Chemie - Int. Ed. 2020, 59 (35), 15191–15194.

(98) Kanemitsu, Y. Luminescence Spectroscopy of Lead-Halide Perovskites: Materials Properties and Application as Photovoltaic Devices. Journal of Materials Chemistry C. Royal Society of Chemistry April 6, 2017, pp 3427–3437.

(99) M. Sugawara, Self-assembled InGaAs/GaAs quantum dots, Academic Press, 1999.

(100) Lin, W.; Stoumpos, C. C.; Liu, Z.; Das, S.; Kontsevoi, O. Y.; He, Y.; Malliakas, C. D.; Chen, H.; Wessels, B. W.; Kanatzidis, M. G. TlSn2I5, a Robust Halide Antiperovskite Semiconductor for γ-Ray Detection at Room Temperature. ACS Photonics 2017, 4 (7), 1805–1813.

(101) Owens, A. Semiconductor Materials and Radiation Detection. J. Synchrotron Radiat. 2006, 13 (2), 143–150.

(102) Owens, A. Compound Semiconductor Radiation Detectors. CRC Press, 2016.

(103) Bolotnikov, A. E.; Camarda, G. S.; Chen, E.; Cui, Y.; Gul, R.; Dedic, V.; De Geronimo, G.; Fried, J.; Hossain, A.; MacKenzie, J. M.; et al. Using the TOF Method to Measure the Electron Lifetime in Long-Drift CdZnTe Detectors (Conference Presentation). In Hard X-Ray, Gamma-Ray, and Neutron Detector Physics XVIII; Fiederle, M., Burger, A., Franks, L., James, R. B., Eds.; SPIE, 2016; Vol. 9968, p 37.

(104) Su, J.; Huang, Y. qiang; Chen, H.; Huang, J. Solution Growth and Performance Study of Cs2AgBiBr6 Single Crystal. Cryst. Res. Technol. 2020, 55 (3), 1900222.

(105) Zhang, W.; Gong, Z.; Pan, S.; Zhang, Y.; Chen, D.; Pan, J. Growth and Photodetection Properties of Cs2AgBiBr6 Crystals with Large Flat (111) Plane Grown from the Solution by Adding Toluene. J. Cryst. Growth 2020, 125922.

APPENDICES

Appendix A

This appendix is not published and the interpretation of shallow/deep defects is preliminary by referring to the published theoretical reports [49, 67]. No further supplementary experiments have been performed to verify the emission origins of the observed CL peaks.

Temperature-dependent CL data of $Cs_2AgBiBr_6$ single crystals were shown in Figures A1 and A2. Deep understanding of the present defects in $Cs_2AgBiBr_6$ using CL spectra could serve better for the further development of $Cs_2AgBiBr_6$-based radiation detectors. Figure A3 is a schematic which explains the possible transitions between either shallow or deep defect energy levels. A summary of the luminescence origins of the observed CL emission peaks is made in Table A1.

It should be noted that although the emission origins of CL peaks/features are not exclusively clear, some of the analyses could be done to help the understanding. To gain more insight into the CL features, we plotted the CL peak energy vs. temperatures, shown in Figure A4. Features G and H are only distinguishable at low temperatures. As discussed in Chapter 4, they are corresponding to 1.917 eV and 2.054 eV respectively at T=83 K. We think feature G in the CL spectra are near bandgap emissions. It is likely ascribed to free exciton recombination. This is also revealed in Figure A4, which shows the slope of linear fitting curve for peak G is negligibly small (~ -0.005 meV/K). Also assisted by the slope of linear fitting curve (~ -0.015 meV/K), feature H could also be induced by defects (probably interstitial Cs_i or Ag_i, see Figure A3). The possibility that feature H is originated from exciton emissions, as discussed in Chapter 4, could not be eliminated.

We also observed a very small red shift of feature D and peak E, approximately 2 meV and 6 meV respectively (Figure A5 (b) and (c)). The red shift was not explicitly observed for

peak C, as displayed in Figure A5 (a). The other peaks tend to disappear at room temperature as shown in the previous CL spectra and therefore they will not be discussed. This small red shift should be normal in semiconductors. It can be ascribed to the nonhomogeneous spatial distribution of excited charge carriers in the bulk $Cs_2AgBiBr_6$ single crystals [98]. Electrons and holes are produced in the near-surface region from band-to-band excitation and then diffuse into the interior of single crystals. The nonhomogeneous spatial profiles of charge carriers can induce slight temporal changes in the CL spectra. This also leads to think that the consistent same shape electron focal spot (determined by the stability of electron beam) can play an important role in the entire process of CL measurement, especially for thick single crystals.

In addition, we analyzed the linewidth or full width at half maximum (FWHM) of CL emission peaks by Gaussian fitting, as exhibited in Figure A6. In general, the analyzed linewidth is ranging from several meV to roughly one hundred meV. The first observation in Figure A6 is the linewidth of some CL peaks rises and then decreases, while the others decrease and then rise. Especially, the FWHM at 123 K rises/decreases obviously for features A, B, C, G and H. Such changes could be associated with the structural phase transition in $Cs_2AgBiBr_6$ single crystals at ~ 122 K from tetragonal (low temperature) to cubic (high temperature) [94]. We also observed that linewidth of D peak is temperature-independent, which could be caused by the structural inhomogeneity. Inhomogeneous broadening induced by the structural inhomogeneity controls the shape of D feature, while the phonon scattering processes and thermal carrier distribution determine the natural peak linewidth and therefore should play a much less important role [99]. On the other hand, CL peaks are well fitted by Gaussian functions rather than Lorentzian, which indicated that the peak linewidth should not be mainly contributed by natural broadening.

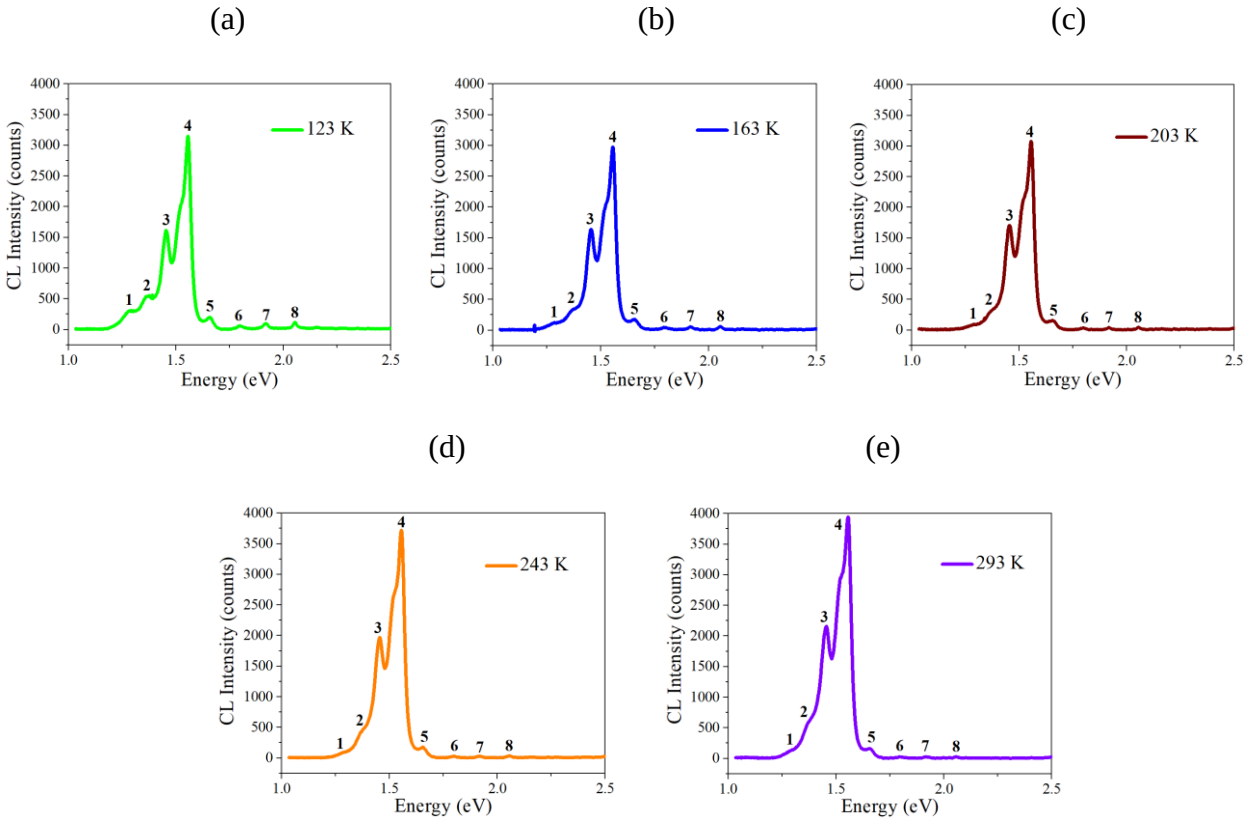

Figure A1. Cathodoluminescence spectrum of $Cs_2AgBiBr_6$ single crystals at (a) 123 K (b) 163 K (c) 203 K (d) 243 K (e) 293 K.

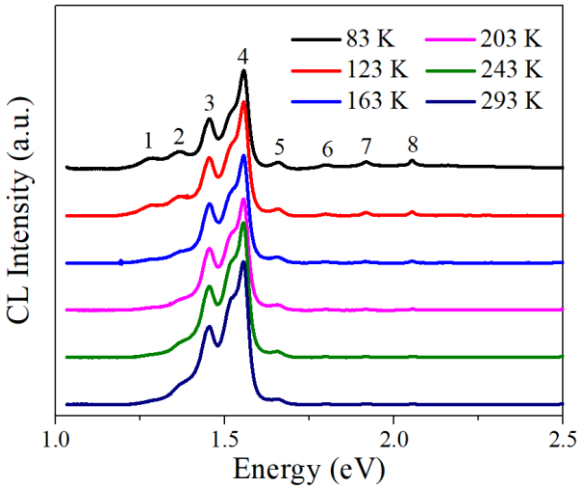

Figure A2. Grouped CL spectra for comparison, measured from 83 K to room temperature 293 K. The spectrum is shifted for clarity.

Table A1. Luminescence origins of CL emission peaks

Peak Number	Emission Mechanism
1 / Feature A	-
2 / Feature B	D-A (or Donor to Acceptor)
3 / Feature C	Donor-to-Valence
4 / Feature D	D-A
5 / Feature E	D-A
6 / Feature F	D-A
7 / Feature G	Free Exciton
8 / Feature H	Free/Bound Exciton or Donor-to-Valence

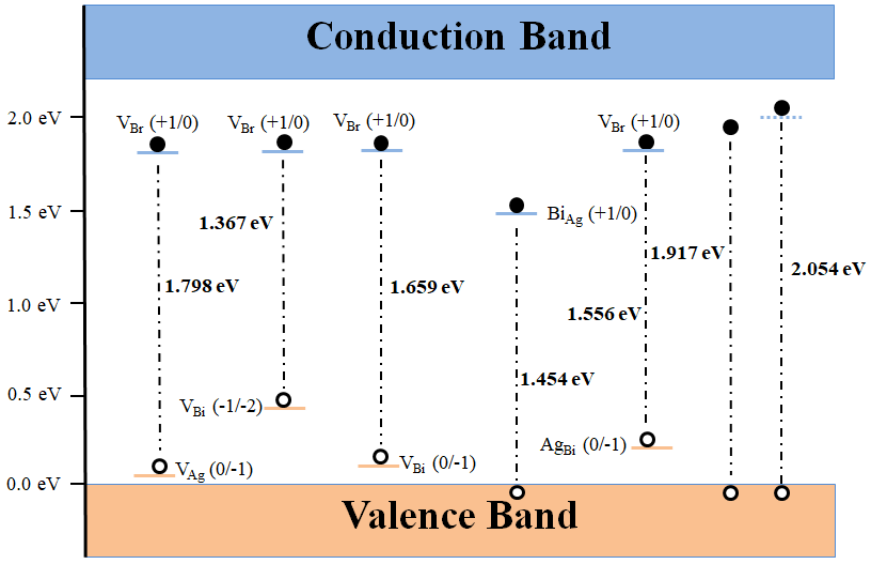

Figure A3. CL transition energy levels in $Cs_2AgBiBr_6$ single crystals. To clarify, the dashed line on the 2.054 eV emission refers to the possible Cs_i (+1/0) or Ag_i (+1/0) defect energy level. Note the energy depicted in the plot corresponds to T=83 K. V represents vacancy defects (e.g., V_{Br}: Br vacancy), Ag_{Bi} and Bi_{Ag} are antisite substitution defects.

Based on our hypothesis, it does show that certain number of deep electron traps V_{Br} vacancy defects present in as-grown Bi-normal $Cs_2AgBiBr_6$ single crystals. Meanwhile, the V_{Br} vacancy defect could have participated in several donor to acceptor transitions and thus caused

the appearance of multiple CL peaks. To verify our hypothesis, future work could be to conduct the temperature-dependent CL study for Bi-poor $Cs_2AgBiBr_6$ single crystals. If the CL transition peaks (which were hypothesized to be contributed by V_{Br} donor to valence transitions) have dramatically reduced peak intensities, then we could have more confidence regarding our hypothesis. Moreover, as discussed in Chapter 4, thermal annealing or solvent annealing (e.g., DMF, isopropanol) technique could be used to treat Bi-normal $Cs_2AgBiBr_6$ single crystals. The temperature-dependent study in combination with annealing treatment should be able to solve some of the confusions for the emission origins of vacancy-related CL peaks.

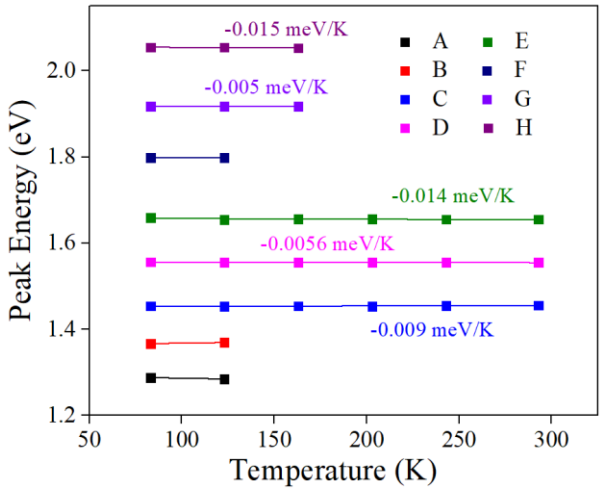

Figure A4. Energy of CL features vs. temperature. Solid lines are the linear fitting curve with slope displayed.

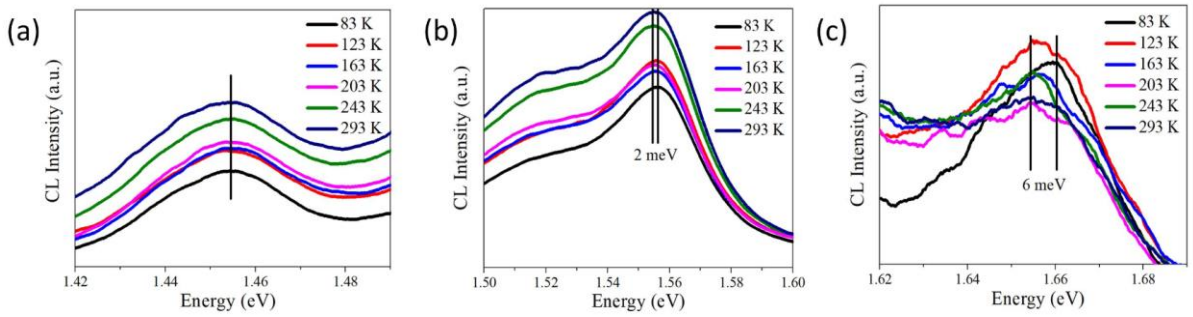

Figure A5. Zoom-in CL plot of (a) C feature and (b) D feature and (c) E feature.

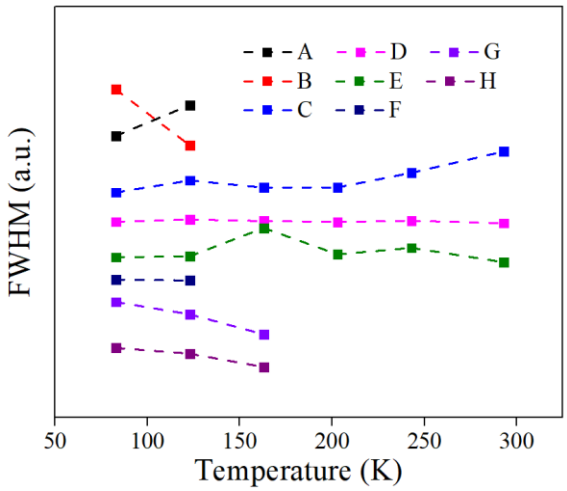

Figure A6. Linewidth of CL emission peaks at measured temperatures. The curve is shifted for clarity.

Appendix B

Figure B1 shows the Time-of-Flight (ToF) pulse traces using Bi-poor $Cs_2AgBiBr_6$-based detector with silver paste deposited on two opposite pristine surfaces of one single crystal (crystal thickness: ~0.2 cm). Using the ToF technique, the charge carrier mobility could be estimated using

$$\mu = \frac{v}{E} = \frac{d/t}{E}$$

where v is the drift velocity, d is the detector length, t is the transit time, and E is the applied electric field.

From Figure B1 (a), the transit time at bias of 100 V is read as ~80 μs, which equals two times the time required for collected charge to reach 50% of the maximum. Thus, the charge carrier mobility is

$$\mu = \frac{v}{E} = \frac{d/t}{E} = \frac{0.2\ cm\ /\ 80\ \mu s}{100\ V/\ 0.2\ cm} = 5\ cm^2/V \cdot s$$

It should be noted that the carrier mobility estimated here is a contribution from both electrons and holes as the 59.5 keV gamma-ray can deposit the energy inside the $Cs_2AgBiBr_6$ single crystal. Figure B1 (b) shows the amplitude from the preamplifier pulse is only 60 mV at bias of 50 V compared to 180 mV (Figure B1 (a)) at bias of 100 V. This indicates that the charge collection is limited at bias voltage of 50 V.

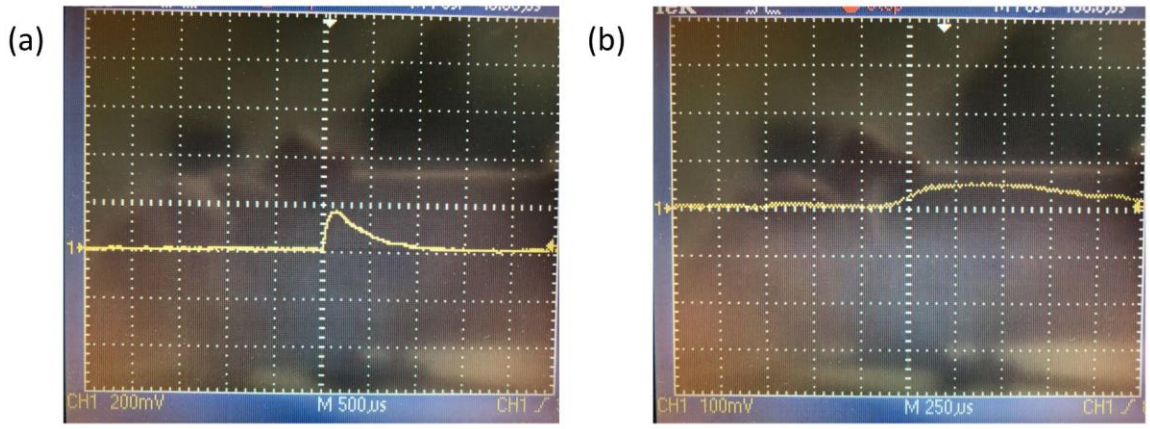

Figure B1. Time-of-Flight (ToF) pulse traces using Bi-poor $Cs_2AgBiBr_6$-based detector and ^{241}Am radioactive source, the detector is biased at (a) 100 V and (b) 50 V respectively.

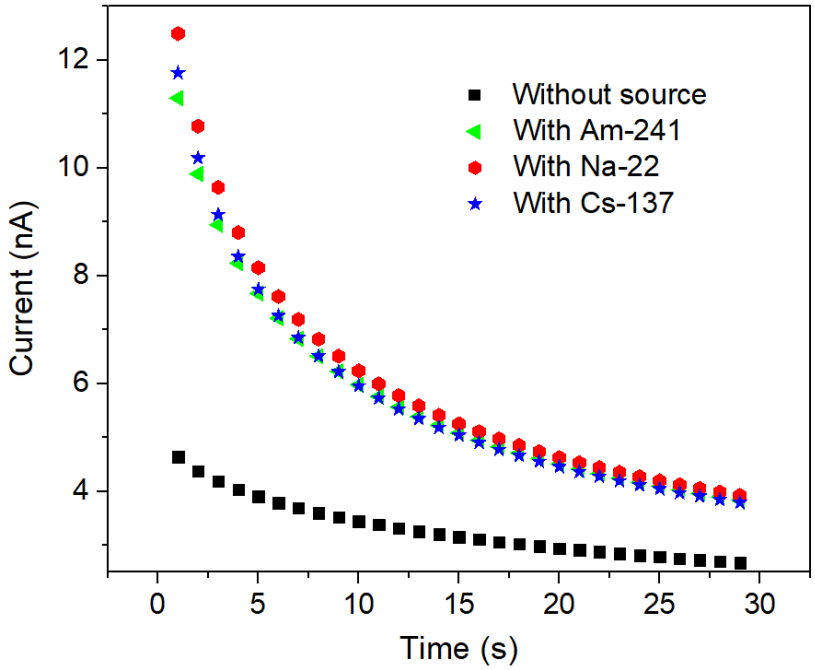

Figure B2. Response of Bi-poor $Cs_2AgBiBr_6$ single crystals to Am-241, Na-22, and Cs-137 radioactive sources, measurement was conducted at room temperature with bias of +70V.

Figure B2 shows the response of Bi-poor $Cs_2AgBiBr_6$ single crystals to Am-241, Na-22, and Cs-137 radioactive sources. It clearly shows that when the Am-241, Na-22, and Cs-137 sources were placed near the Bi-poor $Cs_2AgBiBr_6$-based detector, the current that flows through

the detector was dramatically increased. This indicates that Bi-poor $Cs_2AgBiBr_6$-based detector should be able to respond to gamma photons. Moreover, it could be observed that with Am-241 and Na-22 present, the current recorded with Am-241 source is lower compared to that with Na-22 present. This is expected as the crystal is around 2 mm thick. For this thickness, the 59.5 keV gamma-ray emitted from Am-241 could not penetrate the crystal and thus most of the 59.5 keV photons should be able to deposit the full energy inside the single crystals. While for the 511 keV gamma-ray emitted from Na-22, it could penetrate the single crystal and thus is more likely depositing more energy inside the single crystals. When the Cs-137 source is present, the recorded current is higher than that with Am-241, but lower than that with Na-22. This could be due to the fact that the amount of energy deposited inside the single crystals is highly dependent on the location that photons interact with the detector. Since both 511 keV gamma-ray emitted from Na-22 and 662 keV gamma-ray emitted from Cs-137 could penetrate the crystal, the current recorded or the energy deposited is then dependent on the location that photons hit the detector.

Figure B3 shows the gamma energy spectrum recorded by CZT and Bi-poor $Cs_2AgBiBr_6$-based detectors. The CZT crystal is about 5 mm cubic large and thus the 662 keV gamma-ray could penetrate both the CZT and Bi-poor $Cs_2AgBiBr_6$ single crystals (~2 mm thick). The spectrum recorded by the Bi-poor $Cs_2AgBiBr_6$-based detector shows that the 59.5 keV gamma photons was barely resolved when the measurement time was short (100 seconds). This could be due to the high detector noise in Bi-poor $Cs_2AgBiBr_6$-based detectors. To further the development of Bi-poor $Cs_2AgBiBr_6$ for gamma photon detection, the detector noise should be suppressed with either a higher-quality detector-grade single crystal or with a better device design for noise suppression (such as Schottky-type design for CZT and $CsPbBr_3$ perovskite

single crystals). Essentially, for Schottky-type design, two metal contacts with different work functions could be used for electrodes deposition. Common metal contact materials, such as Au (work function: 5.10-5.47 eV) and Ag (work function: 4.26-4.74 eV) could be adopted for use.

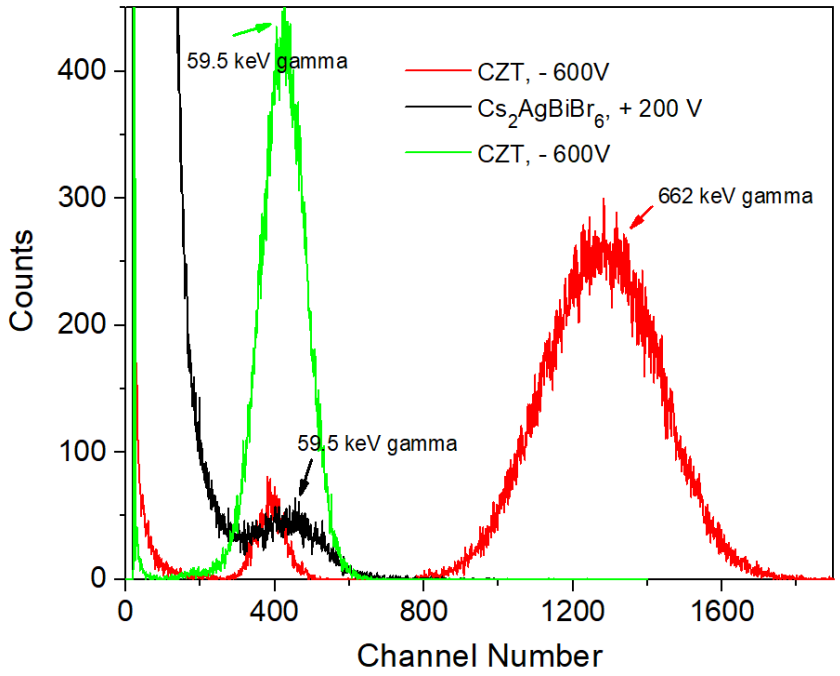

Figure B3. Comparison between the gamma energy spectrum recorded by CZT and Bi-poor $Cs_2AgBiBr_6$-based detectors, measurement was conducted at room temperature with 100 seconds recording time.

Appendix C

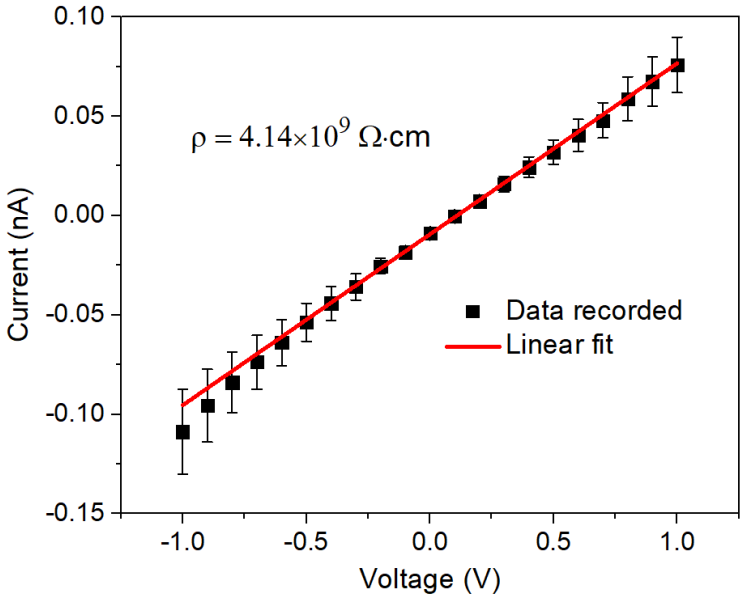

Figure C1. Current-voltage measurement of Bi-poor $Cs_2AgBiBr_6$ single crystals, measurement was conducted at room temperature.

Figure C1 shows current-voltage (I-V) measurement for Bi-poor $Cs_2AgBiBr_6$ single crystals (crystal thickness: ~0.16 cm, metal electrode area: ~0.25×0.19 cm^2), measurement was conducted at room temperature. The determined resistivity is 4.14×10^9 Ω·cm and silver paste was used as metal electrode. To find the resistivity range for solution-processed $Cs_2AgBiBr_6$ single crystals from Bi-normal and Bi-poor growth conditions, we have performed the I-V measurement for several Bi-normal and Bi-poor single crystals. In general, $Cs_2AgBiBr_6$ single crystals grown under these conditions have resistivity of 10^9 Ω·cm to 10^{11} Ω·cm.